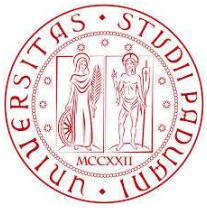

UNIVERSITÀ DEGLI STUDI DI PADOVA

Dipartimento di Geoscienze
Direttore Prof.ssa Cristina Stefani

TESI DI LAUREA MAGISTRALE
IN
GEOLOGIA E GEOLOGIA TECNICA

MULTISCALE PETROPHYSICAL AND THERMAL PROPERTIES ANALYSIS OF ROCKS

Relatore:
Prof. Antonio Galgaro
Correlatori:
Dott. Matteo Cultrera
Dott. Michele Secco

Laureanda: *Stefania Simion*

ANNO ACCADEMICO 2015/2016

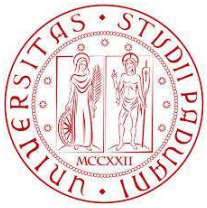

UNIVERSITÀ DEGLI STUDI DI PADOVA

Dipartimento di Geoscienze
Direttore Prof.ssa Cristina Stefani

TESI DI LAUREA MAGISTRALE
IN
GEOLOGIA E GEOLOGIA TECNICA

MULTISCALE PETROPHYSICAL AND THERMAL PROPERTIES ANALYSIS OF ROCKS

ANALISI MULTISCALA DELLE PROPRIETA' PETROFISICHE E TERMICHE DELLE ROCCE

Relatore:
Prof. Antonio Galgaro
Correlatori:
Dott. Matteo Cultrera
Dott. Michele Secco

Laureanda: *Stefania Simion*

ANNO ACCADEMICO 2015/2016

A mamma e papà

Abstract

Data on thermal properties of rocks such as thermal conductivity (λ), thermal diffusivity (α), specific heat capacity (c_p) are necessary for many aspects of exploration and exploitation of geothermal fields (Popov et al., 2012), in both high-low enthalpy and geo-exchange systems. However, there are still several difficulties in characterize geological materials, because their thermal properties are extremely dependent on scale of measurement. From a micro- and mesoscale point of view, porosity (in sedimentary and volcanic rocks), the dominant mineral phase (in metamorphic and plutonic rocks), and anisotropy (in sedimentary and metamorphic rocks) are important controlling factors on thermal conductivity. Texture have been scarcely investigated. Anyway, thermal conductivity as a tensor depends not only on the volume fraction and thermal conductivity of rock components, but also on their distribution, on geometry and internal structure, and on the heat transfer conditions at the contacts between them (Schön, 2011). Thus, understanding the influence on thermal properties of the texture is a present-day challenge whose results could provide a huge contribution to the scientific community now involved in geothermal energy topics.

The main goal of the present project is to provide an example of a new approach that could take into account the thermo-physical properties of rocks at the microscale as well as those at meso- and macroscale. Some techniques have been tested on two different lithologies, dolomites on one hand and trachytes on the other, and results have been discussed separately. μ-XRF seems to be the "turning point" technique for analyses of petro-physical properties on effusive rocks as trachytes since the image analysis on the elemental X-ray maps provides reliable quantitative information on texture and rock-forming minerals in

relatively short analysis times. In the same way, a good applicability of the technique is assumed on intrusive rocks. Conversely, the micro-XRF doesn't provide the expected results for dolomites. Among those tested, the He pycnometer technique remains the most accurate one for measuring porosity.

In addition, a search on literature was made to understand how thermal properties of rock-forming minerals were and can be measured; an overview on the models for the computation of thermal conductivity of rocks starting from rock-forming minerals values is provided.

A continuation of this study is necessary in order to (1) test the validity of the proposed methods on other lithologies, (2) deepen the study of texture influences on thermal conductivity, (3) contribute to the compilation of rock thermal properties database collected by several authors, (4) apply the acquired information for numerical modelling purposes.

Riassunto

I dati relativi alle proprietà termiche delle rocce, come conducibilità termica (λ), diffusività termica (α), capacità termica volumetrica (c_p) sono necessari per molti aspetti dell'esplorazione e dello sfruttamento in campo geotermico (Popov et al., 2012), sia in sistemi di bassa e alta entalpia che in sistemi di geoscambio. Tuttavia, ci sono ancora numerose difficoltà nella caratterizzazione dei materiali geologici, perché le loro proprietà termiche dipendono fortemente dalla scala in cui vengono effettuate le misure. Da un punto di vista micro- e mesoscopico, la porosità (nelle rocce sedimentarie e vulcaniche), la fase mineralogica principale (nelle rocce metamorfiche e plutoniche), e l'anisotropia (nelle rocce sedimentarie e metamorfiche) sono importanti fattori di controllo sulla conducibilità termica. La tessitura delle rocce è stata scarsamente investigata. La conducibilità termica in quanto tensore dipende però non solo dalla frazione di volume e dalla conducibilità termica delle componenti della roccia, ma anche dalla loro distribuzione, geometria e struttura interna, e dalle condizioni di trasferimento di calore ai loro contatti (Schön, 2011). Perciò, comprendere l'influenza della tessitura sulle proprietà termiche è una sfida attuale i cui risultati potrebbero fornire un importante contributo alla comunità scientifica ora coinvolta dei temi legati alla geotermia.

L'obiettivo principale del presente progetto è quello di fornire un esempio di un nuovo approccio in grado di prendere in considerazione le proprietà termo-fisiche delle rocce alla microscala così come alla meso- e macroscala. Sono state testate alcune tecniche su due differenti litologie, dolomie da una parte e trachiti dall'altra, e i risultati sono stati discussi separatamente. La μ-XRF si è dimostrata una tecnica di svolta per le analisi delle proprietà petro-fisiche delle rocce

effusive come le trachiti dal momento che l'analisi di immagine sulle mappe elementari a raggi X forniscono informazioni quantitative sulla tessitura e sui minerali che compongono la roccia in tempi relativamente brevi. Allo stesso modo, si ipotizza una buona applicabilità della tecnica su rocce intrusive. Per le dolomie, invece, la micro-XRF sembra non dare i risultati sperati. Tra quelle utilizzate, il picnometro ad elio rappresenta la tecnica più accurata per le misure di porosità.

Una ricerca in letteratura è stata inoltre condotta per capire come le proprietà termiche sono state e possono essere misurate sui minerali che compongono le rocce; viene fornita anche una panoramica sui modelli che permettono di ottenere la conducibilità delle rocce a partire dai valori dei minerali costituenti.

La continuazione di questo studio è necessaria per (1) testare la validità dei metodi qui proposti su altre litologie, (2) approfondire lo studio sull'influenza della tessitura sulla conducibilità termica, (3) contribuire alla compilazione di database con le proprietà termiche misurate da diversi autori, (4) applicare le informazioni acquisite a scopi di modellazione numerica.

Table of contents

1 Introduction

Geothermal energy is defined as the energy stored in the form of heat beneath the surface of the earth (RES Directive 2009/28/EC). Geothermal energy is one of the most promising source due to its high potential and multiple uses. Geothermal investigations are related to many questions in geoscience, ranging from studies of the physical state of the earth, tectonics, seismicity, and volcanism to practical problems in mining, drilling, geothermal resources, and geothermal methods used in exploration and environmental geophysics (Schön, 2011).

Nowadays more and more attention is focused on so called "shallow geothermal heat exchange". The underground in the first approx. 100 m is well suited for supply and storage of geothermal heat. The climatic temperature change over the seasons is reduced to a steady temperature at 10-20 m depth, and with further depth temperatures increases according to the geothermal gradient (average 3 °C per 100 m of depth). The main methods to make use of this energy are (Quaschning, 2005):

- Ground Source Heat Pumps, or Geothermal Heat Pumps. They are an established technology that uses the heat stored beneath the earth surface, the temperature from the ground, for heating and cooling buildings. They can be used in a wide range of applications, from small, residential houses to large individual building or complexes.
- Underground Thermal Energy Storage. The temperature in the ground is changed by injecting or abstracting calories, that can be retrieved later; usually seasonal storage.

With the aim of both reduce the overall costs of shallow geothermal systems and improve their installation safety, an European project has took place recently, under the Horizon 2020 EU Framework Programme for Research and Innovation. The acronym of this project is Cheap-GSHPs, meaning "cheap and efficient application of reliable ground source heat exchangers and pumps"; the CHEAP-GSHPs project involves 17 partners among 9 European countries such Belgium, France, Germany, Greece, Ireland, Italy, Romania, Spain, Switzerland (Bertermann et al., 2016).

Regarding the geological features that must unavoidably be considered, Padua University plays a key role within and for the project. In particular, it is leader of one task dealing with geological mapping, climatic data and energy requirements. UNIPD, with the collaboration of other institutions (CNR, Energesis Group S.L., FAU, CRES and others), has established different objectives such as to evaluate the base thermal properties of rock- and unconsolidated materials, to relate buildings case studies for different users destination to specific climatic, geothermal, geological conditions for shallow geothermal application, to develop thematic maps useful for managing shallow geothermal system applications at municipal level, etc. In order to achieve the planned targets, an holistic approach is adopted, where all involved elements that take part of shallow geothermal activities are integrated (Bertermann et al., 2016).

A reliable determination of rock thermal properties is then fundamental in evaluating the regional heat flow, the underground heat transfer processes and geothermal reservoirs characterization. An accurate thermal characterization is always needed but it is often very difficult to be done. There are several difficulties in measuring the thermal properties of rocks and the main reason deals with the fact that their parameters are extremely dependent on scale of measurement. Some factors relates to the mineralogical and petrographic texture at microscale; other ones depend on mesoscale factors such porosity, density, moisture conditions, anisotropy, etc.; finally, other factors are related to the geothermal gradient, fracturing, compaction, hydrogeological conditions at field scale. As in the case with most other petrophysical properties, in-situ thermal conductivity may deviate significantly from laboratory values, even if the effect of temperature, pressure and pore-fluid is accounted for. The reason for this problem is again a certain scale dependence in which different aspects are

involved: in –situ measurements, as a rule, represent an average over a much larger rock volume than laboratory measurements performed on small samples. On the other hand, small-scale variations may thus be lost. Which thermal conductivity is the "correct" one will depend on the specific question (Clauser and Huenges, 1995).

The present thesis is proposed as the first step in trying to fill the lack of knowledge in the field of thermal characterization of geological materials. It is a small part of a research plan whose innovative character is to propose the development of original and standard measurements protocols for the determination of thermo-physical properties of lithic materials considering the microscale dimension as well as meso- and macroscale ones.

The thermal conductivity is one of the main input parameters in geothermal modelling (Andrés et al., 2016) but they are usually defined as input according to bibliographical data for geothermal modelling and by indirect field survey methods. The questions are: how have those bibliographical values been obtained in the past? Are they so reliable and the used techniques reproducible? Chapter 2 reports the results of the literature research conducted in order to find some answers and deals with the thermal conductivity of rock-forming minerals.

Looking for publications regarding thermal properties of rocks, mineralogy immediately assume a crucial role. The natural variation of a rock's mineral content is the reason why all rocks must be arranged into the four main groups linked with their formation conditions: sedimentary, volcanic, plutonic and metamorphic rocks. Then in each group different factors affect the thermal conductivity. The great variability of thermal conductivity values (λ) within the same lithologies can be easily confirmed by consulting the several extensive compilations that have been made for a large number of rocks classified according to rock name and origin. Figure 1.1 clearly shows how porosity (in sediments and volcanic rocks), the dominant mineral phase (in metamorphic and plutonic rocks), and anisotropy (in sediments and metamorphic rocks) are important controlling factors. Among sedimentary rocks, only pore-free sediments show a relatively small variation, because they do not have the strong influence of porosity and pore fluid, but only some variation of chemical composition and impurities (Clauser and Huenges, 1995; Schön, 2011).

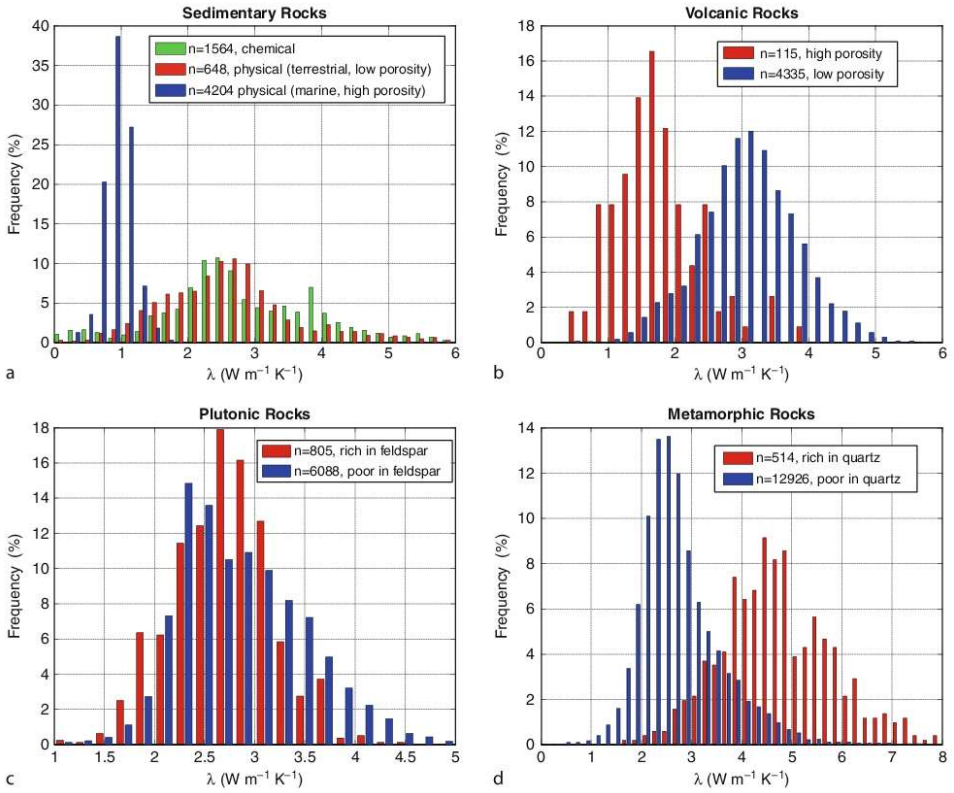

Figure 1.1 Histograms of thermal conductivity for (a) sedimentary, (b) volcanic, (c) plutonic, and (d) metamorphic rocks (Clauser, 2009)

Place these premises, the present work keep the focus on the microscale dimension trying to figure out what role have not only porosity and mineralogy in the thermal behaviour of different groups of rocks, but also rock texture. For the moment, dolomites and trachytes lithologies, representing sedimentary and effusive rocks respectively, have been studied. Chapter 3 provides a description of the two lithologies, of the chosen samples, and of the sampling sites (Val di Non for dolomites and Euganean Hills for trachytes).

Chapter 4 describes the methods with which petrophysical and thermal properties have been measured and computed. Thermal properties have been measured by means a laboratory instruments called C-Therm; a case study regarding in-situ measurements through GRT (Ground Response Test) is reported. Density and porosity have been determined with He Pycnometer and image analysis on scanned surfaces of the rocks. The mineralogical content was investigated though XRD (X-ray Diffraction and Rietveld refinement) and XRF (X-ray Fluorescence). Finally, texture was extrapolated through the μ-XRF (micro-X-ray Fluorescence), a non-destructive technique for the acquisition of elemental X-ray maps of rocks. Helium pycnometer and micro-XR fluorescence

are in particular the two laboratory technique proposed in this thesis for thermal characterization at microscale. The former is considered the most accurate method for porosity measurements while the latter is the most useful source of information, as they can also indirectly provide information on the modal composition of rocks much more quickly than manual point counting under the optical microscope (Germinario et al., 2016).

Chapter 5 presents and discusses the results on dolomites and trachytes separately. Petrophysical properties are discussed individually one from each other, then they are related to thermal conductivity data. On one side the validity of the applied techniques is validated or not, on the other the possible influence of texture, in addition to the mineralogical content, on thermal conductivity is discussed.

Based on the outcomes, the possible considerations are summarized in Chapter 6.

2 Thermal Conductivity of Rock-forming Minerals

When no data are available or no direct measurements can be performed, thermal conductivity can be inferred from a number of indirect data: mineralogical composition and saturating fluids, well-log correlations, and correlations with other physical parameters (Clauser and Huenges, 1995).

If the mineral composition, or mode, of a rock is known, several theoretical models can be used to calculate its composite intrinsic thermal conductivity from table of values for minerals (Robertson, 1988). The discrepancy between the measured thermal conductivity of a rock and its conductivity as computed from the relative abundances and the assumed conductivities of its constituent minerals is probably the results of uncertainties in the conductivities of major minerals (Sass, 1965). These thermal data used for the computation are not measured but they are often bibliographic data the origin of which is rarely or not investigated. Section 2.1 discusses the main methods used to determine thermal conductivity of single-minerals from the ’40s. Section 2.2 reports some of the thermal conductivity data present in literature focusing on minerals constituting lithologies analysed in this thesis (dolomites and trachytes).

Several mathematical models have been proposed to predict the conductivity of a rock from a knowledge of its constituents (Jessop, 1990). Section 2.3 introduces some models that have been developed.

2.1 Methods

There are two specific principal difficulties associated with the measurements of thermal conductivity on mineral samples: purity and sample size (Clauser and Huenges, 1995). As regards sample size, the difficulty lies in the fact that minerals so rarely occur as unflawed crystals of suitable size. Instead of devising a micro-technique for working with very small, single-crystal specimens, it seemed preferable to begin with the rocks themselves and with suitably chosen monomineralic aggregates (Birch and Clark, 1940). Measurements in the literature prior to 1969 were mostly made on relative large samples (Diment and Pratt used machined disks of $0.64 \times 3.81 cm$). When monomineralic aggregates are used instead, uncertainties is introduced by porosity and impurity (Clauser and Huenges, 1995). However, information on anisotropy can be obtained by cutting the disks in appropriate directions (Diment and Pratt, 1988).

Birch and Clark (1940) used a calibrated heater attached to the disk specimen, carefully insulated from the surroundings. Another method used by Birch (1950) and his colleagues is a thermostack, a modified divided-bar technique, which has been widely used for handy measurements of the thermal conductivity of rocks (Horai, 1971).

The divided-bar is a steady-state comparative method in which the temperature drop across a disk of saturated rock is compared with that across a disk of standard material of known conductivity (i. e., quartz) (Popov et al., 1999). Measurements on single crystals or monomineralic, polycrystalline aggregates performed with a divided-bar (or comparable) method requires a minimum sample size (Clauser and Huenges, 1995). On one side, large single crystals that can be machined to the desired size remained relatively rare and on the other side monomineralic aggregates provide uncertainties due to porosity. Trying to overcome those problems a new method has been developed to measure thermal conductivity of monomineralic aggregates at ordinary temperature and pressure. Horai & Simmons (1969) and Horai (1971) use a needle-probe technique to measure the conductivity of finely ground samples (powdered specimens) of minerals saturated with distilled water. This way sample size poses no problem, great purity of sample can be achieved, but all information on anisotropy is lost (Clauser and Huenges, 1995; Diment and Pratt,

1988). Correction of alien mineral phases in samples is possible (Horai, 1971), but requires further microscopic and X-ray examination of the samples (Clauser and Huenges, 1995).

Needle-probe method was described by Von Herzen and Maxwell (1959). The validity of the technique on monomineralic polycrystalline aggregates was tested. Moreover, questions remain as to the systematics of the orientation of small grains in the needle-probe cell and the correction for fluid content. Comparison between the disk ("standard method") and needle-probe measurements is fairly good, but the scatter is large, as might be expected (Diment and Pratt, 1988).

In the same years, Sass et al. (1970) developed a new method of measuring thermal conductivity of minerals. The thermal conductivity of a mixture of mineral powder with distilled water was measured by a divided-bar apparatus (described by Beck, 1957), and the conductivity of mineral is derived from the conductivity of mixture by a method similar to that described by Horai. One of the disadvantages of the method is that the anisotropic conductivity of the crystal is disregarded. What is obtained is the averaged conductivity, which corresponds to the conductivity of the monomineralic aggregate (Horai, 1971).

The interpretation of measurements of thermal conductivity on fragments is not without ambiguity, as pointed out by Sass et al. (1971): their comparison between Horai & Simmons' (1969) transient needle-probe method and their steady-state divided-bar "cell" method on splits from Horai & Simmons's (1969) original mineral samples indicates that the results obtained from measurements on fragments depend on both the measurement technique and the model used for inferring the thermal conductivity of the solid constituents of the mixture.

A more recent laboratory method for thermal conductivity measurements is the optical scanning that was perfected in the 1980s and 1990s and then applied to geo-physical problems. After establishing that the precision and accuracy were satisfactory, the optical scanning method was adapted for the study of thermal conductivity and diffusivity of mineral samples (Popov et al., 1987). The theoretical model is based on scanning a sample surface with a focused, mobile and continuously operated constant heat source in combination with a temperature sensor. The heat source and sensor move with the same speed relative to the sample and at a constant distance to each other (Popov et al., 1999).

An aspect not to be overlooked is that thermal conductivity, like any other physical property, originates in the microscopic behaviour of the solid (Hofmeister, 2001). For this reason, a chapter dedicated to thermal conductivity cannot fail to mention the theory of solid-state physics. According to this theory, thermal conductivity in dielectric solids can be considered to be the propagation of phonons, or quantized lattice vibrational energy, through the crystal (Horai, 1971). The subject of *lattice dynamics* is the study of the vibrations of the atoms in a crystal. Thus, we need to understand lattice dynamics for a number of key applications. The propagation of sound waves in crystal are a practical example of the role of lattice dynamics, as also is the interaction of materials with light. Lattice dynamics also gives us properties such as thermodynamics, superconductivity, phase transitions, thermal expansion, and also thermal conductivity (Dove, 2011). Accordingly, the thermal conductivity of rock is determined by both the mineral composition and the lattice dynamical character of the individual rock-forming minerals (Horai, 1971).

Models of heat transport must account for the two mechanism considered to be dominant (Hofmeister, 2001, 2006):

- through physical contact, at all temperatures, phonons exchange heat when colliding with each other. If the phonons have long lifetimes (e.g., at cryogenic temperatures), it is possible that interactions also occur with defects or grain boundaries. Transport of heat by scattering of phonons within each individual minerals grain is termed lattice conductivity (k_{lat}).
- heat is simultaneously transported through absorption of incident radiation; heat is also moved when photons emitted by any given grain in the medium are absorbed by nearly grains.. This diffusive radiative process is described by an effective thermal conductivity ($k_{rad,dif}$). But below about $\sim 800K$, k_{rad} is negligible, and thus k_0 arises solely from the lattice contribution.

The phonon component of thermal diffusivity can be measured through laser-flash analysis (LFA). The laser-flash method was firstly introduced by Parker (1961) and over the past few decades, it has developed into one of the most widely used techniques for measuring the thermo-physical properties (thermal diffusivity, specific heat and thermal conductivity) of various kinds of solids, powders and liquids (Min et al., 2007). The contact-free LFA removes spurious

photon transfer and accurately (~2% uncertainty) provides the component of heat transfer originating through phonon scattering (lattice conductivity, k_{lat}) (Hofmeister and Pertermann, 2008). Easy sample preparation, fast measurement times and high accuracy are only some of the advantages of this non-contact, non-destructive testing technique (Min et al., 2007). The acquisition procedure consists in few steps: (1) sample preparation, (2) selection of crystallographic orientation and polarization, (3) chemical characterization, (4) near-IR to visible spectroscopy, (5) laser-flash analysis and data processing. In this way, spinels and olivines ((Hofmeister, 2001), garnets at high temperature (Hofmeister, 2006), clynopyroxenes at elevated temperature (Hofmeister and Pertermann, 2008), single-crystal MgO and Al_2O_3 (Hofmeister, 2014) have been studied.

2.2 Bibliographic data

As described in the previous section, different techniques have been used on differently prepared specimens for the determination of rock-forming minerals thermal conductivity. Table 2.1 presents data from various references and measured both on single crystals as well as on natural monomineralic, polycrystalline aggregates, and on artificial monomineralic aggregates produced from a mixture of powdered mineral specimens and distilled water. Data from two sources are presented:

- Clauser and Huenges (1995) who report measurements performed or reported previously by Diment & Pratt (1988) (they report measurements performed by Sass (1965), Ratcliffe (1959), Birch & Clark (1940)), Dreyer (1974), and Horai (1971) including Horai & Simmons (1969);
- Schon (2011), a compilation of data measured by a variety of researchers including Cermak & Rybach (1982), Brigaud et al. (1989, 1992), Melnikov et al. (1975), Drury & Jessop (1983).

Data reported in Dreyer (1974) are averages over an unspecified number of individual measurements. The data in Horai (1971) consist of individual needle-probe measurements on water-saturated mineral powder. Ambient conditions are specified as “ordinary temperature and pressure” by Horai (1971) and as “room temperature” by Dreyer (1974). Diment & Pratt (1989) quote specific temperature and pressure conditions during measurements for most of the data they report (Clauser and Huenges, 1995).

Among all data, a selected group of mineral have been analysed for the purposed of the thesis. In particular, the major mineral phases constituting trachytes and dolomites have been considered.

Figure 2.1 shows the measured values for the two orientations in the quartz single crystal performed by Ratcliffe (1959) and Birch & Clark (1940) at 30°C, and by Dreyer (1974) at room temperature. They report thermal conductivity components normal $\lambda_{\perp}$ and parallel $\lambda_{\shortparallel}$ to the crystal's optical c-axis of $6.15 - 6.5\ \mathrm{W/mK}$ and $10.17 - 11.3\ W/mK$ respectively. Horai (1971) performed the measurements on aggregates composed by distilled water-saturated mineral powder and report a value of $7.69\ \mathrm{W/mK}$. Measurements made by Cermak & Rybach (1982) and Brigaud et al. (1989, 1992) confirm this same value. Griffith et al. (1992) and Rzhewski and Novik (1971) note that there is a difference of the conductivity values between monocrystal, polycrystal, and fused minerals. For quartz in particular, they report a variation between a maximum of $11.7\ Wm^{-1}K^{-1}$ (monocrystalline), through $3.6\ Wm^{-1}K^{-1}$ (polycrystalline), to $1.39\ Wm^{-1}K^{-1}$ (fused). The difference between mono- and polycrystalline results from intergrain contact effects (Schön, 2011).

Feldspars minerals are even more prevalent than quartz in common rocks, and so are also very important in affecting the conductivity of rocks (Robertson, 1988). Sass (1965) presents the results of measurements on fifteen specimens of feldspar, thirteen from single crystals and two from aggregates of average grain size $1\ to\ 2\ mm$ (see Figure 2.2). The measurements were performed (at a mean specimen temperature of 25°C) with the divided bar apparatus described by Beck (1957). Birch & Clark (1940) made measurements on four plagioclase aggregates and found the average of $4.5\ mcal\ cm^{-1}\ sec^{-1}\ °C^{-1} = 1.9\ W/mK$. This became the commonly quoted value for feldspars but it seems to be not representative of feldspars as a whole because measured conductivities are frequently much higher than computed ones (Sass, 1965). The arithmetic mean of the fifteen values is $5.7 \pm 0.2\ mcal\ cm^{-1}\ sec^{-1}\ °C^{-1} = 2.4\ W/mK$. The main conclusion arising from these measurements is that the range of variation of the thermal conductivities of feldspars is great (Sass, 1965).

Figure 2.3 present zircon values from Dreyer (1974) on single crystal, Horai (1971) on aggregate, and Melkinov et al. (1975). Data referring to single mineral are lower than the other two. Dreyer (1974) report thermal conductivity

components normal λ_{11} and parallel λ_{33} to the crystal's optical c-axis of 3.9 W/mK and 4.8 W/mK respectively. Horai (1971) measured 5.54 W/mK and Melkinov (1975) 5.7 W/mK.

Comparing the data in the first two columns, Clauser & Huenges (1995) noted a bad agreement on magnetite data and explained this with lattice imperfections that lead to a significant decrease in thermal conductivity. Figure 2.4 presents data from various sources. The lower value is $4.61 \pm 0.42\ W/mK$ (mean and standard deviation on 8 samples); the higher is 9.7 W/mK measured by Dreyer (1974) along optical a-axis.

Figure 2.5 reports data of the other oxide, ilmenite. Diment & Pratt (1988) measured $1.49 \pm 0.02\ W/mK$ (mean and standard deviation from 3 samples). Horai (1971) measured $2.38 \pm 0.18\ W/mK$. $2.2\ W/mK$ is the thermal conductivity measured by Melkinov et al. (1975).

Apatite values variate on a little range from $1.27 \pm 0.02\ W/mK$ to 1.4 W/mK (Figure 2.6).

Obviously sheet silicates show high anisotropy due their natural structure. In Figure 2.7 biotite data are plotted. Values spread on a range between $0.52 \pm 0.01\ W/mK$ (component perpendicular to the direction of maximum thermal conductivity) to $3.14\ W/mK$ (component parallel to the direction of maximum thermal conductivity).

Among pyroxenes, data related to diopside-augite were considered and plotted in Figure 2.8. There is a good agreement: thermal conductivity varies from $4.1\ to\ 4.66 \pm 0.31\ W/mK$.

As regards carbonates, dolomite ($CaMg(CO_3)_2$) has a higher thermal conductivity than calcite ($Ca(CO_3)$). Horai (1971) observed the relationship between density, thermal conductivity, and mean atomic weight. He derived it from the data on rock-forming minerals. Figure 2.9 shows the clear dependence on thermal conductivity of mean atomic weight. The dolomite has a mean atomic weight of 18.44 while the latter has a mean atomic weight of 20.02. The structure in another important factor. Indeed, dolomite is a rhombohedral carbonate with a structure consisting of an ordered arrangement of alternating layers of Ca^{2+} and Mg^{2+} cations interspersed with CO_3^{2-} anion layers normal to the *c*-axis (Gregg et al., 2015). This is the main reason why its symmetry ($R\bar{3}$) is lower than ($CaCO_3$) $R\bar{3}c$ symmetry.

*Table 2.1 Thermal conductivity λ (W/mK) of different rock-forming minerals.**

	Clauser & Huenges (1995)			Schon (2011)
	Diment & Pratt (1988)	Dreyer (1974)	Horai (1971)	
Mineral	**T, state, λ, (n)**	**state, λ**	**state, λ, (n)**	**λ**
	ZIRCON GROUP			
Zircon $[ZrSiO_4]$		λ_{11}: **3.9**, λ_{33}: **4.8**	a: **5.54**	**5.7** (M)
	FELDSPAR GROUP			
Orhoclase $K[AlSi_3O_8]$	30°C, (100): **2.34** ± **0.08** (2) S 30°C, (010): **2.68** S 30°C, (001): **2.30** ± **0.21** (2) S		a: **2.31**	**2.40** (DJ)
Microcline K[AlSi3O8]	?°C, (001): **2.04** S		a: **2.49** ± **0.08** (3)	**2.9** (M), **2.49** (CR)
Albite Na[AlSi3O8]	25°C, a: **2.34** S	a: **2.0** ± **0.1**	a: **2.14** ± **0.19** (4)	**2.31** (CR)
Anorthite Ca[AlSi3O8]	25°C, a: **2.72** S	a: **2.1**		**1.68** (CR)
Feldspar-mean				**2.3** (H), **2.0** (DJ)
	SILICA GROUP, SiO_2			
α quartz	30°C, ⊥: **6.15** (R), ‖: **10.17** (BC)	λ_{11}: **6.5**, λ_{33}: **11.3**	a: **7.69**	**7.69** (CR), **7.7** (B)
α quartz ⊥	T/λ, x: 0/**6.82**, 50/**5.65**, 100/**4.94**, 150/**4.44**, 200/**4.06**, 250/**3.73**, 300/**3.52**, 350/**3.31** (BC)			
α quartz ‖	T/λ, x: 0/**11.43**, 50/**9.38**, 100/**7.95**, 150/**7.03**, 200/**6.32**, 250/**5.69**, 300/**5.15**, 350/**4.73** (BC)			
silica glass	30°C, amorphous: **1.38** (R)		a: **1.36**	
silica glass	T/λ, amorphous: 0/**1.36**, 50/**1.44**, 100/**1.48**, 150/**1.53**, 200/**1.58**, 250/**1.64**, 300/**1.70**, 350/**1.78**, 400/**1.85**, 450/**1.94**, 500/**2.07** (BC)			
	OXIDES			
Magnetite iso (Fe_3O_4)	22-33°C, a: **4.61** ± **0.42** (8)	λ_{11}: **9.7**	a: **5.10**	**4.7**-**5.3** (M), **5.1** (CR)
Ilmenite $(FeTiO_3)$	35°C, a: **1.49** ± **0.02** (3)		a: **2.38** ± **0.18** (2)	**2.2** (M)
	PHOSPHATES			
Apatite	35°C, a: **1.27** ± **0.02** (3)		a: **1.38** ± **0.01** (2)	**1.4** (M), **1.37** (CR)
	MICA GROUP			
Muscovite $KAl_2[AlSi_3O_{10}][OH]_2$	30°C, ‖: **3.89** (2) 32-45°C, ⊥: **0.62** ± **0.11** (4)		a: **2.28** ± **0.07** (3)	**2.32** (CR)
Biotite $[AlSiO_{10}](OH,F)_2$	33°C, ‖: **3.14** 32°C, ⊥: **0.52** ± **0.01** (2)		a: **2.02** ± **0.32** (2)	**0.7**-**1.6** (M)
Smectite				**1.9** (B)
Illite				**1.9** (B)
Clay minerals (mean)				**2.9** (Q), **1.7** (Ca)
	PYROXENE GROUP $(Na,Ca)(Mg,Fe,Al)(Al,Si)_2O_6$			
Diopside, augite	35°C, a: **4.23** ± **0.05** (4)		a: **4.66** ± **0.31** (4)	**4.1**-**5.1** (M)

Table 2.1 (continued)

	Clauser & Huenges (1995)			Schon (2011)
	Diment & Pratt (1988)	Dreyer (1974)	Horai (1971)	
Mineral	**T, state, λ, (n)**	**state, λ**	**state, λ, (n)**	**λ**
	CARBONATES			
Calcite $CaCO_3$	30°C, ⊥: **3.16**, ∥: **3.63** (BC)	λ_{11}: **4.2**, λ_{33}: **5.0**	a: **3.59**	**3.25**-**3.9** (M)
Calcite ⊥	T/λ, x: 0/**3.48**, 50/**3.00**, 100/**2.72**, 150/**2.52**, 200/**2.37**, 250/**2.25**, 300/**2.16**, 350/**2.09**, 400/**2.06** (BC)			
Calcite ∥	T/λ, x: 0/**4.00**, 50/**3.40**, 100/**2.99**, 150/**2.73**, 200/**2.55**, 250/**2.41**, 300/**2.29**, 350/**2.20**, 400/**2.13** (BC)			
Dolomite $CaMg(CO_3)_2$	25-35°C, a: **4.78** ± **0.54** (70)	a: **4.9**	a: **5.51**	**5.5** (CR), **5.3** (B)

*minerals marked "iso" are isotropic. T is ambient temperature, and (n) is number of data for mean and standard deviation. "x" denotes measurements of unknown orientation on single crystals, "a" on monomineralic aggregates. Directions of anisotropy are specified in one of three ways: (1) by the mineral's optical a-, b-, or c-axes (100, 010, 001), (2) by the diagonal elements of the thermal conductivity tensor ($\lambda_{11}\lambda_{22}\lambda_{33}$), where λ_{33} is parallel to the crystal's optical c-axis, and the optical a-axis lies within the plane defined by λ_{11} and λ_{22}, (3) by the thermla conductivity components normal or parallel to the direction of maximum thermal conductivity (⊥,∥). Compiled data from: B: Brigaud et al. (1989, 1992); BC: Birch & Clark (1940); C: Clark (1966); Ca: Clauser (2006); CR: Cermak and Rybach (1982); DJ: Drury and Jessop (1983); H: Huenges (1989); M: Melnikov et al. (1975); Q: Quiel (1975); R: Ratcliffe (1959); S: Sass et al. (1965).

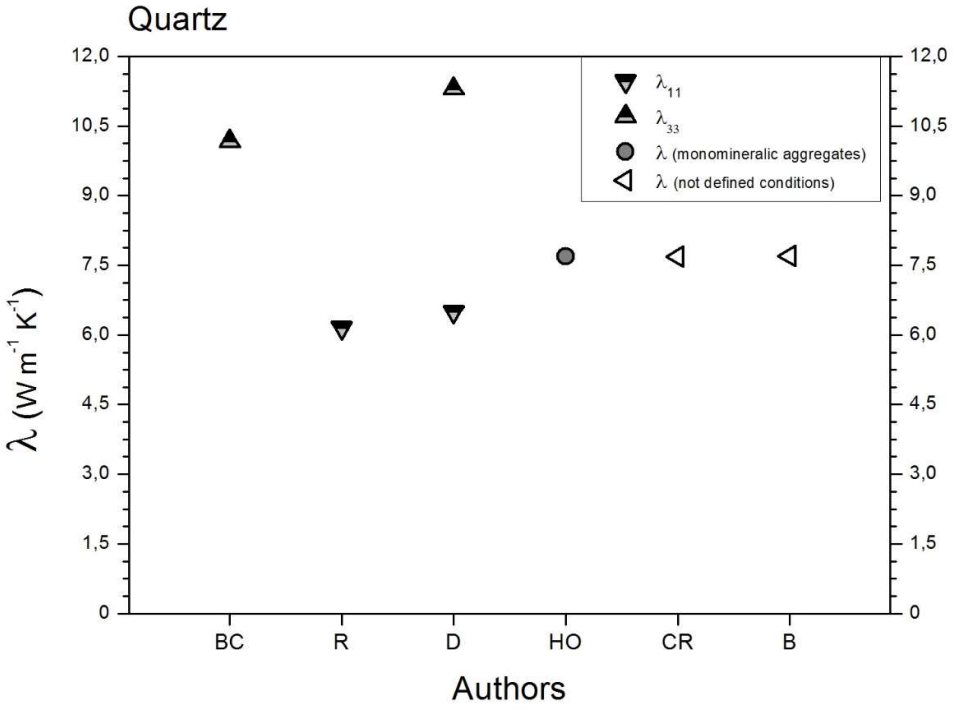

Figure 2.1 *Literature thermal conductivity values for quartz. Compiled data from: BC: Birch & Clark (1940); R: Ratcliffe (1959); D: Dreyer (1974); HO: Horai (1971); CR: Cermak & Rybach (1982); B: Brigaud et al. (1989, 1992).*

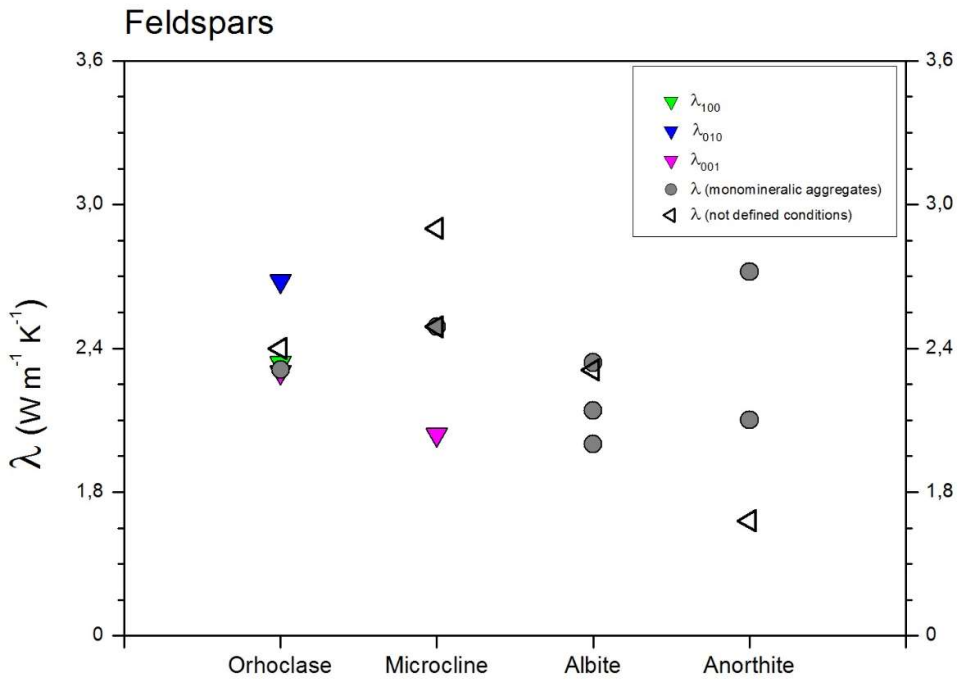

Figure 2.2 *Literature thermal conductivity values for feldspars (orthoclase, microcline, albite, anorthite). Compiled data from: Sass et al. (1995), Cermak & Rybach (1982), Drury & Jessop (1983), Melkinov et al. (1975).*

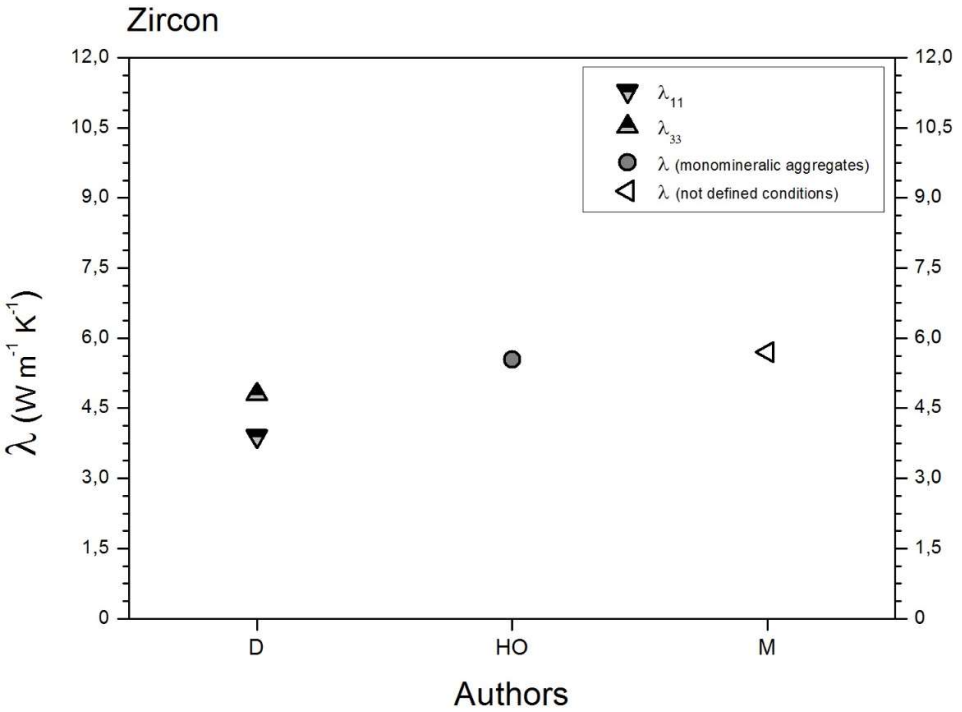

Figure 2.3 *Literature thermal conductivity values for zircon. Compiled data from: D: Dreyer (1974); HO: Horai (1971); M: Melkinov (1975).*

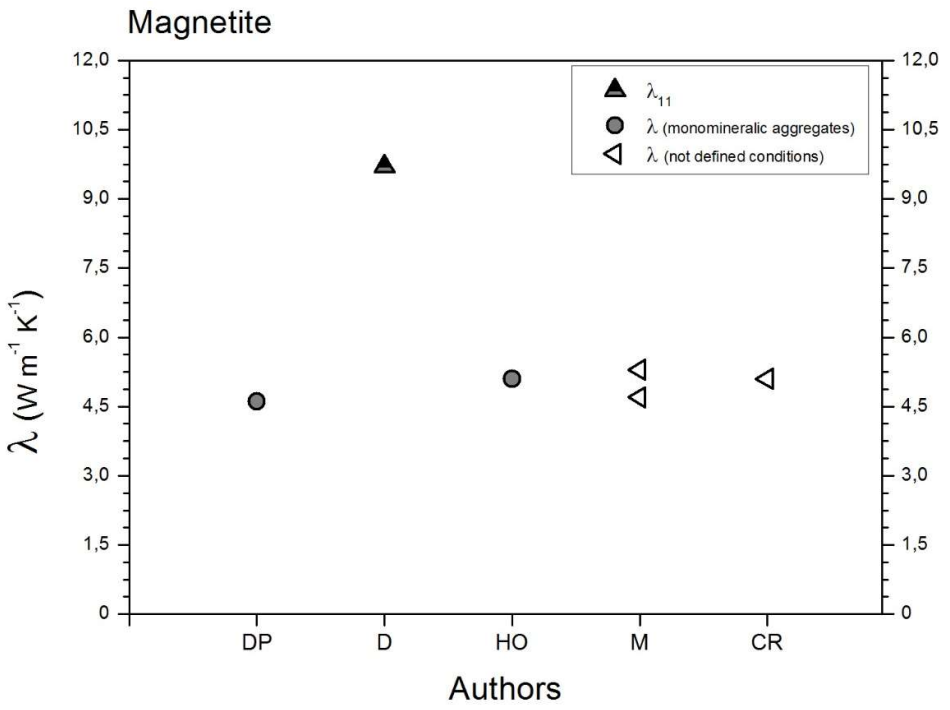

Figure 2.4 *Literature thermal conductivity values for magnetite. Compiled data from: DP: Diment & Pratt (1988); D: Dreyer (1974); HO: Horai (1971); M: Melkinov (1975); CR: Cermak & Rybach (1988).*

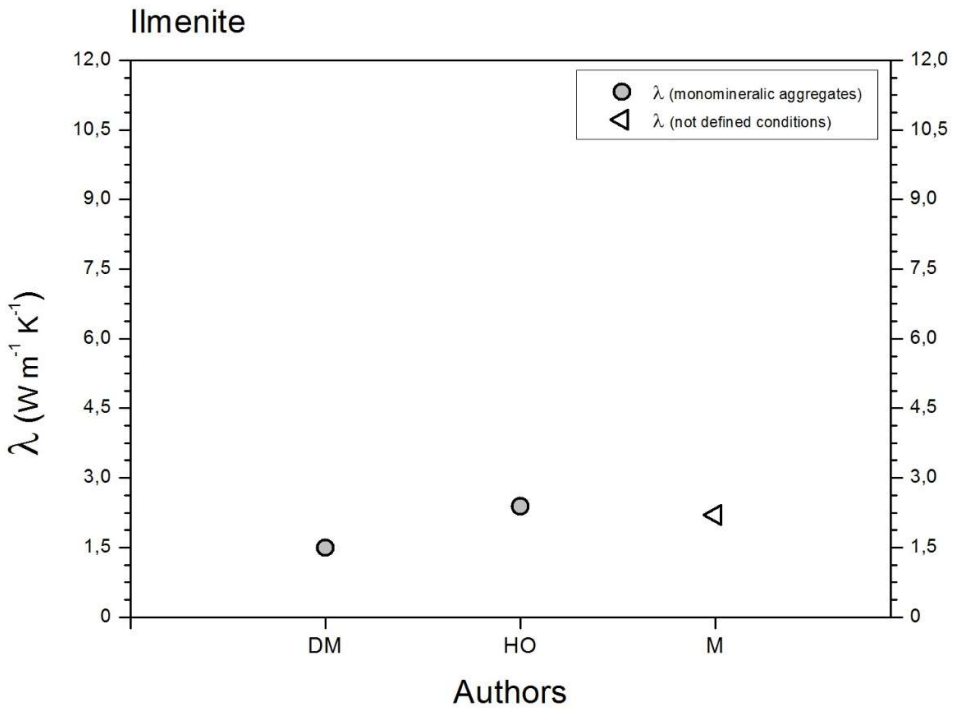

Figure 2.5 *Literature thermal conductivity values for ilmenite. Compiled data from: DP: Diment & Pratt (1988); HO: Horai (1971); M: Melkinov (1975).*

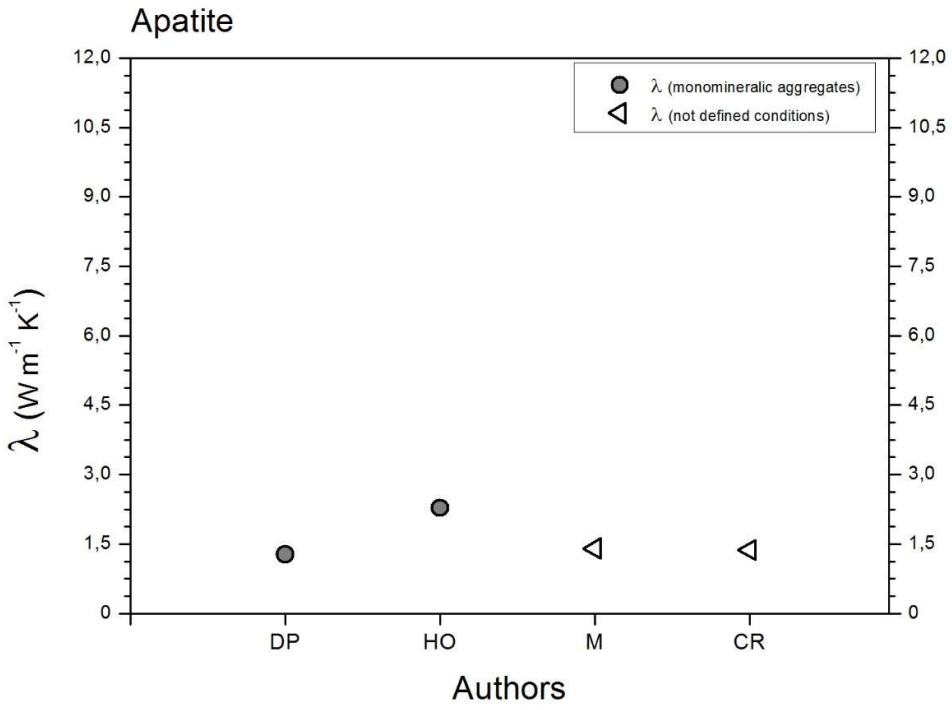

Figure 2.6 *Literature thermal conductivity values for apatite, augite. Compiled data from: DP: Diment & Pratt (1988); HO: Horai (1971); M: Melkinov (1975); CR: Cermak & Rybach (1982).*

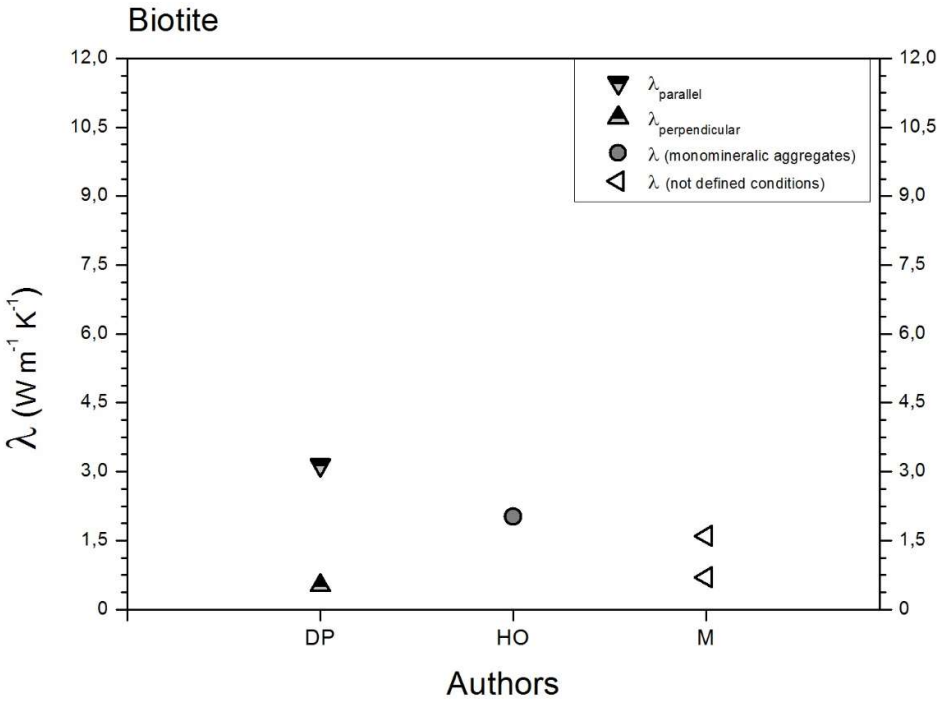

Figure 2.7 *Literature thermal conductivity values for biotite. Compiled data from: DP: Diment & Pratt (1988); HO: Horai (1971); M: Melkinov (1975).*

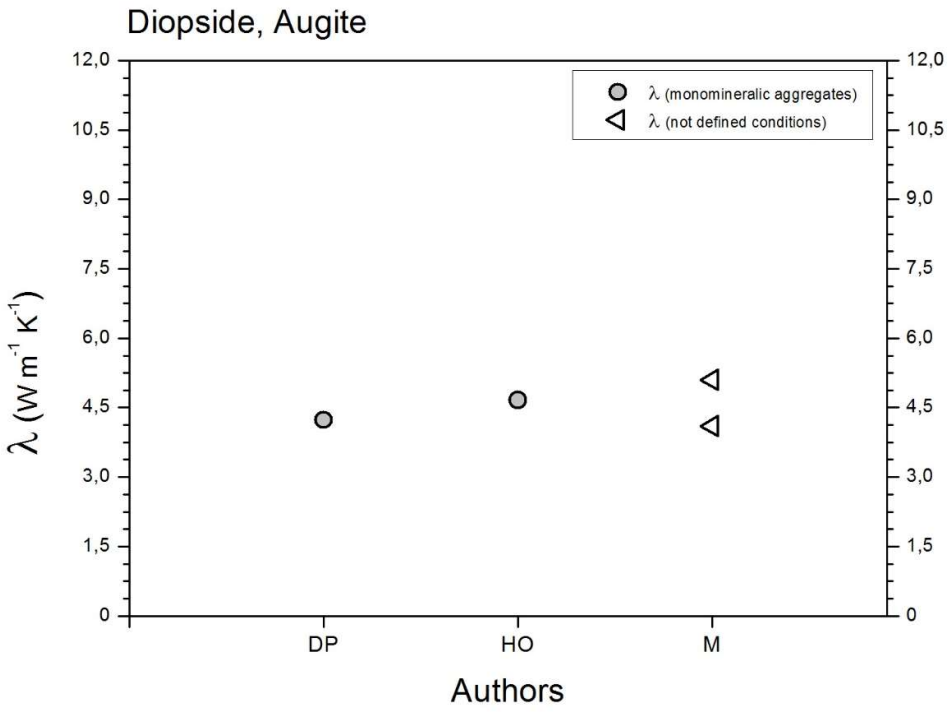

Figure 2.8 *Literature thermal conductivity values for diopside, augite. Compiled data from: DP: Diment & Pratt (1988); HO: Horai (1971); M: Melkinov (1975).*

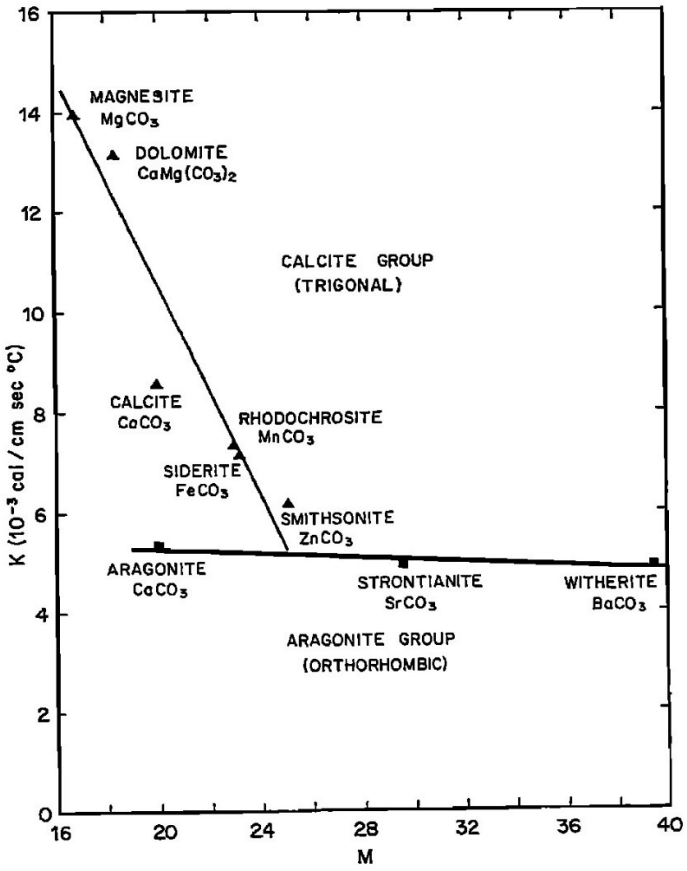

Figure 2.9 *Thermal conductivity versus mean atomic weight for carbonate (from Horai, 1971).*

2.3 Models

Thermal conductivity of rocks may be estimated from their mineral content, as minerals, due to their well defined composition, exhibit a much smaller variance in thermal conductivity than rocks (Clauser and Huenges, 1995). Anyway, thermal conductivity as a tensor depends not only on the volume fraction and thermal conductivity of rock components, but also on their distribution, on geometry and internal structure, and on the heat transfer conditions at the contacts between them (Schön, 2011).

Several mathematical models have been proposed to predict the conductivity of rock from a knowledge of its constituents. Each one employs a different mathematical formulation to account for the distribution of the conductivities within the mineral matrix (Jessop, 1990). All have their disadvantages: some overestimate while others underestimate systematically the true bulk thermal conductivity (Clauser and Huenges, 1995).

Bound Models	**Inclusion Models (Spherical and Nonspherical Inclusions**	
Layer model: Voigt (1910) and Reuss (1929) bound	Random orientation	Aligned orientation
Hashin-Shtrikman (1962) bounds	Clausius-Mossotti model: Berryman (1995)	Berryman (1995)
Modifications: Krischer and Esdorn (1956), Lichtenecker and Rother generalization (1931)	Describes fractured and (low) porous rocks, implements inclusion shape (aspect ratio) and orientation: random orientation (isotropic) or aligned orientation (anisotropic)	

Table 2.2 *Overview to some model concepts for thermal conductivity (from Schon, 2011)*

Table 2.2 shows an overview to some model concepts for thermal conductivity. Schon (2011) presents an overview of two groups of models related to thermal conductivity:

- Layer or laminated models, their modifications and comparable mixing rules
- Inclusion models.

In the first group, a rock consisting of n components can be idealized in the simplest case as a layer model following Voigt's and Reuss's concepts. Parallel (heat flow parallel to boundary between components) and series (heat flow

perpendicular to boundary between components) model are easy to understand, but have the disadvantage of being rather special cases, applicable mostly to bedded sediments (Clauser and Huenges, 1995). Experimentally determined data are situated between the two boundaries given by the series and the parallel model. There are different theoretical developments to obtain a better approximation between calculated and measured. A simple combination of the two fundamental models is their arithmetic mean; another model with a simple mathematical expression is the geometric mean (Schön, 2011). Beck (1988) reviews the topic in considerable detail, and, in particular, presents and discusses several other well known mixing-models.

Models of conductive and convective heat flow strictly depend on heat transport properties of minerals. The thermal conductivity consists of a lattice and a radiative component, and any extrapolation procedure requires a knowledge of the relative contribution of each component to the total and a theoretical knowledge of the temperature dependence of each component (Roufosse, 1974).

Thermal conductivity can be predicted through semi-empirical models. Hofmeister (1999) developed the spectroscopic model of thermal conductivity which is based on the concept of damped harmonic oscillators and provides good agreement with experiment. This semi-empirical model calculates the lattice (phonon) contribution (k_{lat}) from IR reflectivity and sound velocities, and calculates the radiative contribution from the vibrational overtones and electronic bands (Hofmeister, 2001). Giesting and Hofmeister (2002) developed a semi-empirical model that relates thermal conductivity to spectroscopic data.

The heat transfer by phonon is characterized by the mean acoustic velocity and mean free path length of phonons. Similarly to diffusion in kinetic gas theory, thermal diffusion by phonons can be expressed as:

$$D = \frac{1}{3} v l \tag{2.1}$$

where v corresponds to the mean velocity of phonons and l represents the mean free path length of a phonon. With increasing temperature the number of phonon-phonon interactions increases, reducing the mean free path length of phonon (Kittel, 1981; Höfer and Schilling, 2002, Berman, 1976).

The theory also shows that the velocity of phonons depends on the interatomic force constant. This explains why the structure of the silicon-oxygen network controls the thermal behaviour of silicates. The role played by silicon-oxygen tetrahedral in thermal conduction was already pointed out by Birch and Clark (1940). Now it is known that the velocity of phonons is larger if the force acting between the atoms in the crystal are stronger. Since the bond between silicon and oxygen is stronger than any other bonds in the silicate crystal, phonons will be transmitted most effectively through the silicon-oxygen framework (Horai, 1971).

3 Samples

The major aim was to suggest a multiscale approach and to understand which techniques and laboratory methods could be used to obtain a thermal characterization that take into account the properties at the microscale as well as those at the meso- and macroscale. For this purpose, analysing a single lithology was not recommended. We wanted to apply the methodology on different type of rocks in order to test its validity in different conditions. For the moment, dolomites and trachytes have been studied.

3.1 Dolomites – Rio Maggiore mine (TN)

During a previous study conducted by Alessandra De Lullo, eight samples of Dolomites were collected from a Val Di Non (Trento Province, Italy) site, the Rio Maggiore mine, and a thermo-physical properties analysis was conducted on them (De Lullo, 2016).

The Rio Maggiore dolomite mine (see Figure 3.1) is known for the reutilization of the chambers formed after extraction of the dolomite as conservation storage of apples produced in Val di Non and for two large irrigation water reservoirs for the overlying agriculture. The aquifer is used to supply drinking water to the village of Prio and to cool the systems that manage the preservation of the fruit at approximately 1°C. The temperature inside the mine is around 10°C. The aquifer water also supplies the underground irrigation reservoirs. The use of the excavated chambers for the preservation of fruit offers considerable energy savings (Fuganti et al., 2013).

The Rio Maggiore mine is located in Val di Non within the territory of the villages of Vervo and Taio. The exploited dolomite rock types are referred to Jurassic age and represent the dolomite heteropy of Calcari Grigi and Rosso

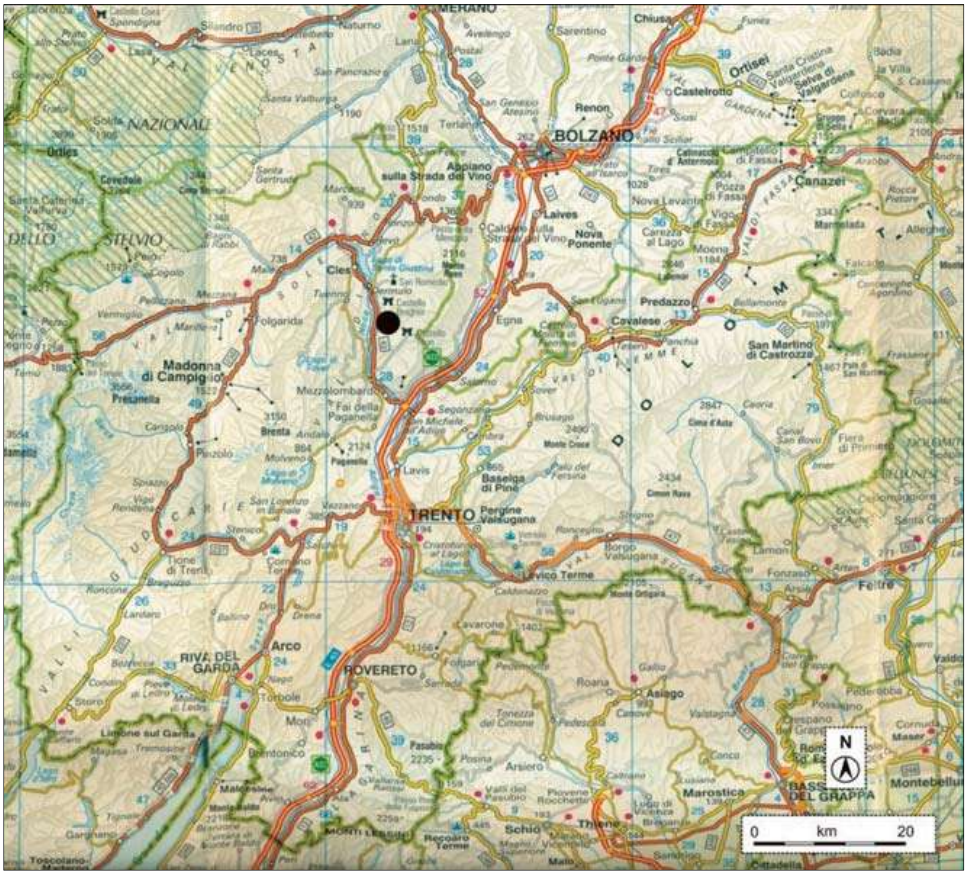

Figure 3.1 *Black dot indicates Rio Maggiore mine.*

Ammonitico. The types of dolomite include: m-cyclicities, mm-cyclicities, dolomite breccias, fossil-bearing dolomite, microcrystalline dolomite in which all the original limestone structures have been overlaid by the new mosaic, saccaroidal dolomite, dolomite with bird-eye structures, and stromatolite dolomite. The basal portion of the dolomite (Lias) is related to a shallow sea system which is so-called "Trento platform". The deep sea corresponds to the depositional environment of the upper section instead.

The eight dolomite rock samples attracted our attention because, despite the same lithology, the samples revealed very heterogeneous thermal properties (Table. 3.1) so they were the perfect candidate for the new microscale approach. Thus three of these dolomites were selected for further investigations (see Figure 3.2). The choice was based on the mean thermal conductivity values measured by De Lullo, so samples with higher (C-B-Dol_007; $\lambda = 5.2006\ W/mK$), lower (C-B-Dol_004; $\lambda = 3.4892\ W/mK$), and intermediate (C-B-Dol_002; $\lambda = 4.9823\ W/mK$) conductivity were chosen (dotted boxes on Table 2.1).

Table 3.1 *Summary of the main results obtained by De Lullo (2016) on 8 samples of dolomite from Rio Maggiore (TN). Despite the same lithology, note the heterogeneity on thermal conductivity values.*

Sample	Open Porosity [%]	Density [g/cm^3]	Thermal Conductivity [W/mK]
C-B-Dol_001	1.593	2.7827	3.8006
C-B-Dol_002	3.7211	2.7347	4.9823
C-B-Dol_003	2.0451	2.7717	3.7807
C-B-Dol_004	2.8634	2.742	3.4892
C-B-Dol_005	3.1718	2.7416	3.5108
C-B-Dol_006	1.5765	2.7828	3.6343
C-B-Dol_007	3.0469	2.7394	5.2006
C-B-Dol_008	2.546	2.7442	5.0759

Table 3.2 is a summary of the analysis that was made by De Lullo (2016) and those made in the present work on the three selected sample. Petrophysical properties, namely density and porosity, were studied by De Lullo (2016) and the results are compared with those obtained here with different techniques. Thermal conductivity was measured by De Lullo only. In the present work the three dolomite samples were subjected to a textural analysis.

Table 3.2 *Summary of the analysis performed on three sample s of dolomite.*

Sample	Lithology	Location	Author	Petrophysical properties	Thermal properties	Textural analysis
C-B-Dol_002	dolomite	Val Di Non (TN)	De Lullo (2016)	YES	YES	NO
			present work	YES	NO	YES
C-B-Dol_004	dolomite	Val Di Non (TN)	De Lullo (2016)	YES	YES	NO
			present work	YES	NO	YES
C-B-Dol_007	dolomite	Val Di Non (TN)	De Lullo (2016)	YES	YES	NO
			present work	YES	NO	YES

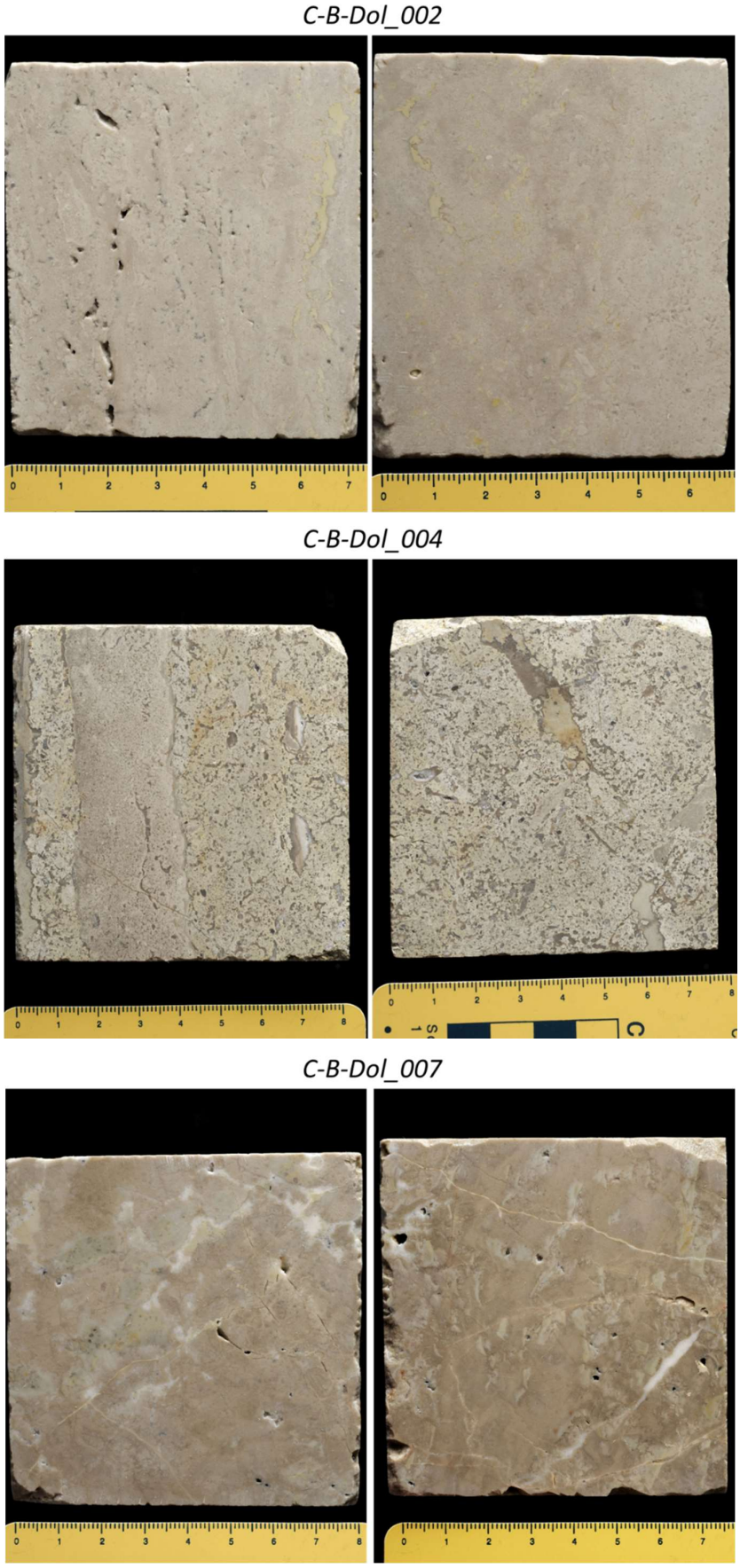

Figure 3.2 *High resolution photos of dolomite samples (De Lullo, 2016).*

3.2 Trachytes – Euganean Hills

The Euganean Hills are located in north-eastern Italy, not far from Padua and extend over an area approximately 100 km^2 wide. They comprise a number of low gently sloping hills (601 m a.s.l. maximum height at Monte Venda) emerging from the alluvial sedimentary cover of the Venetian Plain, and represent the only important magmatic manifestation in the southern part of the Alpine chain (Capedri et al., 2000).

The geology of the Euganean Hills is dominated by two rock series: an Upper Jurassic to Lower Oligocene marine sedimentary sequence mainly composed of limestone and marl, and a series of volcanic and subvolcanic products, diversified in both space and time. The latter represents the most recent magmatic manifestation within the Paleocene-Upper Oligocene Venetian Volcanic Province (VVP). In fact, Euganean Hills are a magmatic district belonging to the VVP (Paleocene-Upper Oligocene), whose magmatism developed during an extensional tectonic regime within the Alpine orogenesis along the southern border of the Trento Platform (Southern Alps), a major structural domain of the northern Adria margin. This magmatic province, which covers an area of $\sim 2000\ km^2$ in NE Italy, also comprise the Berici Hills, close to Vicenza, the Lessini Hills, north of Verona, and the Marosticano, just west of Bassano, where only alkalic basalts were erupted (Bartoli et al., 2013; Capedri et al., 2000; Maritan et al., 2013; Sassi, 2004 and references on them).

The Euganean Hills District is the most recent within the VVP. It developed over a relatively short time-span of 10 Ma (Eocene-Oligocene), during which two main volcanic events are recognised: the older event is Late Eocene in age (42 ± 1.5 Ma, Borsi et al., 1969) and displays the typical features of submarine basic volcanism (pillow lava, breccias, hyaloclastites); the younger event is Oligocene in age (33 ± 1 Ma, Borsi et al., 1969; 32 + 3,5 Ma and 34 + 2 Ma according to Rb-Sr radiometric ages on biotite from trachyte and rhyolite, respectively); and is characterised by the emplacement of acidic and intermediate volcanic and sub-volcanic bodies (domes, plugs, laccolites and dykes) (Maritan et al., 2013 and references on it). The most representative rock types of the Euganean Hills District are Late Eocene to Oligocene trachytes, rhyolites, latites and basalts (Borsi et al., 1969).

In 2014, Stefano Buggiarin performed a study regarding thermo-physical properties of Euganean Hills lithologies related to underground thermal storage feasibility. Forty-seven samples of different lithologies have been collected and among these samples, twenty-one samples have been selected for the laboratory tests and analyses, on the basis of petrographic and structural considerations. Two years later, thin sections of some of the Buggiarin's samples were prepared by Prof. Raffaele Sassi (Professor at the Department of Geosciences of the University of Padova) in order to test the efficiency of a new technique for quick acquisition of elemental X-ray maps of rocks: the μ-XRF. Such a technique was also interesting for our purposes, since it provides quantitative information on texture and rock-forming minerals. Therefore, it was decided to combine the two interests and to analyse precisely those samples. The complete list is reported in Table 3.3. Despite the elemental maps of all thin sections have been acquired, it was possible to elaborate data only for trachytes (sample 1 and 22B in Table 2.2) because this activity requires quite a significant amount of time. All the acquired maps are reported in Appendix A.

Luigi Germinario (PHD at the Department of Geosciences of the University of Padova) studied Euganean trachytes for a long time. He has analysed fourteen trachyte samples collected from nine quarries in Monselice, Monte Merlo, and Monte Oliveto, the localities representing the main historical quarry sites in the Euganean district (Germinario et al., 2016). The micro-XRF technique was used and the same, or similar, elaboration process was followed in both his study and the present work. Among the samples listed in the article, it was decided to take into account trachytes from Monte Merlo quarry with the purpose of making a comparison between Germinario's textural and mineralogical considerations and those made on this M.S. thesis on sample 1 that comes from Monte Merlo as well. In particular, it is of the samples MRL-02, MRL-03, and MRL-05.

Furthermore, Prof. Claudio Mazzoli (Professor in Petrology and Petrography at the Department of Geosciences of the University of Padova) offered two trachyte samples from Zovon for further thermal analyses by the means C-Therm. Dott. Germinario (2016) provided also textural and mineralogical data of these trachytes and he kindly shared those results.

Table 3.3 *List of the thin sections analysed with micro-XRF in Torino. Respective location and lithologies are reported. The terms S:R., B., R.A. in parentheses are referred to the formations of Scaglia Rossa, Biancone and Rosso Ammonitico respectively. The dotted box highlight the two trachyte samples that have been analysed in this M.S. thesis.*

Sample	Place	Formation	Lithology
1	Cava di Montemerlo	Lave trachitiche alcaline	Trachyte
22B	Rocca Pendice	Lave trachitiche alcaline	Trachyte
16	Torreglia	Rioliti alcaline	Rhyolite
39	Monte Rua	Rioliti alcaline	Rhyolite
42	Monte Cecilia	Lava latitica	Latite
43	Baone	Lava latitica	Latite
11	Faedo	Marna euganea	Marl
24	Teolo	Marna euganea	Marl
3 parallela	Teolo	Scaglia Rossa	Limestone (S.R.)
3B ortogonale	Teolo	Scaglia Rossa	Limestone (S.R.)
25	Monte Cecilia	Scaglia Rossa	Limestone (S.R.)
6A parallela	Bastia	Maiolica	Limestone (M.)
6A ortogonale	Bastia	Maiolica	Limestone (M.)
8	Fontanafredda	Maiolica	Limestone (M.)
10B	Fontanafredda	Rosso ammonitico	Limestone (R.A.)
34	Fontanafredda	Rosso ammonitico	Limestone (R.A.)
J 8-3	Tregnago (Monte Bellocca)	Basalt	Basalt
TBD	Abano	Basalt	Olivinic Basalt

Table 3.4 summaries the analyses performed in the present work and by other authors (see Figure 3.3 for the map):

- On samples 1 (from Monte Merlo) and 22B (from Rocca Pendice), previously analysed by Buggiarin (he measured petrophysical and thermal properties), textural and mineralogical analysis and a petrophysical properties evaluation was made; moreover thermal conductivity measurements was repeated in order to check the reliability of Buggiarin data.
- Textural and mineralogical data collected by Germinario on samples MRL-02, MRL-03, and MRL-05 were compared with that of sample 1.
- Thermal conductivity of two cube of trachyte from Zovon (Rovarolla quarry) was measured; data on textural and mineralogical features were shared by Germinario.

Table 3.4 *Summary of the measurements performed by Buggiarin (2014) and in the present work on Euganean Hills trachytes.*

Sample	Lithology	Location	Author	Petrophysical properties	Thermal properties	Textural analysis
1	trachyte	Mt. Merlo	Buggiarin (2014)	YES	YES	NO
			present work	YES	YES	YES
22B	trachyte	Mt. Pendice	Buggiarin (2014)	YES	YES	NO
			present work	YES	YES	YES
LTR_13	trachyte	Zovon (Rovarolla)	Germinario (2016)	NO	NO	YES
RVL_01			present work	NO	YES	NO
RVL_02			present work	NO	YES	NO

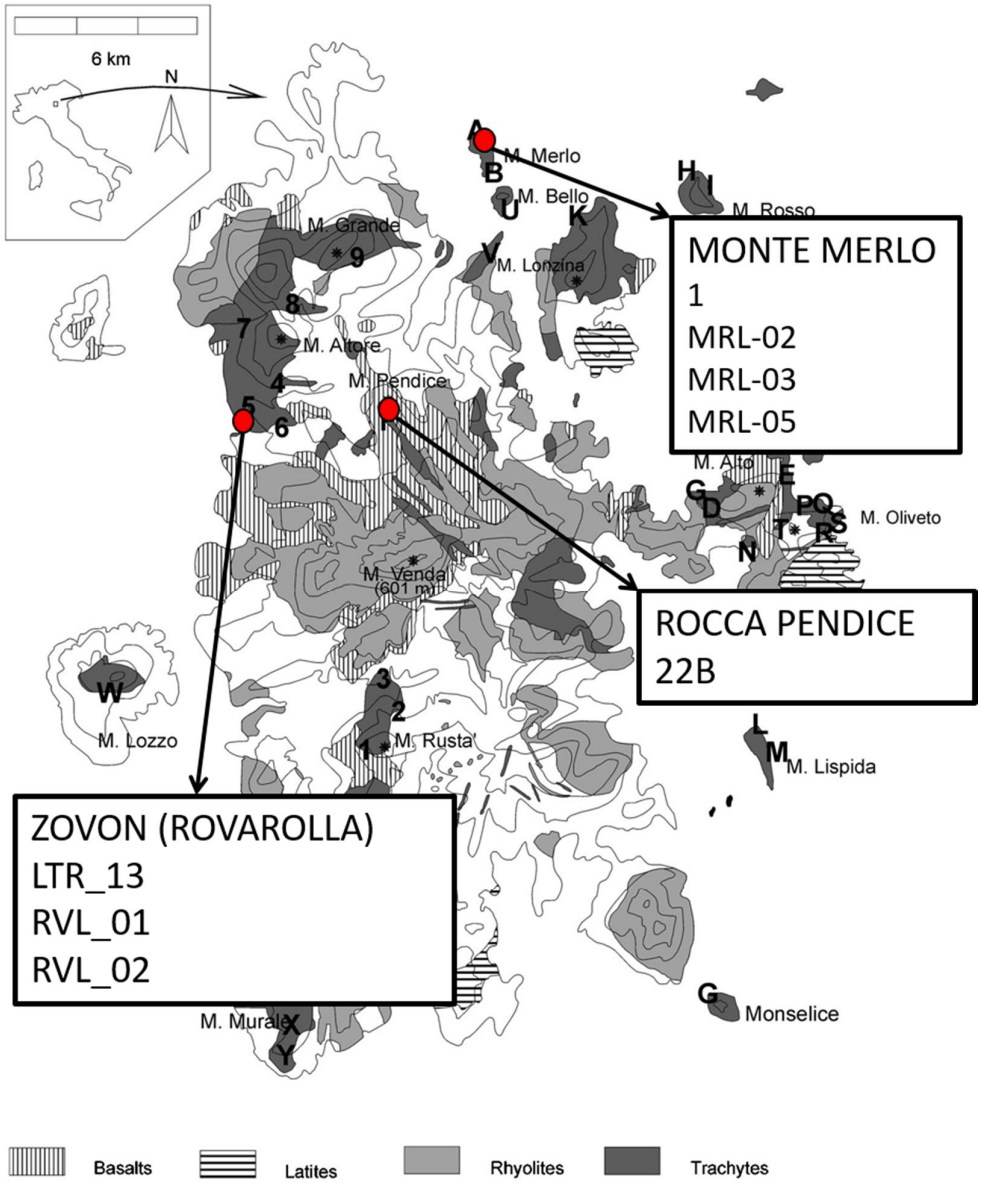

Figure 3.3 *General map of the Euganean Hills, modified after Piccoli et al. The sites (quarries) analysed in the present paper are marked by red circles and for each site the considered samples are reported.*

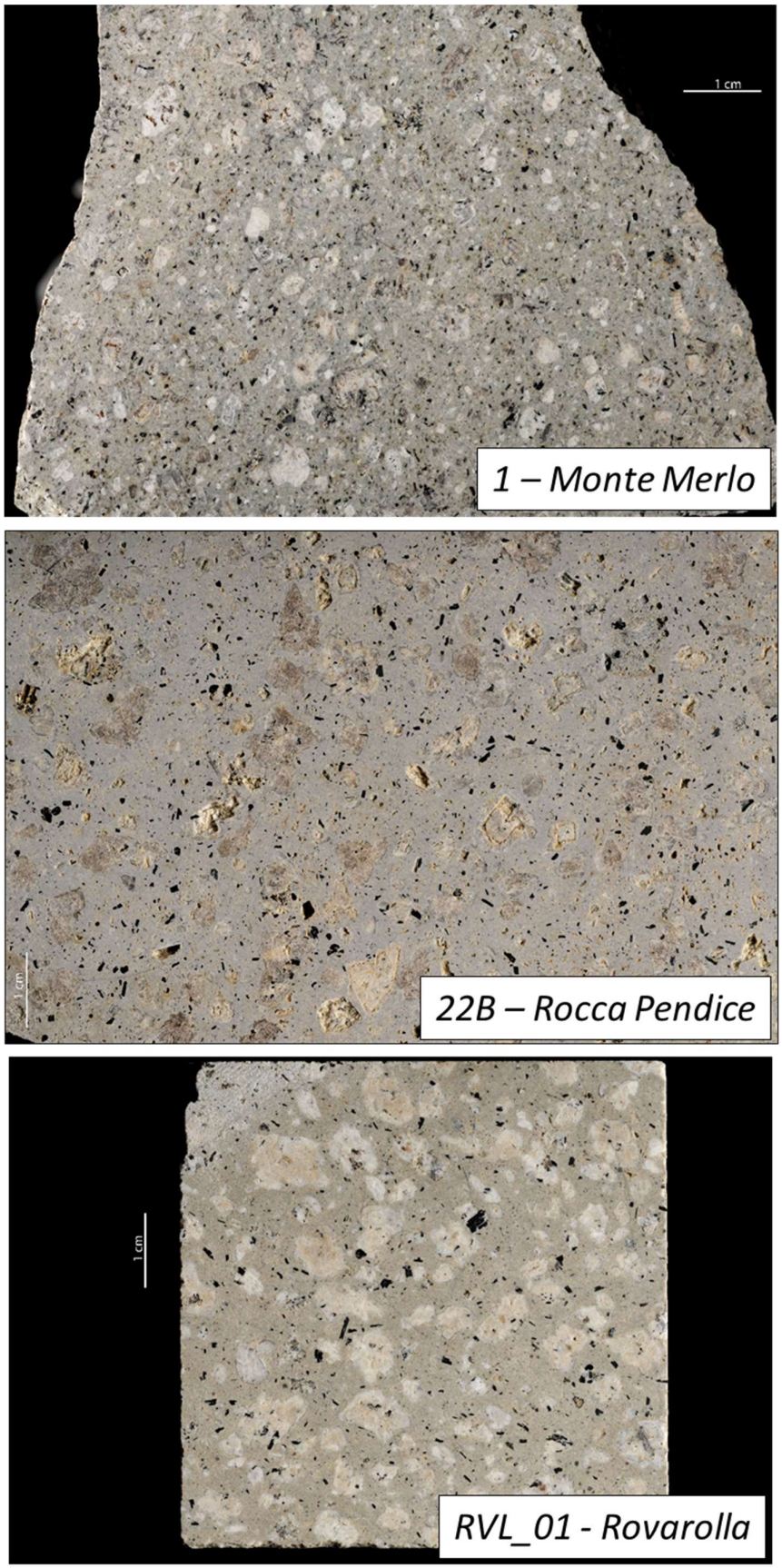

Figure 3.4 *High definition photos of the three samples of trachytes (by Dott. Castelli).*

4 Methods

The following chapter highlights laboratory techniques, analytical procedures and instruments necessary for the acquisition of the results reported in this work.

Section 4.1 starts with a brief description of the main thermal properties; then methods for measure them at two different scales, C-Therm laboratory test at a mesoscale and in-situ measurements (Ground Response Test) at a macro-scale, are described. Section 4.2 shows the two main petrophysical properties, namely density and porosity, and the procedures to measure them. Section 4.3 concerns two different techniques for the mineralogical composition study: X-ray diffraction and X-ray fluorescence. The last section 4.4 deals with the micro-XRF acquisition technique for textural and mineralogical quantitative analysis and summarizes the image analysis performed on the acquired elemental maps.

4.1 Thermal Properties

Geothermal investigations are related to many questions in geoscience, ranging from studies of the physical state of the earth, tectonics, seismicity, and volcanism to practical problems in mining, drilling, geothermal resources, and geothermal methods used in exploration and environmental interest geophysics (Schön, 2011).

Three thermal properties are the most relevant in geothermal investigations (Schön, 2011):

- specific heat capacity c_p
- thermal conductivity λ
- thermal diffusivity a.

Thermal Capacity

Thermal capacity, or specific heat capacity, indicates the capability of a material to store heat and it is given in $J\ kg^{-1}K^{-1} = m^2s^{-2}K^{-1}$. Specific heat capacity is defined as the ratio of the heat input Q to the product of the mass m and the resulting temperature increase ΔT:

$$c_p = \frac{Q}{m \cdot \Delta T} \tag{4.1}$$

where the subscript p indicates specific heat capacity at constant pressure (Schön, 2011).

The specific heat can be measured at constant pressure (c_p) or at constant volume (c_v). For the incompressible material the specific heats are equal to one another, $c(T) = c_p(T) = c_v(T)$. The $c(T)$ is a weak function of the temperature and for a wide temperature interval it can be approximated by a linear equation:

$$c(T) = c(T_i) + \beta(T - T_i) \tag{4.2}$$

where T_i is the initial temperature, and β is the coefficient. The thermal capacity is also defined as the amount of energy required to raise the temperature of a unit of the mass of a substance by 1° (Eppelbaum et al., 2014).

Thermal Diffusivity

Another physical property that influences the rate at which heat dissipates through the material is the thermal diffusivity α.

The thermal diffusivity represents a measure of a material's ability to respond to changes in its thermal environment and it is defined as

$$\alpha = \frac{\lambda}{\rho c} \tag{4.4}$$

where ρ is the density and c the specific heat (Pasquale et al., 2014).

Under transient conditions, this parameter determines how fast the temperature field of a solid changes with time; it controls the time-dependent temperature distribution. The coefficient of thermal diffusivity (α) is connected with specific heat capacity c_p, density ρ, and thermal conductivity λ:

$$\alpha_{ij} = \frac{\lambda_{ij}}{c_p \rho} \tag{4.5}$$

Thermal diffusivity is given in m^2s^{-1} (Schön, 2011).

Thermal Conductivity

Thermal conductivity, or the thermal conductivity coefficient, of a material represents the measure of a material's ability to transfer thermal energy (heat) by conduction. We may consider an infinite plane wall of a certain material with a thickness of one unit in length. The sides of the wall are maintained at constant temperatures and the temperature difference is equal to 1°C. Let us also assume that a sensor can measure the amount of heat per unit of the area of the wall per unit of time. In this case the amount of heat measured will be numerically equal to the thermal conductivity coefficient (λ) of the given material (Eppelbaum et al., 2014).

The basic law of thermal conduction is the Fourier's law which defines heat flow density q_i, the vector of heat flow rate (W/m^2), in isotropic solids as the product of the thermal conductivity tensor λ_{ij} and the temperature gradient vector $\partial T/\partial x_j$:

$$q_i = -\lambda_{ij} \cdot \frac{\partial T}{\partial x_j} \tag{4.3}$$

where ij refers to the directions (Schön, 2011). The negative sign is due to the fact that heat flows in the direction of the decreasing temperatures (Eppelbaum et al., 2014; Pasquale et al., 2014).

Since q is the amount of energy flowing through an unit area per unit time, the thermal conductivity λ is expressed in $Wm^{-1}K^{-1}$ (Pasquale et al., 2014).

Thermal conductivity can be measured in the laboratory on rock samples, i.e. cores or cuttings, or in-situ in boreholes or with marine heat flow probes. There are numerous steady state and transient techniques available for measuring thermal conductivity, the most prominent being the "divided bar" and the "needle probe" method (Clauser and Huenges, 1995).

In a steady-state thermal regime, i.e. when temperature does not vary with time, thermal conductivity expresses how fast heat is transported due to a spatial variation in temperature. Under transient heat conduction, thermal diffusivity describes the rate at which heat flows (Pasquale et al., 2014).

Looking for publications regarding thermal properties of rocks, mineralogy immediately assume a crucial role. Then, each lithology is different from the others because of its natural variation in mineral content. However, consulting the several extensive compilations that have been made for a large number of rocks classified according to rock name and origin, a great variability of thermal conductivity values (λ) within the same lithologies can be easily observed. Figure 4.1 highlight the variability of thermal conductivity existing within single lithologies. This spreading of values is due to the fact that several factors affect thermal conductivity of rocks.

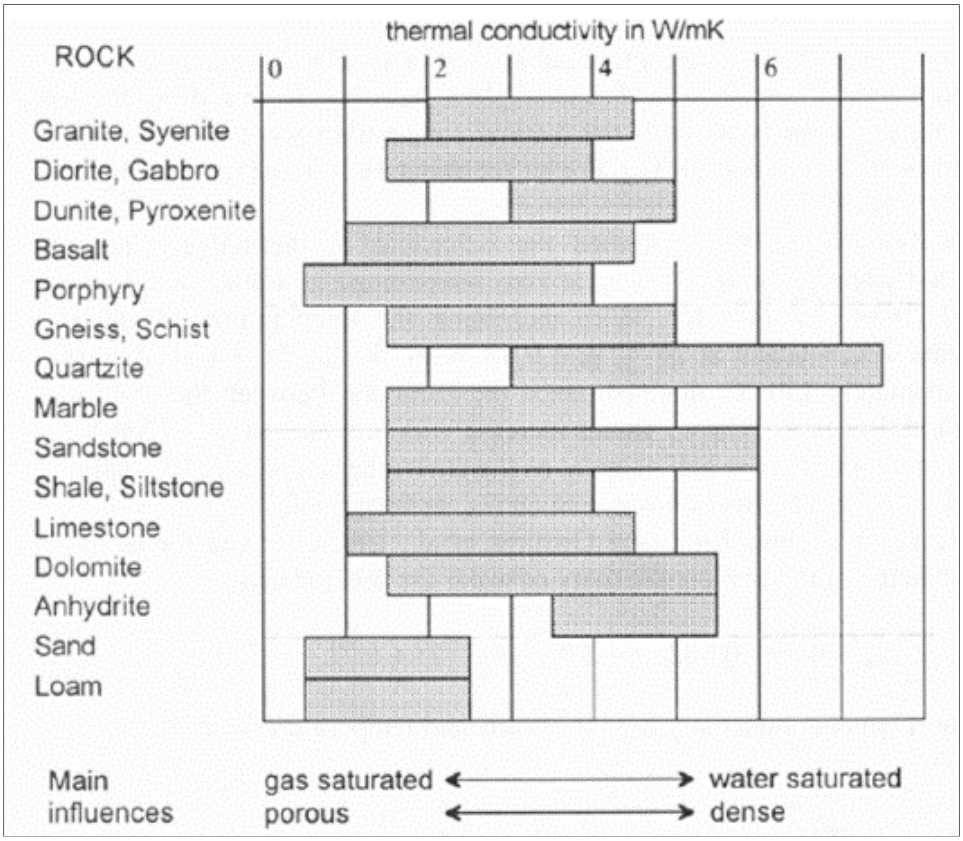

Figure 4.1 *Thermal conductivity variability for some rocks according to porosity and pore fluid.*

Apart from temperature and pressure, porosity, degree of saturation, pore fluid, dominant mineral phase, and anisotropy are controlling factors. Clauser and Huenges (1995) composed two ternary diagrams in which different types of rocks are related to those factors that have the most pronounced effect on their thermal conductivity (Figure 4.2). The position of a rock's name in the compositional triangle indicates in a qualitative way its thermal conductivity.

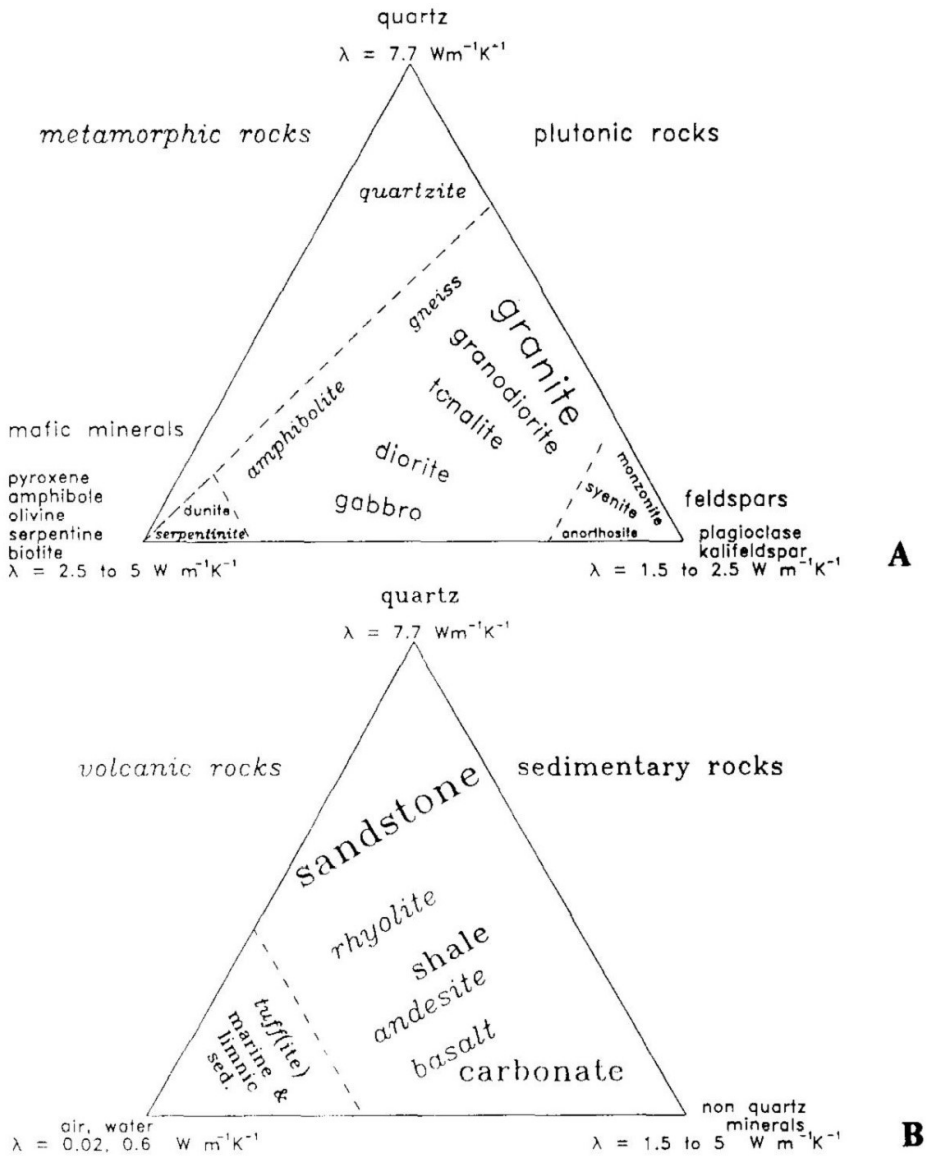

Figure 4.2 *Thermal conductivity of basic rock-forming minerals and compositional relationship with rocks. (a) metamorphic and plutonic rocks, (b) volcanic and sedimentary rocks.. For volcanic and sedimentary rocks the third "mineral" phase is air or water, due to the great importance of porosity for the thermal conductivity of these rocks. From Clauser & Huenges (1995).*

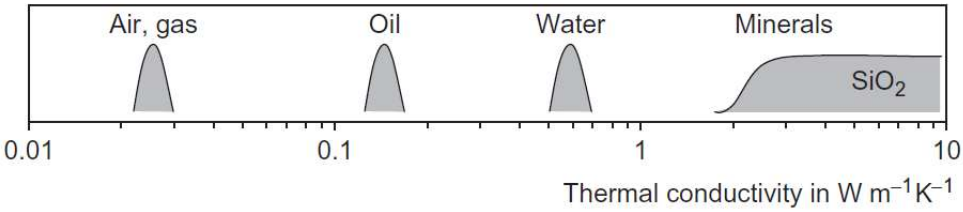

Figure 4.3 *Schematic picture of thermal conductivity distribution of fluids and rock-forming minerals (Schön, 2011).*

Among sedimentary rocks, only pore-free sediments show a relatively small variation, because they do not have the strong influence of porosity and pore fluid, but only some variation of chemical composition and impurities (Clauser and Huenges, 1995; Schön, 2011). In all other cases, porosity has a great influence because of the distinct difference between conductivity of matrix materials (minerals) and pore-filling material (Figure 4.3). Air and water, when dry and wet samples are measured respectively, have lower conductivity than minerals so a great quantity of pores causes a decrease in thermal conductivity.

4.1.1 Laboratory Test (C-Therm)

Two groups of methods used to measure thermal conductivity of rocks in laboratory are recognized: steady-state (or stationary) methods and transient methods. Both groups of measurements provide a temperature gradient and verify the thermal reaction of the material to this temperature change. In steady-state methods thermal conductivity is measured directly while in transient methods values of thermal diffusivity are generally measured and from these measurements thermal conductivities are calculated. Steady-state methods require long amount of time to achieve equilibrium conditions and require carefully prepared test specimens of specific geometries. Transient methods of measurements are usually much faster than steady-state methods (Gustafsson, 1991; Mathis, 2000; Somerton, 1992).

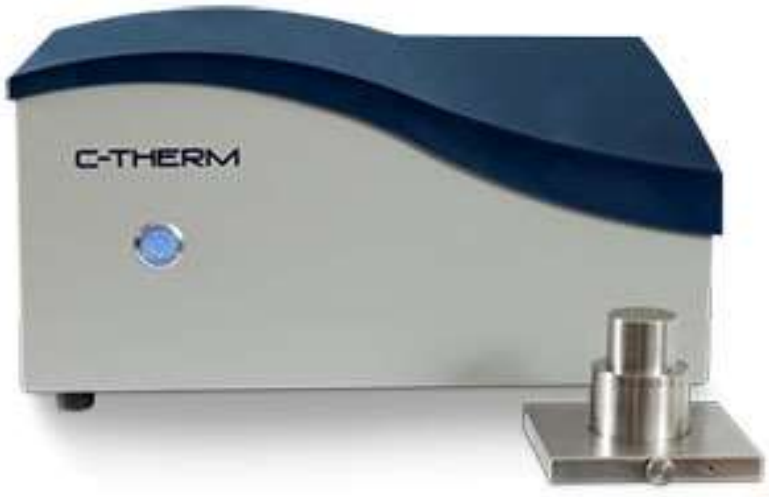

Figure 4.4 *TCi Thermal Conductivity Analyzer. The module for data processing and the one-sided, interfacial heat reflectance sensor.*

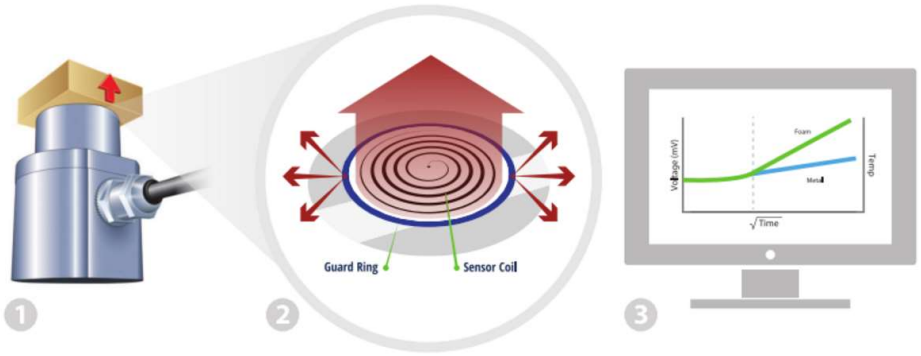

Figure 4.5 *Simplified scheme of how C-Therm TCi measures thermal conductivity. 1) a known current is applied to the sensor's element, providing a small amount of heat. 2) a guard ring surrounds the primary sensor coil. The applied current results in a rise in temperature at the interface sensor- sample, which induces a change in the voltage drop of the sensor element. 3) the rate of increase in the sensor voltage is used to determine the thermal properties of the sample.*

The thermal analyses conducted on dolomites and trachytes, both in the present and previous works, were performed with the C-Therm "TCi Thermal Conductivity Analyzer" (manufactured by C-Therm Technologies) which employs the *Modified Transient Plane Source* technique in characterizing the thermal conductivity and effusivity of materials (Figure 4.4). It employs a one-sided, interfacial heat reflectance sensor that applies a momentary constant heat source to the sample. The test methodology allows for much faster, easier thermal conductivity testing. It represents a significant innovation in thermal analysis in reducing testing time to seconds from hours. Typically, the measurements pulse is between 1 to 3 seconds. Thermal conductivity and effusivity are measured directly, providing a detailed overview of the heat transfer properties of the sample material (www.ctherm.com).

To understand how the C-Therm Analyzer works, an image illustrating a three points process is reported in Figure 4.5. Point 1: a known electrical impulse is applied to the sensor's spiral heating element, providing a small amount of heat. TCi thermal conductivity sensors are factory-calibrated and provided with reference material(s). The standard reference materials are tested via traditional ASTM methods for thermal conductivity measurement by external third-party certified labs. Point 2: a guard ring surrounds the primary sensor coil to support a one dimensional heat transfer into the sample. The applied current results in a rise in temperature at the interface between the sensor and the sample, which induces a change in the voltage drop of the sensor element. Point 3: the rate of increase in the sensor voltage is used to determine the thermal properties of the

sample. The voltage is factory-calibrated to temperature. The thermal conductivity is inversely proportional to the rate of increase in the temperature at the point of contact between the sensor and the sample. With the C-Therm TCi results are reported in real-time making thermal conductivity measurements fast and easy (www.ctherm.com).

The tested object must be flat in order to evaluate thermal properties. The TCi tests the properties of the material in contact with the sensor, so if the tested material or object is not flat, the air in the cracks or buckles will be tested too.

As the TCi employs a transient test methodology, it requires that the heat generated at the interface does not totally penetrate the tested material or object. It is suggested to be a minimum 2 mm thick for a 0.8 $second$ (factory default timing parameter) test for materials under 2 W/mK - but the minimum thickness depends on the properties of the material and the length of the test. It is possible to test thinner materials. Insulation material can be thinner than conductive materials. A Blotter Test can be performed to ensure the sample is sufficiently thick and a user can also stack thin samples such as films to produce a thicker cross section for testing as long as the material forms an intimate bond between layers.

4.1.2 In-Situ Measurements (GRT)

In some particular situations, thermal properties of a specific underground are requested. In these cases, in-situ measurements are necessary.

A real case is here reported. The new humanistic polo of the Padua University, with libraries, classrooms, offices and parks, will be settled in the former geriatric hospital (Fig. 4.6). The complex is spread over an area of 14.738 square meters on which the Italian company *Georicerche* installed about sixty thermal probes on a grid all over the site construction. This probe field will be in service of a geothermal plant for heating and cooling of buildings. Each probes are doubled-U probes; this means that there are two independent circuits, plus a pipe used for the concrete casting within the hole (Fig. 4.7b).

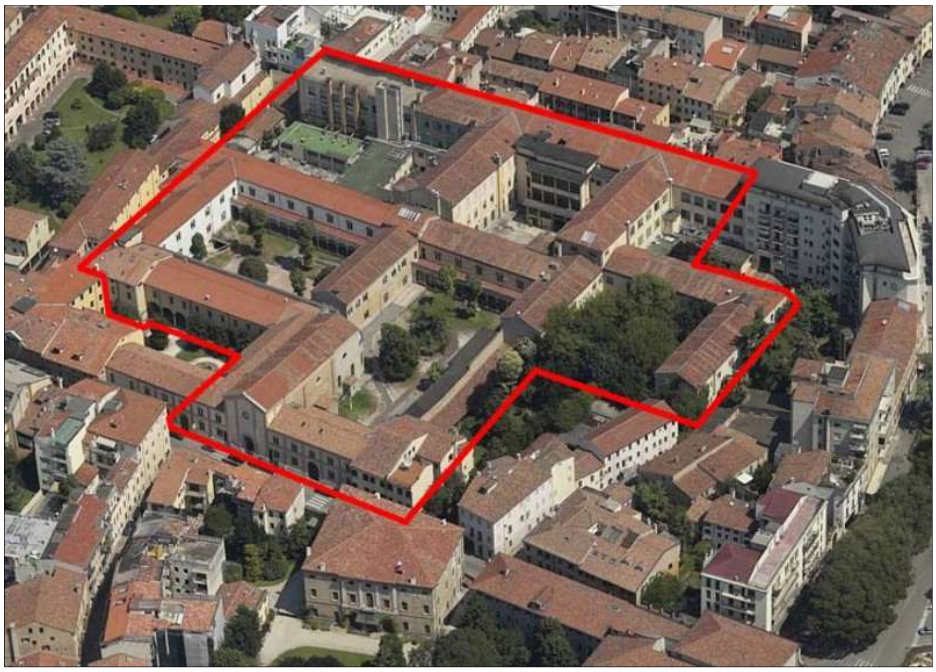

Figure 4.6 *Aerial view of the area of about 14738 square meters in which the new humanistic polo of the Padua University will occupy.*

Figure 4.7 *a) GEOgert 2.0 system for testing geothermal probes. b) focus on a geothermal probe consisting on two U-shaped independent circuits, plus a pipe used for the concrete casting within the hole.*

Geogert 2.0 is a system for testing Ground Source Heat Exchangers (GSHE) probes; it is made up of the machine, GEOsoft for the data processing and the web site (Fig. 4.7a).

It has been designed to perform all the tests required to try out the probes and to estimate the thermal characteristic of the ground by the probes:

(1) Pressure test;

(2) Flow test;

(3) Undisturbed ground temperature measures;

(4) Geothermal Response Test (GRT).

GEOgert 2.0 is made up of two modules: module 1 for flow test, pressure test and measure of the undisturbed ground temperature; module 2 for the execution of the GRT with electrical resistance.

Among the main output, Geosoft provides the step-by-step graphs of the thermal conductivity of the soil, the trend of the apparent thermal resistance of the probe, as well as the trend of the main test variables: inlet and outlet temperature, electric power, flow rate, etc.

The temperature of the subsoil at different depths is obtained in an indirect way by measuring the temperature of the water inside the probe.

There are two different procedures to measure the temperature: the opened loop and the closed loop. To perform the opened circuit procedure the water should have never flowed, so that it is already in thermal equilibrium with its surroundings when the test starts. The fluid flows from one end of the probe by connecting the other one to the water supply. The machine repeats the temperature measure in order to obtain in output both a weighted average temperature value and a trend function of depth.

The test is performed independently on the two circuits of the double-U probes with the automatic conversion and comparison of results. This innovative procedure minimizes the external thermal interference, allowing the user to interpolate the stratigraphy of the thermal probe.

On the other hand, in the closed loop procedure there is a pump that lets the water flowing until the temperature difference between inlet and outlet section is about zero. In this way, the water in the probe is in internal equilibrium with its surrounding. As results the user can measure the average temperature of the subsoil. Once the undisturbed ground temperature was measured, the machine was set for the ground response test. The test lasted more than 72 hours.

It is a design tool, if performed before the completion of the geothermal plant, but also an acceptance test to verify the quality of cementing, to be used random or in case of doubts on the specific probe. The test is performed by providing to the fluid, through an electrical resistance, a quantity of thermal energy known and constant for at least 72 hours. The conditions of energy dissipation in the ground define the temperature difference between the inlet and the outlet section, and then through the analysis of the behaviour of the temperatures over time the user can calculate the apparent thermal conductivity of the soil around of the probe and the thermal resistivity of the probe itself. To obtain the results the data acquired by the machine require a subsequent processing through GEOsoft 2.0 (www.geogert.com).

4.2 Physical Properties of Rocks

4.2.1 Introduction

The density and porosity of a rock are fundamental physical properties on which practically all other physical properties, such as seismic wave velocity, thermal conductivity, electric conductivity, are directly or indirectly related (Gong, 2005).

These properties are strictly related each other. As results, some methods could provide the measurements of both parameters, such the Helium Pycnometer method, the caliper and the scanner too.

Density

Density ρ is defined as the quotient of mass m and volume V of a material:

$$\rho = \frac{m}{V} \tag{4.6}$$

The SI unit for density is $kg\ m^{-3}$. For geological materials it is used $g\ cm^{-3}$.

Due to the heterogeneity of rocks, it is necessary to distinguish between different densities that are related to different rock components (Gong, 2005; Schön, 2011):

- ρ_b or bulk density (the mean density of the considered rock volume, including pores; for example, density of sandstone:
- ρ_i (density of any individual mineral rock component i; for example, density of quartz).
- ρ_{matrix} (mean density of the solid matrix material without pore fluid, also called grain density; for example, density of a carbonate matrix,).
- ρ_{fl} (the mean density of the pore or fracture fluid; for example, density of water ρ_w).

Bulk density corresponds to the ratio between mass and total volume of a rock:

$$\rho_b = m/V_{total} \tag{4.7}$$

where $V_{total} = V_{matrix} + V_{pores}$ supposing that the volume of rock consists of matrix and pore (for dry rock sample mass of air in the pore can be neglected) (Gong, 2005). Bulk density of a composite material (rock) consisting of n components is:

$$\rho = \sum_{i=1}^{n} \rho_i \cdot V_i \tag{4.8}$$

where ρ_i is the density and V_i is the volume fraction of component i (Schön, 2011).

Matrix density considers only the mass in the matrix volume, and the void volume of the pores inside the rock is excluded. Therefore, matrix density is defined as the mass in the matrix volume:

$$\rho_{matrix} = m/V_{matrix} \tag{4.9}$$

Porosity

Porosity is a fundamental volumetric rock property: it describes the potential storage volume of fluids (i.e., water, gas, oil) and influences most physical rock properties (e.g., elastic wave velocity, electrical resistivity, and density).

Porosity is defined as the summarized volume of all pores, fractures, cracks, etc., or generalized all fluid (e.g., gas, water, hydrocarbons) or "nonsolid" containing parts of a sample related to the total volume of the sample:

$$\phi = \frac{V_{pores}}{V_{total}} = \frac{V_{total} - V_{matrix}}{V_{total}} = 1 - \frac{V_{matrix}}{V_{total}} \tag{4.10}$$

From the bulk density ρ_b and matrix density ρ_{matrix}, one can obtain the porosity by using Equation (4.7) and (4.9) in Equation (4.10),

$$\phi = 1 - \rho_b/\rho_{matrix} \tag{4.11}$$

Porosity is given as a volume fraction (dimensionless) or as percentage.

The definition above describes the "total porosity". If the rock contains a part of non-connected or separated pores (vugs, moldic pores, etc.), then this part does not contribute to any fluid transport within the rock and is "non-effective". Thus, effective or interconnected porosity is the ratio of the connected pore volume and the total rock volume (Schön, 2011).

Porosity can be determined directly by various laboratory techniques and indirectly by logging methods. Several methods can be employed to directly measure rock porosity: (1) saturation or imbibition, (2) buoyancy, (3) gas expansion (He porosimetry), (4) gas absorption (BET) and (5) mercury intrusion porosimetry (Anovitz and Cole, 2015).

Bulk density and open porosity of dolomite samples (by Alessandra De Lullo) and trachyte samples (by Stefano Buggiarin) have been determined through a saturation method according to the UNI EN 1936 standards. It is a standardized procedure in which the Archimedes' principle is applied; it states that "a body immersed in a fluid (liquid or gas) is buoyed up by a force equal to the weight of the fluid that occupies the volume displaced".

From each rock sample it has been provided three cubes of 3 cm side when possible, or at least three parallelepipeds of similar size. The first step in the laboratory was to dry the rock specimens for 24 hours in an oven at a temperature of $70 \pm 5°C$; once removed from the oven cubes were placed inside a dryer at a constant room temperature of $21°C$. After this treatment, in a second step, the dry weight (md) of the rocks was measured with a Mettler PM400 precision balance. For the complete description of the method see (Buggiarin, 2014) and (De Lullo, 2016).

All of the following parameters have to be measured:

- Weight of dry sample "md" (g)
- Weight of saturated sample "ms" (g)
- Weight of the wire in the water "C" (g)
- Weight of saturated sample + weight of the wire in water "D" (g)
- Weight of saturated sample in water "mh =D-C" (g)
- Density of water at the temperature of measurement (g cm^{-3}), as the density of water depends on temperature.

From this data bulk density and open porosity can be computed through the following equations:

$$\rho_b = \frac{md}{ms - mh} \cdot \rho rh \quad \left[\frac{g}{cm^3}\right] \tag{4.12}$$

$$\phi = \frac{ms - md}{ms - mh} \cdot 100 \quad [\%] \tag{4.13}$$

where ρ_b is the bulk density in (g cm^{-3}), md is the weight of dried sample in air (g), ms is the weight of saturated sample in air (g), mh is the weight of saturated sample immersed in water (g) and ϕ is the open porosity.

For our purposes, porosity of dolomite and trachyte samples have been analysed under two different aspects: the porosity as percentage (volume and area fractions) and porosity as size distribution of pores. Therefore, it was prepared:

- micronized powder. The micronization was conducted as described in subsection 4.3.1 with a McCrone Micronizing Mill;
- coarse material with grains size > $1mm$;
- 3 cubes of different dimensions according to material availability;
- polished surfaces (2 for each dolomite sample and 1 for each trachyte samples) for the image acquisition through scanner.

Bulk density was measured by geometric means measuring the cubes with a caliper (subsection 4.2.3) while granulate and matrix densities were determined through the pycnometer on granulates and powders (subsection 4.2.2). From these results, the porosity was computed. Open porosity values were compared with that of Buggiarin (for the trachytes) and De Lullo (for the dolomites).

Area fractions of porosity were obtained through image analysis of the polished surfaces. The scanning operation and the elaboration of the acquired images is described in subsection 4.2.4. Otherwise, the acquisition procedure of elemental maps and their processing that allow to isolate pores and to better visualize their distribution within the rock matrix on a microscale are described in section 4.4.

4.2.2 Helium Pycnometer

Once powders and granulate were prepared, they were divided into test tubes and a code was assigned to each of them: for dolomites, numbers from 1 to 3 are micronized powder, numbers from 4 to 7 are granulates (see Figure 4.9c); for trachytes there are the same numbers but there are only three granulates. A, B, C are the letters for cubes.

For the porosity measurements a Micromeritics AccuPyc 1330 Pycnometer was used (Figure 4.8). It is an easy-to-use, fully-automatic gas displacement pycnometer. Gas expansion methods employing Boyle's law, most notably helium (He) porosimetry, are considered among the most accurate techniques for measuring effective porosity in low permeable rocks as well as lithologies such as sandstone.

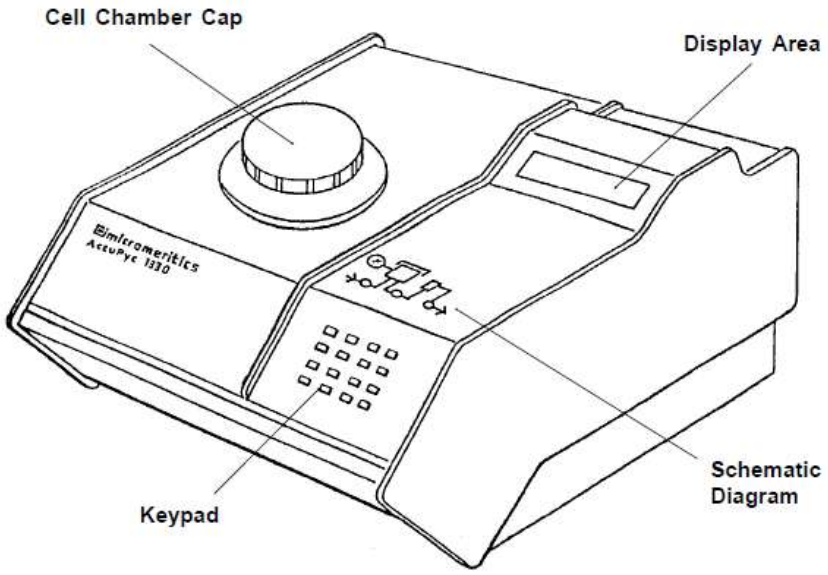

Figure 4.8 *AccuPyc 1330 Pycnometer (from AccuPyc Operator's Manual). The schematic diagram, which is included above the keypad, indicates system status. The three indicators show the current state of the fill, expansion, and vent valves.*

The pycnometer uses helium (99.995% pure or better) to provide rapid, accurate analyses. Helium has advantages over other gases because (Anovitz and Cole, 2015):

- its small molecules rapidly penetrate small pores;
- - it is inert and does not adsorb on rock surfaces as H_2O or CO_2 in air may do;
- - helium can be considered an ideal gas (i.e., $z = 1.0$) for pressures and temperatures usually employed in the test;
- - helium has a high diffusivity and therefore affords a useful means for determining porosity of low permeability rock.

A porosity analysis with AccuPyc is characterized by three phases: the instrument setting, the calibration, and then the data acquisition.

Setup Parameters

The set-up function enables the user to enter parameters to be used for analysis, calibration, reporting, and data transmission. The user can modify his own analyses by entering the following parameters: number of purges, purge fill pressure, number of runs, run fill pressure, equilibrium rate, and run precision. By modifying these parameters, the user retains control over the two main sections of the analysis: purge and run.

A purge is used strictly for sample clean up and air and moisture removal from the chamber's inside. It is accomplished by closing off the pycnometer block and filling the cell chamber to the designated purge fill pressure. The chambers are then vented to atmosphere, resulting in elimination of water vapor or other contaminants. A run is used for collecting the precise, accurate data used in report calculations.

In Table 4.1 the default *analysis parameters* and *report options* are listed. The default "volume" in *analysis display mode* was left for the calibration phase only, because the volume of the sphere (the standard) was the only parameter we were interest in. Prior to begin the true analysis, the *analysis display mode* was switched from "volume" to "density": in this way both volume and density results of samples were printed.

Table 4.1 *AccuPyc Pycnometer parameters set for the analysis.*

Analysis Parameters		**Report options**	
Number of purges	3	Request sample ID	no
Purge fill pressure	19.5 psig	Analysis display mode	volume
Number of runs	3	Report destination	display
Run fill pressure	19.5 psig	Transmission format	single column
Equilibration rate	0.005 psig/min		
Run precision	no		
Percent full scale	0.05		

Calibration

Calibration is used to determine the size of the cell and expansion chambers within the instrument. After calibration, the cell and expansion chamber volumes are automatically stored in the set-up parameters.

It is very important to check or calibrate the pycnometer anytime you restart it. When you are the first user in the morning or when another user has utilized the machinery before you, the calibration must be done because the conditions could have been altered and the pycnometer is strongly affected by local conditions. Therefore, when you change the sample holder, the calibration is needed because the volume of the cell chamber and expansion chamber have to be re-determined.

The calibration is subdivided into 2 steps:

- An empty cup (the smaller one if the user wants to measure the powders, or the biggest one for the granulates) has to be placed, the cell chamber cap replaced, then the calibration procedure begins pressing the right botton;
- When the first phase ends, the pycnometer beeps three times and “Insert cal std” compares on the display, the calibration standard has to be placed in the cup in the cell and the cell chamber cap replaced.

The standards samples are available (Figure 4.9a). The small standard sphere has a volume of 0.718492 cc and has to be used with the small chamber of 1 cc; the volume of the big sphere is 2.421100 cc that has to be used with the chamber of 3.5 cc.

Once the calibration ends, the reported volume of the standard is compared with the declared values. Errors to three decimal places are accepted.

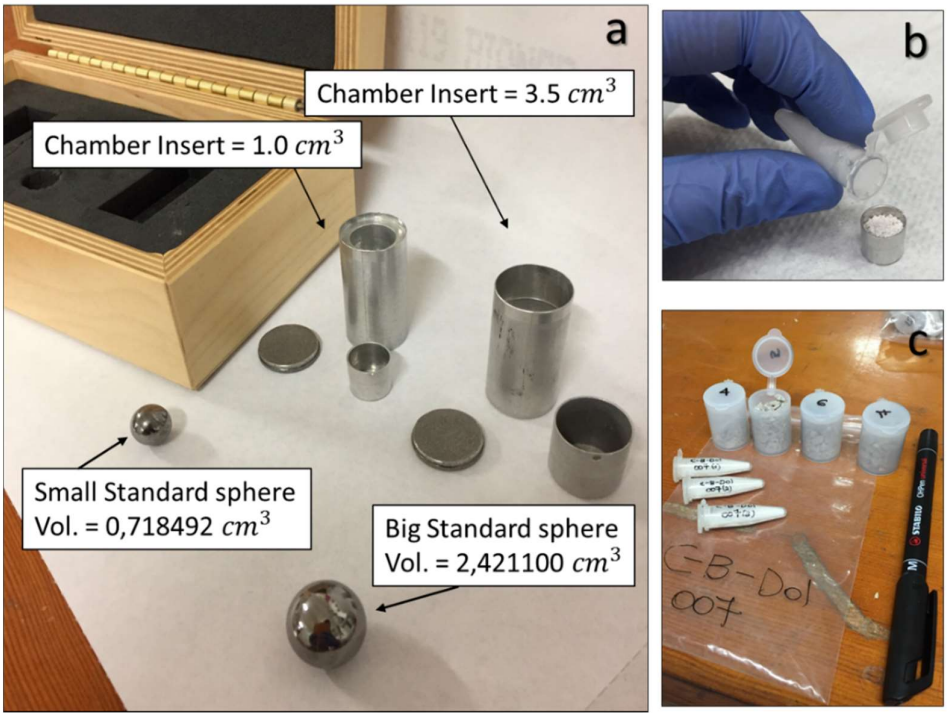

Figure 4.9 *a) Chambers where to insert sample. The small chamber is calibrated through the small standard sphere; the big chamber through the big standard sphere. b) Small chamber while inserting the powder. c) C-B-Dol_007 sample prepared for the pycnometer analysis: 3 specimens of powder and 4 of granulate.*

Analysis

Two chambers where to put the rock sample are available (Figure 4.9a): the small one (used for powders) has a volume of 1 cm^3 while the big one (used for granulates) has a volume of 3.5 cm^3.

Prior to each measurement each specimen in the chamber (Figure 4.9b) was weighed on a precision balance because the mass is an important value that the pycnometer uses to calculate the density from the volume it measures. Reading the operator's manual an important point to keep in mind is that each step should be conducted to avoid exposure of the dried sample to atmospheric moisture. This means weighing as rapidly as possible and installing in the instrument without unnecessary delay. Unfortunately a precision balance is not available in the laboratory where the pycnometer is installed so the user has to move in a different laboratory; as consequence this operation is time consuming and it involves a long exposure of the sample to air.

A gas pycnometer like AccuPyc 1330 determines volume, and then density, by detecting the pressure change in helium resulting from displacement of gas by a solid object in the calibrated volume. Once an analysis is initiated, data are collected, calculations performed, and results displayed without further operator intervention. In fact, the density values are directly computed by the pycnometer by means the mass value that is inserted at the beginning of the measurement.

4.2.3 Caliper

The bulk density ρ_b of a sample in the form of a cube can be determined by geometric means using a digital caliper, knowing the weight of the dry cube (Figure 4.10).

As stated above, 3 cubes for each sample were prepared. The side dimensions are in a range from 12.565 mm to 28.5342 mm for the dolomites and from 19.5033 mm to 25.3108 mm for the Euganean Hills trachytes.

The cubes have been obtained with a Struers Labotom – 3, a compact table-top model for abrasive wet cutting; the roughness of some imperfect faces was deleted through Struers LaboPol – 5.

The volume of the cubes was calculated first measuring all 12 sides and raising the mean value at the third power. For the mass measurement it was important to have sample perfectly dry so the cubes were left in an oven until the mass was constant. The bulk (geometric) density was then computed with the equation (4.6): $\rho = m/V$.

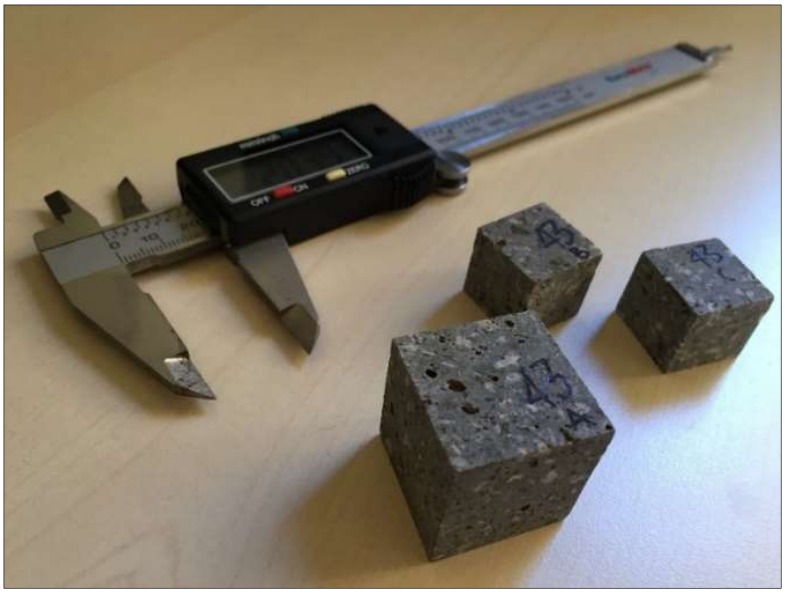

Figure 4.10 *Example of how cubes of the samples were prepared for the geometric density calculation. Above the digital caliper used for cubes measures.*

4.2.4 Scanner

Regarding the dolomite samples, De Lullo (2016) prepared one cube of dimensions range between 6.5 to 10 cm per side and other three smaller cubes of about 3 cm side for each sample. Unfortunately, this cubes were not available because they were sent to Germany laboratories where other thermal analyses have been conducted. Anyway, among the chunks of rock remained in the Padua department there were some of the faces corresponding to those of the cubes. Two were the advantages: cutting operations were not necessary and the image analysis were made on surfaces with the same or very similar characteristics of that De Lullo made thermal measurements on.

It was decided to select two different surfaces to be scanned for each sample in order to have more data to be compared. After an accurate observation of the hand-samples, the surfaces were selected. The criterion of selection was driven by two important aspects: the areas had to be not too small, to guarantee the

representability, and not too big, because the images would have been very heavy data amount and so very difficult to be processed. Then, the surfaces were compared with the faces of the cubes on which De Lullo made the thermal measurements to be sure that the physical characteristics were similar. E and F are the letters assigned to the dolomite samples surfaces.

For the Euganean Hills rock samples, only one surface per sample was selected; big pieces of rocks were available so it was simple to cut a slice. No letters was assigned so the images reports the name of the sample only.

In order to remove all the major asperities from the surfaces, the samples were put on a water lubricated *Struers Labopol-5* lapping machine equipped with a silicon carbide abrasive paper. *LaboPol-5* has a variable rotational speed of between 50 – 500 rpm controlled by an electronic servo system that keeps the selected speed constant, independent of the load. Then the samples were polished with a series of progressively finer aluminium oxide abrasives (no. 500, 800, 1200) through a Gemmarum Lapidator *Lapidello 400* polishing machine, until smooth reflective surfaces were obtained. *Lapidello 400* is a machine suitable for all those operation of lapping and polishing of the hard stone in which flat surfaces of large dimensions are required.

The following step was to fill the voids on the surface to be analysed with a powder of synthetic eskolaite (Cr_2O_3) that is characterized by a green colour (Fig. 4.12b); in this way the pore network would have been easily distinguishable from the rock matrix on the acquired image. Prior to the aspersion on the rock surfaces, the powder was finely micronized on a McCrone Micronizing Mill. It was important to carefully clean the surfaces in order to remove the powder in excess; a small agglomerate of powder grains left on a part of the sample without voids would have been seen as one or more voids affecting the results.

In Figure 4.12a-b you can see how the surface of sample C-B-Dol_007 appeared before and after the green powder treatment. The surface ready to be scanned had big pores and fractures visibly filled with chromium oxide and other micro-porous areas in which the former colour of the rock was altered towards more green tones.

The surfaces treated with chromium oxide were then scanned in 24-bit colour through a high-end Epson V750 PRO flatbed scanner at a 3600x3600dpi ($8 \times 8\mu m$) optical resolution (Figure 4.12d).

Since rock surfaces were quite large, the acquisition of each image took some time and the files were heavy.

The image analysis was performed on scanned images through ENVI 4.7 and ImageJ software. ENVI allows you to make the image segmentation while ImageJ the particle (voids in this case) analysis.

The images were characterized by two-components: the rock matrix and the pores. This simplification allows a simple explanation of the method. After a series of preliminary operations on the RGB images the segmentation of the porosity was performed: pores were separates from the rest of the image and this allowed to quantify the porosity percentage and then to analyse the pores. The first step was the creation of a class called *voids* and to do this a ROI Tool was used. A ROI (Region of Interest) is a manually created class in which all the pixels corresponding to voids are grouped. To do this, the software has to be educated through so called "training pixels": once a ROI is created, the pixels that represent the voids (with polygons) have to be manually selected. When the defined class ("voids class" in this case) is described by an adequate number of training pixels, the classification can be performed applying a supervised maximum likelihood classification. The resulting classified image is characterized by red-coloured voids areas within a black background corresponding to the rock matrix (Figure 4.11 b).

After the segmentation process, a binary images is created; a black-and-white image (pores in black within a white groundmass) allowed to isolate the voids from the rock matrix, understand how they are distributed and also to make a series of pores measurements such as area, min and max Feret, ecc.

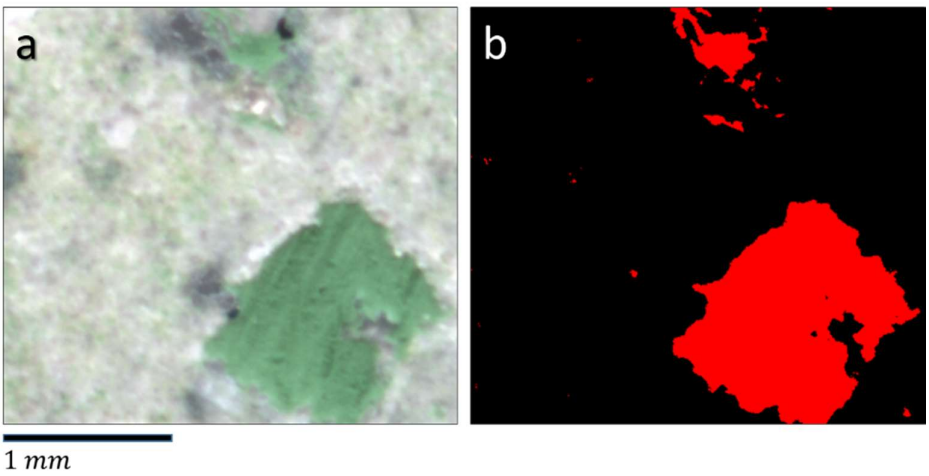

Figure 4.11 *Particulars on sample 1 from Euganean Hills porosity. Zoom 1x on real colours image (a) and on segmented image (b)*

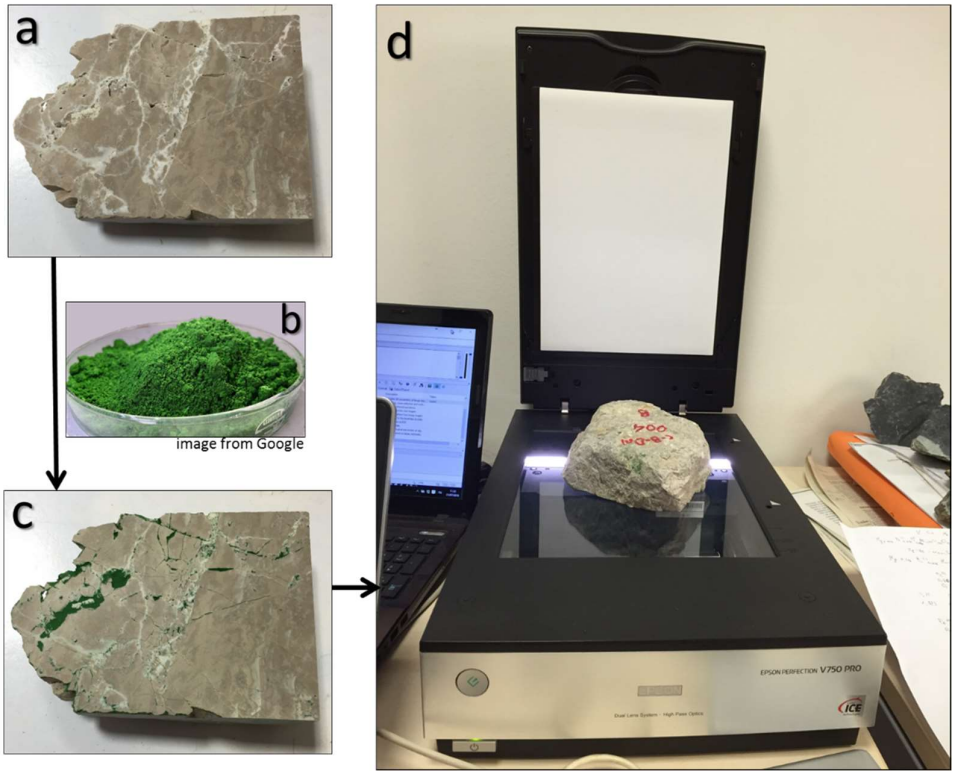

Figure 4.12 *Sample C-B-Dol_007 F a) before the aspersion of b) Cr_2O_3 powder on the surface and c) after the treatment. d) Epson V750 PRO flatbed scanner during the acquisition of the C-B-Dol_004F sample image.*

4.3 Mineralogical content

The mineralogical content of rocks is one of the most important factor influencing its thermal behaviour. Thus, it is necessary to know which phases are present in a rock, in which quantity, and how they are distributed within the rock matrix.

Spatial distribution information are highlighted by X-ray maps (see section 4.4), while the quantitative analysis is performed with other analytical techniques. In section 4.3.1 X-ray diffraction technique with the Rietveld refinement are briefly described. Section 4.3.2 provides the basic information about X-ray fluorescence.

4.3.1 X-Ray Diffraction

X-ray diffraction (XRD) is an analytical technique based on the x-ray scattering produced when passing through the matter. The scattering phenomenon occurs when X-ray photons interacts with the electrons present in the studying material. Electrons behave as diffusion centres for X radiation of

the same wavelength (coherent scattering) or different wavelength (incoherent scattering) of incident radiation. Diffraction is related to the coherent part of the scattering phenomenon: a crystalline solid covered by an X-ray beam produces diffracted X-rays along those directions where all the waves diffused by atoms in the crystal lattice are in phase concordance (constructing interference). To obtain a diffracted beam, certain geometric conditions have to be satisfied and such conditions are well described by Bragg's law:

$$2d_{hkl}sin\vartheta = n\lambda \quad (4.14)$$

where $d_{hkl}$is the interplanar distance between a family of hkl planes, ϑ is the angle between the direction of incident X-ray beam and the lattice planes hkl, λ is the incident radiation wavelength and n is an integer number.

X-ray diffraction can be performed on both single crystals and powders. Obviously, the present work needed the analysis of lithologies, not of single phases, so the powder X-ray diffraction was the chosen technique.

Nowadays the applications of Powder Diffraction include, besides the more traditional uses for phase identification work:

- the *ab initio* crystal structure determination;
- - the Rietveld crystal structure refinement;
- - the accurate phase quantitative analysis (QPA) by line intensity or the Rietveld methods;
- - the quantitative determination of microstructural properties such as lattice strain, domain size and disorder;
- - the kinetic and structural analyses of materials and reaction processes *in situ* at non ambient conditions also performed in real time, etc.

The choice of instrument components as well as of data collection strategy should be driven by the specific goal (e.g. phase identification, quantitative phase analysis, structure determination, structure refinement, microstructural analysis, time-resolved analysis, etc.). Furthermore, the choice of components and strategy is typically a trade-off between, at least, one of the following factors: sample features, data collection duration, required resolution, costs (purchase, maintenance, accessibility, etc.), and other constrains (e.g. non-ambient environments, etc.). The quality of collected data (hence the reliability of final results) largely depends on (Cruciani, 2006):

- - brilliance and quality (i.e. less divergence) of the primary beam;

- - choice of the optics;
- - quantity and shape of the sample under the beam;
- - type and efficiency of detector;
- - scan strategy (i.e. the choice of the angular range, step-size and counting times).

The instrumental set-up used for our analysis is reported in Table 4.2. The instrument is a PanAnalytical X'Pert Pro; it was insert a Co anode.

Table 4.2 *Instrumental parameter used for XRD acquisitions*

Instrument	Panalytical X'Pert Pro
	(Bragg Brentano geometry, theta-theta)
Tube type and settings	Long Fine Focus tube with Co anode, 40kV e 40mA
Detector	X'Celerator
Sample support	Circolar sample holder (32 mm internal diameter)
Sample stage	Spinner
Optical elements	Divergent slit 1/4°
	Antiscatter slit 1/2°
	Soller slit 0.04 rad
	Bragg Brentano HD
Acquisition range and rate	3-85º 2theta
	Virtual step 0,017º 2theta
	100s x step

As regard the sample preparation, the powder was finely micronized on a McCrone Micronizing Mill. The grinding vessel (Figure 4.13) consisting of a $125\,ml$ capacity polypropylene jar fitted with a screw capped gasketless polyethylene closure. The jar is filled with an ordered array of 48 identical cylindrical grinding elements in zirconium oxide (they are also available in agata or corundum). These cylindrical elements grind the samples gently via friction. The grinding time for optimum micronization is between 3 and $30\,minutes$. The dry sample volume is $2.5\,ml$ to which $10\,ml$ of water had to be added obtaining a moisture (Figure 4.13 c). There are several advantages to use this kind of method: first, crystal lattice is almost entirely preserved during grinding

operation (a premise for meaningful X-ray diffraction), secondly very narrow and reproducible particle size distribution is obtained, there is minimal cross contamination, it is a compact, bench-top sized model, and so on.

The grinding operation is a delicate step because the crystallite size of a polycrystalline sample should be the best controlled as possible (i.e. in the 1-3 μm range, < 10 μm) (Cruciani, 2006). An ideal polycrystalline sample is the one consisting of i) a very large number (ideally, infinite) of crystallites, ii) with the same number of crystallites in all possible orientation (random orientation), and iii) with a controlled grain size (usually in the 1-10 μm range). This are the fundamental requirements of a crystalline sample suited for powder diffraction. Every significant deviations from one of these requirements would introduce uncertainties in the final results.

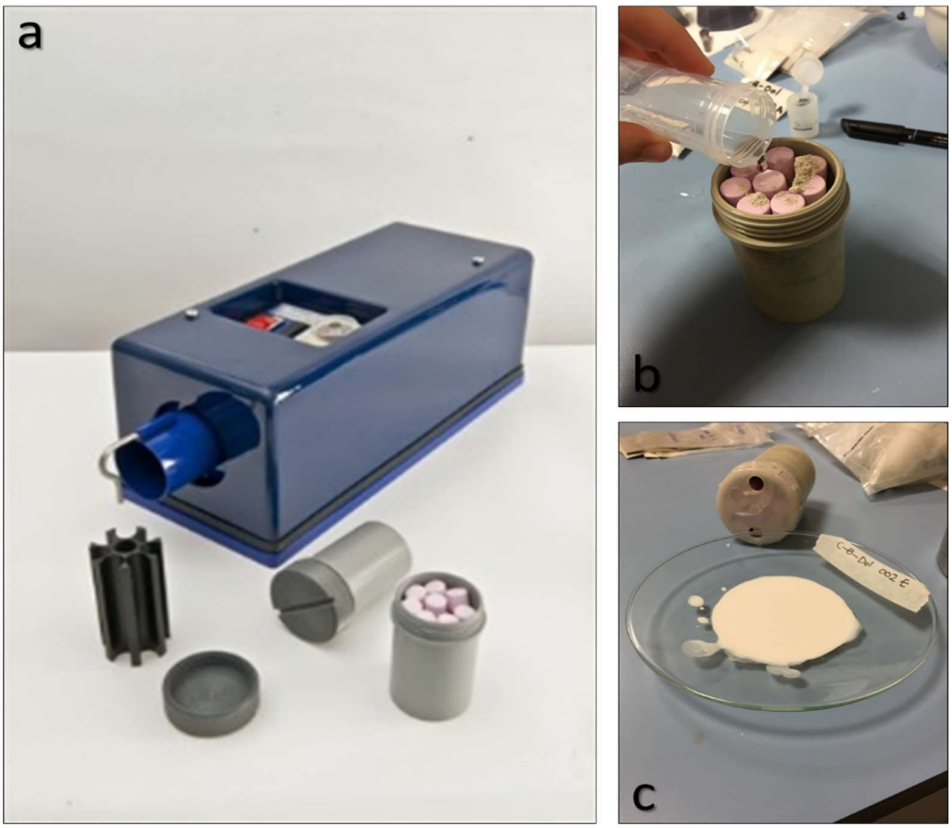

Figure 4.13 *a) McCrone Micronizing Mill, the grinding vessels consisting in a jar and 48 zirconium oxide grinding elements; the spacer. b) Once the powder is within the jar, 10ml of demineralized water is poured into the vessel. c) The mixture sample+water after 5 minutes of grinding.*

The very first step for a correct interpretation of a powder pattern is the phase identification occurring in a sample (qualitative analysis). Each crystalline phase shows a peculiar combination of position and intensity of diffraction peaks. In this way, every diffractogram of crystalline compounds is a sort of "fingerprint" for the compounds, which allow its identification.

The identification process consists firstly in a database search (PDF – Powder Diffraction File) that collects about 300.000 files of inorganic and organic crystalline phases. PDF database is maintained and updated by the International Centre for Diffraction Data (ICDD). PD Files report information related to the crystalline compound, references and list of d_{hkl} interplanar distances with relative intensities and characteristic Miller indices of each phase.

The correct phase identification procedure applied to a polyphaser sample assume different difficult degrees depending on the sample preparation, data collection strategy and the complexity of the phase blend.

The diffraction patterns acquired during this study were all qualitative interpreted with X'PertHighScore Plus 3.0 software by PANalytical. The mineral profiles of the compounds were reconstructed by comparing the reflection positions of the detected diffraction patterns with entries of ICDD (International Center for Diffraction Data) and ICSD (Inorganic Crystal Structure Database) databases.

One of the possible methods to determine the relative quantity of each phase in a blend is the Rietveld method. The basic of the Rietveld method lays on the complete exploitation of the whole powder profile without extracting the integrated intensities, all the structure and instrumental parameters are refined during the fitting procedure between the calculated and measured data. The refinement procedure implements the least square regression and it requires a reasonable scheme of starting values that approximate the real datum. Such parameters include:

- A function that describe the peak shape
- A function that describe the instrumental effects (on the shape, position and intensity of diffracted peaks)
- Structural parameters as cell dimension, space group and unit cell atomic coordinates.

The reliability of the Rietveld method is strictly connected to the quality of powder diffractograms (a well-prepared polycrystalline sample, high counting statistics and limited instrumental problems).

Structural refinements of the compounds were performed through full-profile fitting according to Rietveld method, using DIFFRACplus TOPAS software by Bruker AXS.

4.3.2 X-Ray Fluorescence

X-ray fluorescence spectrometry (XRF) is currently the most widely used analytical technique in the determination of the major and trace element chemistry of rock samples. The main limitation is that elements lighter than Na (atomic number =11) cannot be analysed by XRF (Rollinson, 1993).

X-ray fluorescence spectrometry is based upon the excitation of a sample by X-rays. A primary X-ray beam excites secondary X-ray (X-ray fluorescence) which have wavelength characteristic of the elements present in the sample. the intensity of the secondary X-ray is used to determine the concentrations of the elements present by reference to calibration standards, with appropriate corrections being made for instrumental errors and the effects the effects the composition of the sample has on its X-ray emission intensities (Rollinson, 1993).

The samples to be examined were grinded to a fine powder and micronized powders were used when available (the micronized powder analysed in XRF can be regained for other measures if no standards are mixed). 2 g are requested for a X-ray fluorescence analysis. Then it is the operator who proceeds with the analysis delivering the results in a Excel format table.

4.4 Texture

The texture of a rock represents the geometric complexity of its constituents, i.e., crystals, grains, glass and pores, as defined by their size, shape, position, orientation, and mutual spatial relationships. The description and quantification of texture is a key topic in petrology but textural characteristics are also studied in a number of related disciplines (Germinario et al., 2016).

There are different way to gain textural information of rocks; in section 4.4.1 the micro-XRF technique is introduced. Section 4.4.2 deals with the elaboration of elemental maps for textural and mineralogical quantitative analysis.

4.4.1 Micro X-Ray Fluorescence

Micro X-ray Florescence (μ-XRF) works on the same principles as standard XRF (see section 4.3.2), but high-intensity, finely collimated X-Ray beams are used (Haschke, 2012). It is a cheap analytical method for the determination of the chemical composition of many types of materials. It is non-destructive, requires no, or very little, sample preparation and therefore may be suitable for many studies, also in the geological field (Vaggelli and Cossio, 2012).

The measurements were performed in Torino (Dipartimento di Scienze della Terra) by means of the commercial μ-XRF Eagle III, an elemental analyser which combines an optical microscope to an ED-XRF spectrometer.

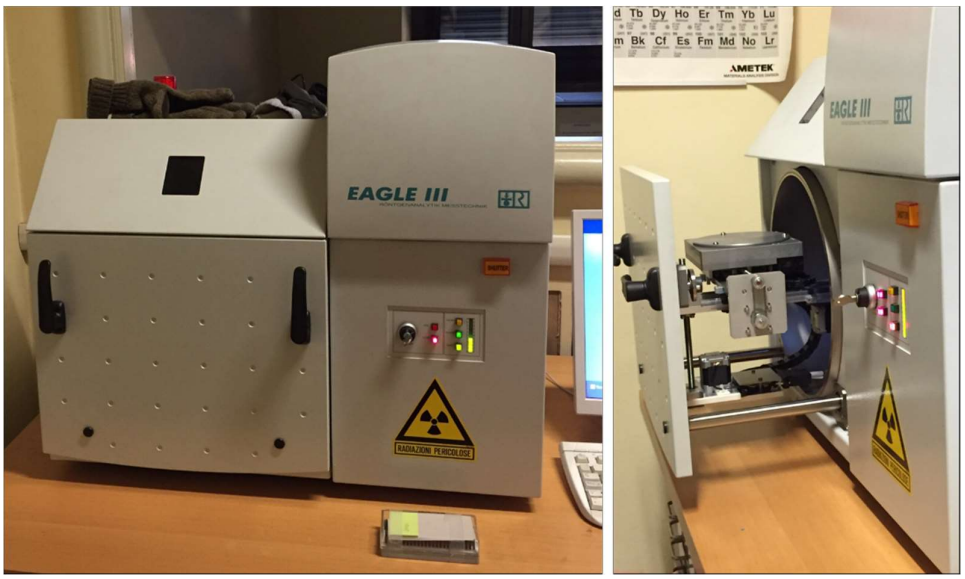

Figure 4.14 *Eagle III micro XRF. The unit on the left; the radiation-safe sample chamber and the motorized stage on the right.*

The Eagle III Micro XRF unit (Figure 4.14) is similar to a traditional XRF unit, with the primary difference being that the X-rays beams are focused onto the sample surface by a polycapillary optic into a spot nominally 50 μm in size (spot size ranging from 30 μm to 300 μm at various steps). The small, focused spot allows users to do X-ray imaging and microanalysis of a wide variety of samples where surface composition is of interest. There are also two cameras (magnification 10x and 100x) for sampling site viewing.

The micro-XRF technique requires little or no sample preparation for most materials (solids. liquids, powders, films and coatings, polymers…). 30 μm thin sections were used in the present work but rock tiles can also be analysed (in 2016 Germinario used $7 \times 7 \times 1\ cm$ tiles).

Unlike electron beam instruments, the large, radiation-safe sample chamber allows analysis either at atmospheric pressure or in vacuum (*ca.* 0.5 mbar). A typical micro-XRF instrument includes a high precision motorized sample stage, which allows the sample to be very accurately positioned beneath the X-Ray beam.

Equipped with an EDAX EDS system, the system has detection limits well below 100 ppm for most elements, and below 50 ppm for transition metals such as iron, copper and zinc. Elements lighter than aluminum (Al Kalpha = 1.487 keV) are heavily absorbed by the 25 μm thick beryllium window in front of the detector (Si(Li) semiconductor detector; LN_2 cooled), so the analysis of light elements is not possible. The system uses a 50 W rhodium tube for primary excitation: the X-Ray tube operated at 40 keV of accelerating voltage and maximum current of 1 mA). A time constant of 2.5 μs and a dwell time of 200 ms were chosen.

The μ-XRF is controlled and operated by the EDAX Vision 32, a software for instrument control and data analysis, which allows performance of automated spectral acquisition and quantification using single spot acquisition, profiles or mapping (Vaggelli and Cossio, 2012).

Micro X-ray Florescence enable to extract qualitative, quantitative, and spatial distribution information from samples.

ED-XRF spectrometer is ideally suited for very fast qualitative elemental analysis. Typically all elements from sodium through uranium can be detected simultaneously, with good quality spectra obtained in seconds/minutes. Band assignment for an XRF spectrum is usually easy, since each element peak occurs

at a known fixed position - however, overlapping bands can cause confusion, but modern software will take this into account for peak labelling. Similarly, certain artefact peaks may be present in the spectrum, including Rayleigh and Compton scattered characteristic lines from the X-Ray generator, peaks caused by X-Ray diffraction, and sum/escape peaks. Knowledge of these is necessary to avoid incorrect interpretation of results.

Regarding quantitative and size distribution information acquisition, elemental maps are necessary. Then, once the measurement conditions have been chosen, the motorized stage (it is a precision, computer-controlled $x - y - z$ sample stage with precise stepper motors that controls its movements) will move to each position in turn, acquiring a spectrum at each before moving to the next. Therefore, the imaging micro-XRF system combines the automated sample movement with fast EDS elemental analysis. The sample is rapidly scanned through the X-Ray beam, and spectra are continuously read from the detector and correlated to a particular position on the sample. The distribution of a particular element can be displayed by plotting an image of the element's peak intensity at each pixel position. The result are detailed false coloured images showing areas of high and low concentration for each chosen element.

Since the detector captures a spectrum with information from all detectable elements simultaneously, multiple elements can be imaged without any time disadvantage. For this reason it was decided to gain the elemental map of several elements even if some of them give no information: Al, Ba, Ca, Fe, K, Mg, Mn, Na, P, Si, S, Sr, Ti, Zr.

Modern micro-XRF imaging systems can allow acquisition of images over areas ranging from around $0.25\ mm^2$ through to $10 \times 10\ cm$ or larger. Thus, it is possible to analyze samples with a wide range of sizes, both on the macro and micro scale.

For our purposes X-Ray mapping was performed with a $68 \times 69 \mu m$ resolution and a spot size of $30 \mu m$ over sample areas of about $34.97 \times 20.08\ mm$. Each X-ray image was collected for 16 hours per sample with automated overnight run.

4.4.2 Image analysis

The digital image analysis on the resulting maps was necessary to derive the relative abundances of the rock constituents, i.e., phenocrysts and groundmass, and the textural features of the various mineral phases. The maps (see Appendix A for all the acquired maps) were processed with open-source software packages (ImageJ v1.48 and MultiSpec v3.4).

A pre-processing step of contrast/brightness adjustment and noise reduction preceded for each elemental map. It was important to carefully find the right combination of parameters for each map singularly. Moreover, being the maps dimensions confined ($34.97mm \times 20.08mm$), applying noise filters such as *remove outliers* can be chancy and can lead to a loss of information irremediably.

The most significant maps from each sample were then superimposed and analysed as multispectral images (3 maps at a time in the three channel R: red, G: green, B: blue), in which the various mineral phases were identified by their chemical composition and segmented according to manually defined training pixels. Just to give an example, quartz can easily identify selecting Ca (R), Fe (G), and Si (B) maps: pixels representing quartz appear blue because in this phase there is neither calcium nor iron.

Lastly, classified images were obtained, after ECHO spectral/spatial classification with Fisher's linear discriminant algorithm; the classified images were subjected to colour thresholding and, for each colour-assigned constituent and phase, particle analysis was performed.

Quantitative textural and mineralogical data were extracted through calculation of the following descriptors of size and shape of each discrete grain: area, perimeter, Feret diameter, circularity, aspect ratio.

The Feret diameter is the longest distance between any two points along the selected particle boundary, i.e., the maximum dimension of a grain. Circularity is calculated as $4\pi \cdot area/perimeter^2$: a value of 1 indicates a perfect circle, values approaching 0 denote an increasingly elongated shape. Aspect ratio AR = Feret diameter/minimum Feret diameter: the ratio between the major and minor axes of an ellipse fitted to the selected particle boundary, thus expressing the average degree of elongation of that grain.

5 Results and Discussion

In this chapter, the main results are reported. Thermal conductivity data from previous and present works are reported (De Lullo for dolomites, Buggiarin for trachytes). Then, density and porosity of the samples are discussed, mineralogical content is analysed and, finally, texture is taken into account. For the sake of clarity, results on dolomites and trachytes are considered separately.

5.1 Thermal conductivity

This section is dedicated to characterization of the thermal properties. Thermal measurements on dolomites have been performed on three samples (C-B-Dol_002, C-B-Dol_004, C-B-Dol_007). Two trachyte samples from Euganean Hills (1 and 22B) have been considered; then two cubes of trachyte from a different quarry have been thermally analysed.

- ***Dolomites***

De Lullo (2016) conducted several thermal measurements on dolomite samples using both Isomet and C-Therm technologies, in anhydrous (dry samples) and wet (water saturated samples) conditions. Among the two instruments only C-Therm results are considered, since the comparison with the Isomet device shows both better precision and accuracy.

The main results for both dry and saturated samples are reported in Table 5.1. The subscripts $\parallel$ and $\perp$ refer to two mutually orthogonal faces of the sample, parallel and perpendicular with respect to the stratification respectively. Data reported in table are the results of the mean of 8 thermal conductivity values for each of 5 points along the diagonals of each face. The ratio $\lambda_{\parallel}/\lambda_{\perp}$ gives the anisotropy factor. A material can be considered isotropic when the factor of

Table 5.1 *Thermal conductivity data of dolomite samples C-B-Dol_002, 004, and 007 from De Lullo (2016). Results on both dry and wet conditions are reported.*

C-Therm - Dry samples

Sample	λ_{II} W/mK	$\lambda_{\perp}$ W/mK	Anisotropy	λ_{mean} W/mK
C-B-Dol_002	5.111	4.853	1.05	4.982
C-B-Dol_004	3.434	3.544	0.97	3.489
C-B-Dol_007	5.215	5.186	1.01	5.201

C-Therm - Saturated samples

Sample	λ_{II} W/mK	$\lambda_{\perp}$ W/mK	Anisotropy	λ_{mean} W/mK
C-B-Dol_002	5.15	4.962	1.04	5.056
C-B-Dol_004	3.497	3.52	0.99	3.509
C-B-Dol_007	5.172	5.151	1	5.161

anisotropy is equal to 1.0, slightly anisotropic when it present values of 0.9 or 1.1, and anisotropic when it exceeds 1.1 (Di Sipio et al., 2014). Since the anisotropy factor is 1.05 for C-B-Dol_002, 0.97 for C-B-Dol_004, and 1.01 for C-B-Dol_007, they are considered slightly isotropic and the mean thermal conductivity value λ_{mean} was assigned to them. Sample C-B-Dol_007 has the highest thermal conductivity (5.201 W/mK) while C-B-Dol_004 has the lowest one (3.489 W/mK). C-B-Dol_002 has the intermediate value of 4.982 W/mK.

Data referring to saturated sample are not considered for the moment.

- ***Trachytes***

The determination of thermal properties of some rocks from Euganean Hills was the main target of Buggiarin's work (2014). He used the laboratory instrument "Mathis TCi Thermal Property Analyzer" (C-Therm) to measure thermal conductivity and thermal effusivity directly (other thermal quantities can be indirectly determined) on dry samples. The measurements were conducted on two smooth faces, parallel and perpendicular with respect to the stratification. Table 5.2 reports the thermal conductivity values of the two mutually orthogonal faces λ_{II} and $\lambda_{\perp}$ the ratio of which ($\lambda_{II}/\lambda_{\perp}$) gives the anisotropy factor. Since this factor is 1 for sample 22B and 0.93 for sample 1, they were considered isotropic and the mean thermal conductivity value λ_{mean} was assigned to them: 1.58 W/mK for sample 1 and 1.36 W/mK for sample 22B.

Table 5.2 *Thermal conductivity data of trachyte samples 1 (Monte Merlo) and 22B (Rocca Pendice) from Buggiarin (2014) and the present work. C-Therm instrument was used on dry samples.*

BUGGIARIN (2014)

Sample	λ_{II} W/mK	$\lambda_{\perp}$ W/mK	Anisotropy	λ_{mean} W/mK
1	1.53	1.65	0.93	1.58
22B	1.36	1.36	1	1.36

PRESENT WORK

Sample	λ_{II} W/mK	$\lambda_{\perp}$ W/mK	Anisotropy	λ W/mK	SD
1	x	x	x	1.913	0.006
22B	x	x	x	1.876	0.004

A comparison with literature values revealed that thermal conductivities of $1.58\ and\ 1.36\ W/mK$ could be very low for trachytes. For this reason, it was decided to repeat the measurements, using the C-Therm instrument but with a new surface plane tool probe provided by the C-Therm factory. The isotropy of the samples was assumed, so only one face was selected, polished, and analysed. On the selected surfaces, eight measures for each of five points were acquired. Then, maximum and minimum values on each point were excluded and median and standard deviation were computed. Results are reported in Table 5.2. Thermal conductivity of $1.913 \pm 0.006\ W/mK$ was found on sample 1 and sample 22B has a value of $1.876 \pm 0.004\ W/mK$. These values are quite low for this type of extrusive rocks; anyway, they cleary indicate that sample 1 has a thermal conductivity higher than the one of sample 22.

In order to make some comparisons with the samples from Monte Merlo and Rocca Pendice, it was decided to measure the thermal conductivity of two cubes of trachyte from Zovon (Rovarolla quarry), previously characterized from a textural and compositional point of view by Germinario (2016). The results of measurements performed with C-Therm are reported in Table 5.3. The obtained anisotropy factors were equal to 1.01 (RVL_01) and 1.00 (RVL_02). Such experimental values allowed to consider the two samples as isotropic, so only λ_{mean} was used: $1.95\ W/mK$ for sample RVL_01 and $1.94\ W/mK$ for sample RVL_02. Trachytes from Zovon (Rovarolla) show a higher conductivity with respect to the samples from the other two quarries and this is an important information that will be discussed in section 5.5.

Table 5.3 *Thermal conductivity data of trachyte samples from Zovon quarry measured in the present work.*

C-Therm - Dry samples				
Sample	$\lambda_{\parallel}$ W/mK	$\lambda_{\perp}$ W/mK	Anisotropy	λ_{mean} W/mK
RVL_01	1.95	1.95	1.00	1.95
RVL_02	1.94	1.94	1.00	1.94

5.2 Density

Density is an important petro-physical property, and different types of density have been defined according to the different rock components. In the present study, three density types have been considered:

- Bulk density: mean density of the whole rock cubes volume, including open and closed pores.
- Granulate density: mean density of the solid material plus the closed pores.
- Matrix density: mean density of the solid matrix material.

- ***Dolomites***

Bulk density can be determined geometrically, so three cubes for each sample (A, B, and C) were prepared, and volume and weight were measured after drying the materials in oven. All the measured parameters for each cube and the calculated average bulk density for each sample are reported in Table 5.4. The sample with the highest value is C-B-Dol_007, with a density of $2.783 \pm 0.073\ g/cm^3$, while the sample with the lowest density is C-B-Dol_004 with a value of $2.711 \pm 0.019\ g/cm^3$. The C-B-Dol_002 sample has an intermediate density, with a value of $2.736 \pm 0.033\ g/cm^3$.

The bulk density was also calculated by De Lullo (2016) with the saturation method and the results of her measurements for three cubes (B, C, and D) of the same samples analyzed in the present study are also reported in Table 5.4. The sample with the highest value is C-B-Dol_004 with a density of $2.742 \pm 0.007\ g/cm^3$ while the sample with the lowest λ is C-B-Dol_002 with a value of $2.735 \pm 0.004\ g/cm^3$.

Table 5.4 *Present work: Volume, mass, and computed bulk density of three cubes for each dolomite sample. De Lullo (2016): Bulk density of other three cubes. Average values and standard deviations are reported.*

PRESENT WORK

Sample	C-B-Dol_002			C-B-Dol_004			C-B-Dol_007		
Cube	**A**	**B**	**C**	**A**	**B**	**C**	**A**	**B**	**C**
Average cube side (mm)	25.089	20.150	12.565	19.946	15.166	14.288	25.169	24.909	14.208
Volume (cm^3)	15.793	8.181	1.984	7.935	3.488	2.917	15.944	15.455	2.868
Mass (g)	43.329	22.261	5.445	21.474	9.440	7.932	44.433	43.431	7.891
Bulk Density (g/cm^3)	2.744	2.721	2.745	2.706	2.706	2.720	2.787	2.810	2.752
Average Bulk Density (g/cm^3)	2.736 ± 0.033			2.711 ± 0.019			2.783 ± 0.073		

DE LULLO (2016)

Sample	C-B-Dol_002			C-B-Dol_004			C-B-Dol_007		
Cube	**B**	**C**	**D**	**B**	**C**	**D**	**B**	**C**	**D**
Bulk Density (g/cm^3)	2.739	2.735	2.730	2.733	2.747	2.746	2.742	2.737	2.739
Average Bulk Density (g/cm^3)	2.735 ± 0.004			2.742 ± 0.007			2.739 ± 0.003		

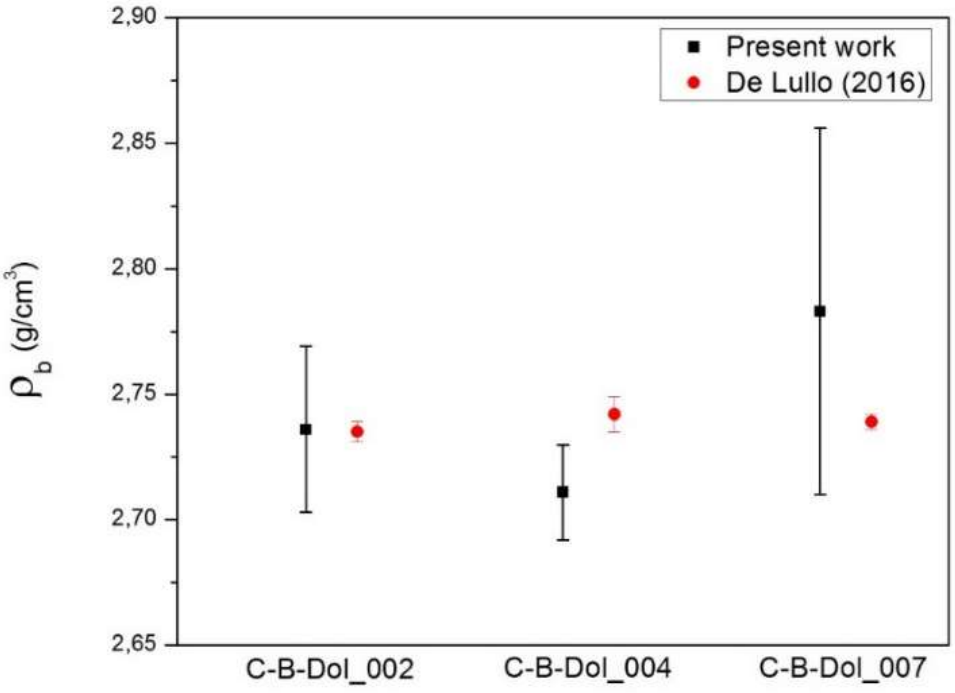

Figure 5.1 *Bulk density for three sample of dolomite and computed standard deviation. In black results of the present work, in red results from De Lullo (2016).*

Densities obtained in the present work and by De Lullo, with relative errors, are compared in Figure 5.1. A good correspondence can be observed for sample C-B-Dol_002, while it is within the error for sample C-B-Dol_007. There is a little difference in sample C-B-Dol_004, with densities of $2.711 \pm 0.019\ g/cm^3$ (present work) and $2.742 \pm 0.007\ g/cm^3$ (De Lullo).

As regards the variation of thermal conductivity with density (present work data) for the three dry samples of dolomite, the increasing thermal conductivity clearly corresponds to an increase of density. Indeed, sample C-B-Dol_007, that has the highest conductivity, it is characterized by the highest bulk density.

Granulate density and **matrix density** were measured by means of a helium pycnometer, on granulates ($1mm <$ grain size $< 3 - 4mm$) and micronized powders (in which the original structure is lost and all pores are destroyed), respectively. For each sample, 3 powders and 4 granulates were analysed. The complete report of the pycnometer measurements is reported in Appendix B.

Table 5.5 *Bulk, granulate and matrix density for three samples of dolomites. Data computed using pycnometer results. * indicates data calculated using diffraction results.*

	Density (g/cm^3)				Thermal Conductivity (W/mK)
Sample	Bulk	Granulate	Matrix	Matrix*	
C-B-Dol_002	2.74 ± 0.03	2.84 ± 0.001	3.08 ± 0.07	2.86	4.98
C-B-Dol_004	2.71 ± 0.02	2.81 ± 0.01	3.09 ± 0.06	2.86	3.49
C-B-Dol_007	2.78 ± 0.07	2.83 ± 0.002	3.10 ± 0.1	2.86	5.20

A summary of bulk, granulate and matrix densities and relative errors is reported in Table 5.5. As expected, the bulk density is lower than the granulate density, that is lower than the matrix one. Nevertheless, a matrix density of $3.08 - 3.10\ g/cm^3$ for a dolomite is too high compared with literature data. Trying to overcome this problem, matrix density was determined also in a different way. The density of a composite material such as a rock can be calculated from the densities and volume fraction of each crystalline component.

For a two-component system, the density is calculated through the following equation,

$$\rho_{mix} = A\rho_A + B\rho_B \tag{5.1}$$

where ρ_{mix} is the density of the mixture, ρ_A is the density of component A, ρ_B is the density of component B, A and B are the volume fraction of A and B, respectively (and so $B = 1 - A$). In the present case, it was decided to multiply the percentage of each phase identified through diffraction to the matrix density of the phase itself. Expanding this into a general system with n components the density of the material is expressed by the following equation:

$$\rho_{matrix} = (\%A_1\rho_{A1} + \%A_2\rho_{A2} + \cdots + \%A_n\rho_{An})/100 \tag{5.2}$$

where ρ_{matrix} is the matrix density of the sample, ρ_{A1} is the density of component A_1, ρ_{A2} is the density of component A_2; $\%A_1$ and $\%A_2$ are the weight percentages of the phases A_1 and A_2(and so $\%A_1 + \%A_2 + \cdots + \%A_n = 100\%$). Phase percentages and densities have been obtained through Rietveld refinements of the diffraction data. The matrix densities computed for each specimen are reported in Appendix B. The mean values obtained for each sample (C-B-Dol_002, 004, and 007) are marked by an "*" in Table 5.5. The three samples have the same matrix density ($2.86\ g/cm^3$) and this is not an unexpected result since their mineralogy is pure dolomite. Indeed, the dolomite mineral has a density of $2.86\ g/cm^3$. Matrix densities previously calculated are thus no more considered for porosity determinations (see next section about porosity).

The reasons of such high matrix density values measured by the pycnometer are not clear yet. Preparing the sample is the first step in obtaining accurate results from the pycnometer. Sample must be free of moisture in order to obtain true sample weight and to avoid the distorting effect of water vapor on the volume measurement. This could be a possible cause since powders were not dried in oven and, in addition, they remained exposed to air for relative long time intervals during the measurements. Then, it is important to mantain a constant temperature inside the unit because a change in temperature could alter analysis results. Possible temperature fluctuations were avoided leaving the cap always on the cell chamber except when actually inserting or removing a sample. Other malfunctions of the pycnometer could be caused by gas pressure leaks or by too high pressures. The issue could be deeply evaluated in the future.

- ***Trachytes***

Bulk density can be determined geometrically, so three cubes for each sample (A, B, and C) were prepared, and volume and weight were measured after drying the materials in the oven at 75°C for at least 24hours. All the measured parameters for each cube and the calculated average bulk density for each sample are reported in Table 5.6. Sample 1 has the highest density with $2.439 \pm 0.034\ g/cm^3$ while the sample 22B has a density of $2.261 \pm 0.017\ g/cm^3$.

Bulk densities determined by Stefano Buggiarin with a saturation method are also reported in Table 5.6. There is a correspondence with the previous data. Indeed, sample 1 has the highest density of $2.450 \pm 0.016\ g/cm^3$ and the sample 22B has the lowest one, with a value of $2.326 \pm 0.089\ g/cm^3$. Bulk densities from both the present work and the previous one are plotted in the same graphs (Figure 5.2) where a relationship is clear. In particular, data referring to sample 1 are very close and those referring to sample 22B can be compared within the error.

As regards the variation of thermal conductivity with bulk density (present laboratory data) for the two dry samples of trachyte, sample 1 has the highest λ and it also has the highest bulk density and vice versa for sample 22B.

Table 5.6 *Present work: Volume, mass, and computed bulk density of three cubes for each trachyte sample. Buggiarin (2014): Bulk density of other three cubes. Average values and standard deviations are reported.*

PRESENT WORK

Sample	Trachyte_1			Trachyte_22B		
Cube	**A**	**B**	**C**	**A**	**B**	**C**
Average cube side (mm)	19.503	20.236	20.288	23.246	25.311	21.984
Volume (cm^3)	7.419	8.286	8.350	12.561	16.215	10.625
Mass (g)	18.208	20.149	20.292	28.406	36.551	24.101
Bulk Density (g/cm^3)	2.454	2.432	2.430	2.261	2.254	2.268
Average Bulk Density (g/cm^3)	2.439 ± 0.034			2.261 ± 0.017		

BUGGIARIN (2014)

Sample	Trachyte_1			Trachyte_22B		
Cube	**1**	**2**	**3**	**1**	**2**	**3**
Bulk Density (g/cm^3)	2.454	2.464	2.433	2.263	2.428	2.288
Average Bulk Density (g/cm^3)	2.450 ± 0.016			2.326 ± 0.089		

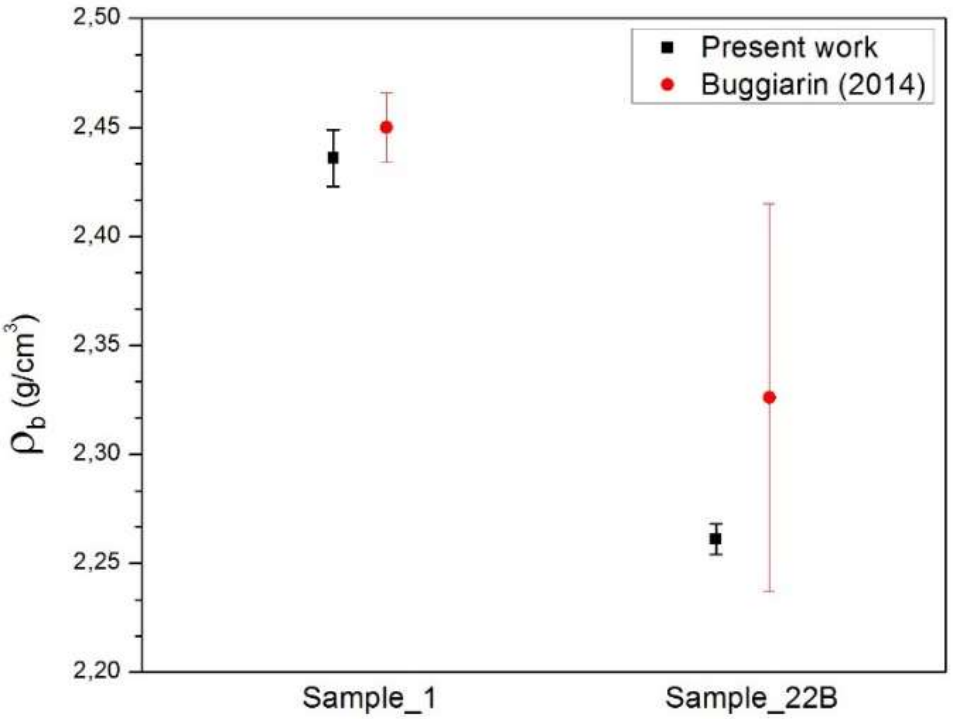

Figure 5.2 *Bulk density for two samples of trachyte and computed standard deviation. In black results of the present work, in red results from Buggiarin (2014).*

Granulate density and **matrix density** were measured by means of a helium pycnometer, on granulates ($1mm$ < grain size < $3-4mm$) and micronized powders (in which the original structure is lost and all pores are destroyed), respectively. For each sample, 3 powders and 2 granulates were selected and then analysed. The complete report given by the pycnometer is reported in Appendix B.

Table 5.7 *Bulk, granulate, matrix density for two samples of trachyte. Data computed using helium pycnometer results.*

	Density (g/cm^3)			Thermal Conductivity (W/mK)
Sample	Bulk	Granulate	Matrix	
Trachyte_1	2.44 ± 0.03	2.62 ± 0.004	2.81 ± 0.11	1.91
Trachyte_22E	2.26 ± 0.02	2.63 ± 0.01	2.87 ± 0.07	1.88

A summary of bulk, granulate and matrix densities and relative errors is reported in Table 5.7. As expected, the bulk density is lower than the granulate density, that is lower than the matrix one. Since densities measured on dolomites were higher than expected ones, the doubt that also for trachytes pycnometer gives distorted results was legitimate. Anyway, the alternative method for the calculation of matrix density previously tested on dolomites seems to not fit well in trachytes. In the future, the pycnometer functionality will be verified but for the moment densities of $2.81 \pm 0.11\ g/cm^3$ for sample 1 and $2.87 \pm 0.07\ g/cm^3$ are used for porosity computations.

5.3 Porosity

Porosity can be determined in different ways. In this study, the gas expansion method was tested and image analysis was applied to images acquired through different methods (for dolomites only scanned images were analysed, while for trachytes also micro-XRF maps were useful for porosity investigations).

It is important to underline that the results of each method will be discussed individually because they correspond to different types of pores, considered under different points of view. For example, data obtained from pycnometer outputs are given as volume fractions: they express the fraction of the volume of voids over the total volume considered (3D). On the other hand, the values obtained through image analysis techniques give area fraction values as output, that is the fraction of the area of voids over the total considered area (2D). Furthermore, the gas expansion method measures the porosity in a $3\ nm - 4\ mm$ dimensional range, while the image analysis on scans only discriminates pores bigger than the maximum resolution limit (in our case, employing a maximum resolution of $8 \times 8 \mu m$, only pores with dimensions bigger than $20 \mu m$ were identified). A single comparison was possible between open porosity results from this work and those from De Lullo analyses.

- ***Dolomites***

Bulk (by geometric means), granulate (though pycnometer), and matrix (from diffraction data) densities reported in Table 5.5 were used to compute three types of porosity: total, open and closed porosity.

Total porosity was computed with the equation:

$$\phi = 100 - (\rho_b / \rho_{matrix} \times 100) \quad (5.1)$$

Two columns of total porosity are reported in Table 5.8 because two matrix densities were used. Results in the first column were computed using densities from pycnometer measurements. The total in the grey column are clearly to high than the expected one, according to other analysis. Same observations may be provided for density outcomes. Obviously these results cannot be further used. Data reported in the second column (calculated using diffraction data: percentages and minerals density) are instead acceptable, according to literature and visual observations. Sample C-B-Dol_007 has the lowest total porosity (2.70%) and sample C-B-Dol_004 the highest one (5.22%). Sample C-B-Dol_002 has an intermediate porosity of 4.29%.

Open porosity was computed with the equation:

$$\phi = 100 - (\rho_b / \rho_{granulate} \times 100) \quad (5.2)$$

Samples C-B-Dol_002 and C-B-Dol_004 show the same open porosity of 3.64 ± 0.01 %, while sample C-B-Dol_007 has an open porosity equal to 1.73 ± 0.03 %.

These values were first of all compared with De Lullo results (see Figure 5.3). The saturation method provided the highest average open porosity of 3.721% for C-B-Dol_002 and the lowest percentage of 2.863% for C-B-Dol_004; C-B-Dol_007 has an open porosity of 3.047%.

Amongst the two methods, the pycnometer remains the most reliable one because the saturation method has the key limitation linked with the difficulty of the imbibing fluid (water in this case) to purge air from the smallest nm-sized pores. For this reason, it was decided to only consider data obtained in the present work. Other data are necessary but, for the moment, these results clearly confirm that thermal conductivity is higher for samples with low porosity and vice versa.

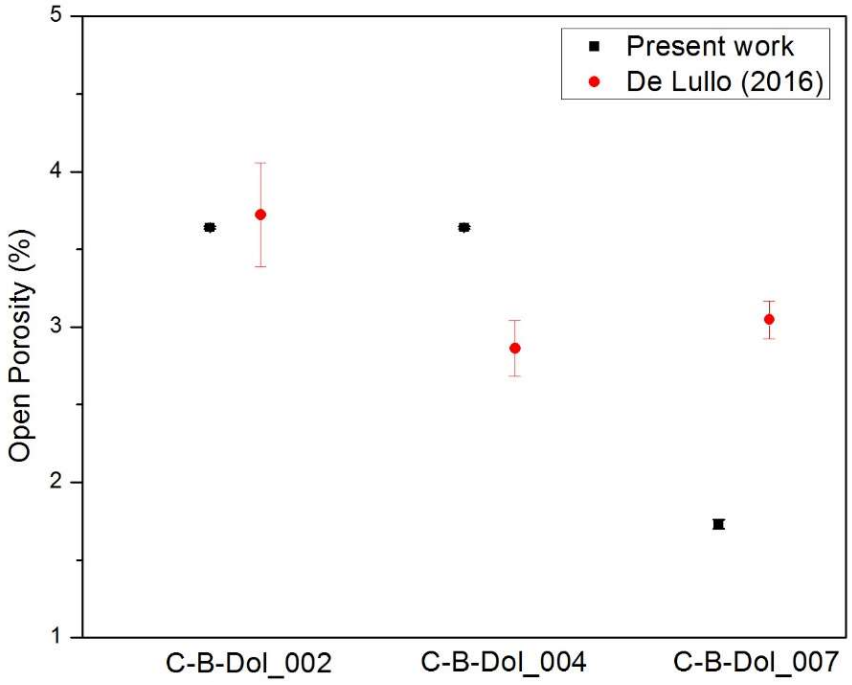

Figure 5.3 *Comparison between open porosity of three samples of dolomite measured with pycnometer (present work) and through saturation method (De Lullo, 2016).*

Closed porosity was calculated as the difference between total and open porosity, so its accuracy strictly depends on the reliability of the other two values. The results are reported in grey in Table 5.8 because closed porosity is not more considered for our aims.

Table 5.8 *Total, open, and closed porosity for three samples of dolomites. * indicates data calculated with diffraction results. The others are computed with pycnometer results. Data in grey have not been considered.*

	Porosity (%)					Thermal Conductivity (W/mK)
Sample	Total	Total*	Open	Closed	Closed*	
C-B-Dol_002	11.22 ± 0.03	4.29	3.64 ± 0.01	7.58 ± 0.04	0.65	4.98
C-B-Dol_004	12.17 ± 0.03	5.22	3.64 ± 0.01	8.53 ± 0.03	1.58	3.49
C-B-Dol_007	10.25 ± 0.06	2.70	1.73 ± 0.03	8.53 ± 0.06	0.97	5.20

The results from image analysis on scanned images are reported hereafter. Two surfaces (E and F) were selected for each dolomite sample. Figure 5.4 reports the true-colours scan and the binary image of sample C-B-Dol_007E. The external limit of the sample does not correspond to the border of the area on which the pores analysis was performed. In fact, a polygon was created and all black pixels outside the line were not taken into account. The chromium oxide treatment leaves a residue toward the borders of the sample, while the polished

surface can be easily clean with gloves. Consequently, the creation of a polygon was necessary in order to avoid this "noise" coming from areas not related to the surface.

The percentage of pores in each image is reported in Table 5.9. Except for sample C-B-Dol_007, data testify a variability not only on the same lithology but also on within the same sample. For example, the two surfaces E and F cut from the same C-B-Dol_002 sample show a percentage of pore of 1.32% (E) and 0.51% (F) respect to the considered area.

Table 5.9 *Porosity percentages of three samples of dolomite measured on two different surfaces.*

Sample	Surface	Porosity (%)
C-B-Dol-002	E	1.32
	F	0.51
C-B-Dol-004	E	0.56
	F	0.28
C-B-Dol-007	E	1.42
	F	1.38

In order to make the results comparable, nearly equal surfaces should be obtained for all samples. The surfaces should be as larger as possible to be representative of the entire sample but for some samples it's not possible to gain large areas (see C-B-Dol_004F respect to C-B-Dol_004E). Reduced investigation areas could mean over- or underestimated porosities, especially in sedimentary rocks where lithology shows frequent changes related to the stratification. In conclusion, image analysis on scanned images could not be the best method to be applied on dolomites and in general on sedimentary rocks. If He pycnometer actually is a reliable technique, porosity results computed from pycnometer reports could be enough. In the future this aspect could be better investigated.

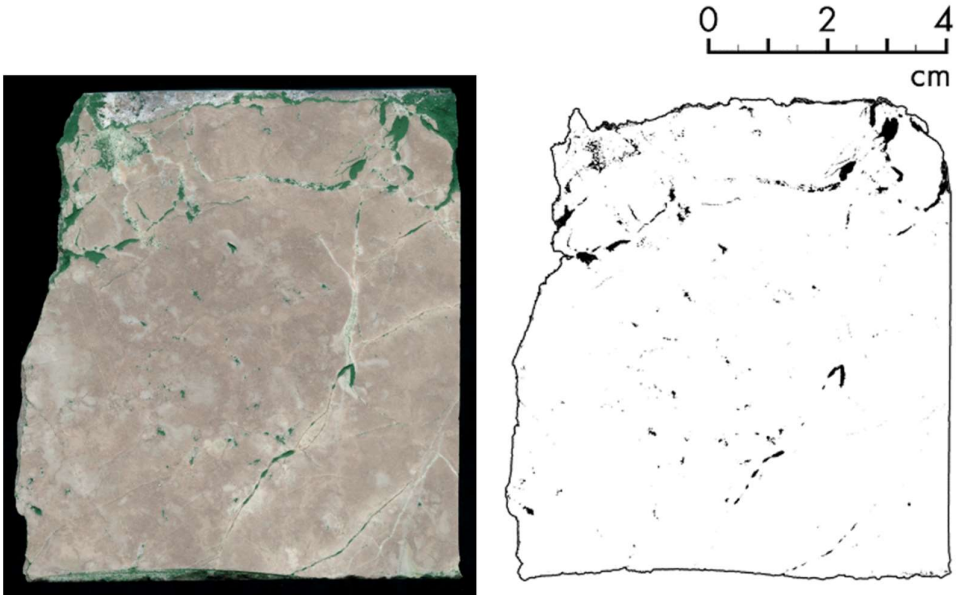

Figure 5.4 *True-colours (on the left) and binary image (on the right) of sample C-B-Dol_007 E.*

- ***Trachytes***

Previously reported bulk (by geometric means), granulate and matrix (though pycnometer) densities results were used to compute three types of porosity: total, open and closed porosity.

Table 5.10 *Total, open, and closed porosity for two samples of trachyte. Data computed with pycnometer results. Data in grey have not been considered.*

	Porosity (%)			Thermal Conductivity (W/mK)
Sample	Total	Open	Closed	
Trachyte_1	13.28 ± 0.05	7.08 ± 0.02	6.20 ± 0.06	1.91
Trachyte_22B	21.09 ± 0.03	13.94 ± 0.01	7.15 ± 0.04	1.88

Total porosity was computed with the equation:

$$\phi = 100 - (\rho_b/\rho_{matrix} \times 100) \quad (5.3)$$

The results are reported in Table 5.10. Sample 1 has a total porosity of $13.28 \pm 0.05\%$ while the total porosity of sample 22B is $21.09 \pm 0.03\%$.

Open porosity was computed with the equation:

$$\phi = 100 - (\rho_b / \rho_{granulate} \times 100) \quad (5.4)$$

The results are also reported in Table 5.10. Sample 1 has the lowest value of $7.08 \pm 0.02\%$ and sample 22B has an open porosity of $13.94 \pm 0.01\%$ that is almost double than the first. These values were compared with the Buggiarin ones. The saturation method is not a reliable procedure because it tends to underestimate the total porosity. Indeed, this method cannot take into account the small pores, where the water cannot fill the voids. On the contrary, the helium pycnometer is considered amongst the most accurate techniques for measuring effective porosity because helium has small molecules that rapidly penetrate small pores. For this reason, it was expected a correlation between results obtained with the two techniques, but the open porosity determined through gas expansion method was expected to be higher. Figure 5.5 confirms those predictions.

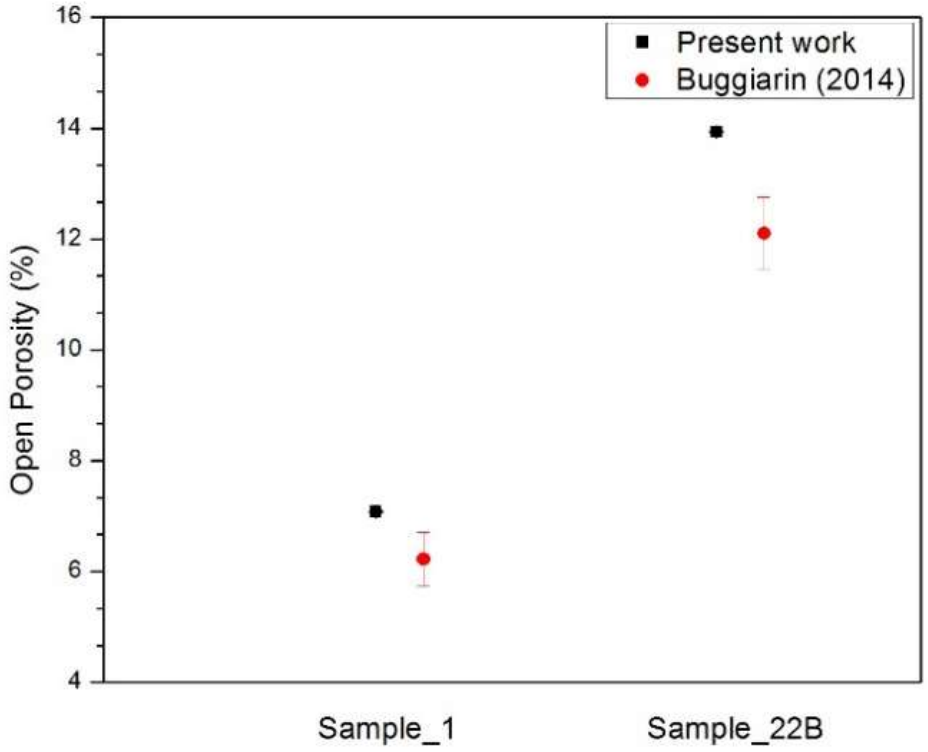

Figure 5.5 *Comparison between open porosity of two samples of trachyte measured with pycnometer (present work) and through saturation method (Buggiarin, 2014).*

Closed porosity was calculated as difference between total and opened porosity so its accuracy strictly depends on the reliability of the other two values. The results are reported in grey in Table 5.10 because closed porosity was not more considered for our aims.

The results from image analyses are reported hereafter. Regarding scanned images, only one surface was selected for each sample, and the analysis was performed on binary images (see Figure 5.6). The determined amount of voids is equal to 2.22% of the investigated area for sample 1, and to 6.16% for sample 22B. Looking at binary pictures, it can also be noted a difference in pores size: sample 22B has bigger pores than those of sample 1.

Table 5.11 *Porosity percentages of two samples of trachyte measured on both scanned images and elemental maps.*

	Porosity (%)	
Sample	Scans	μ-XRF Maps
1	2.22	1.45
22B	6.16	2.25

Micro-XRF elemental maps were acquired for the textural analysis (see section 5.5) but they proved to be useful also for the porosity. From the false colours the class corresponding to pores was isolated through a threshold operation and the binary images were saved in order to be analysed in ImageJ. The two percentages of pores respect to the considered areas are reported in Table 5.11: 1.45% for sample 1 and 2.25% for sample 22B. As it is observable in Figure 5.7, the thin section of sample 22B does not cover the entire area of analysis, but the empty spaces were not considered as pores and thus they were excluded from the final counting. The area of investigation for sample 1 is of about $7.02\ cm^2 (34.97mm \times 20.08\ mm)$, while for sample 22B the total investigated area is about $6.78\ cm^2$. Despite the percentages refer to areas of different dimensions, the images confirm, at a different scale, the higher porosity of sample 22B and also the difference in pore size of the two samples: trachyte 22B has bigger pores than sample 1.

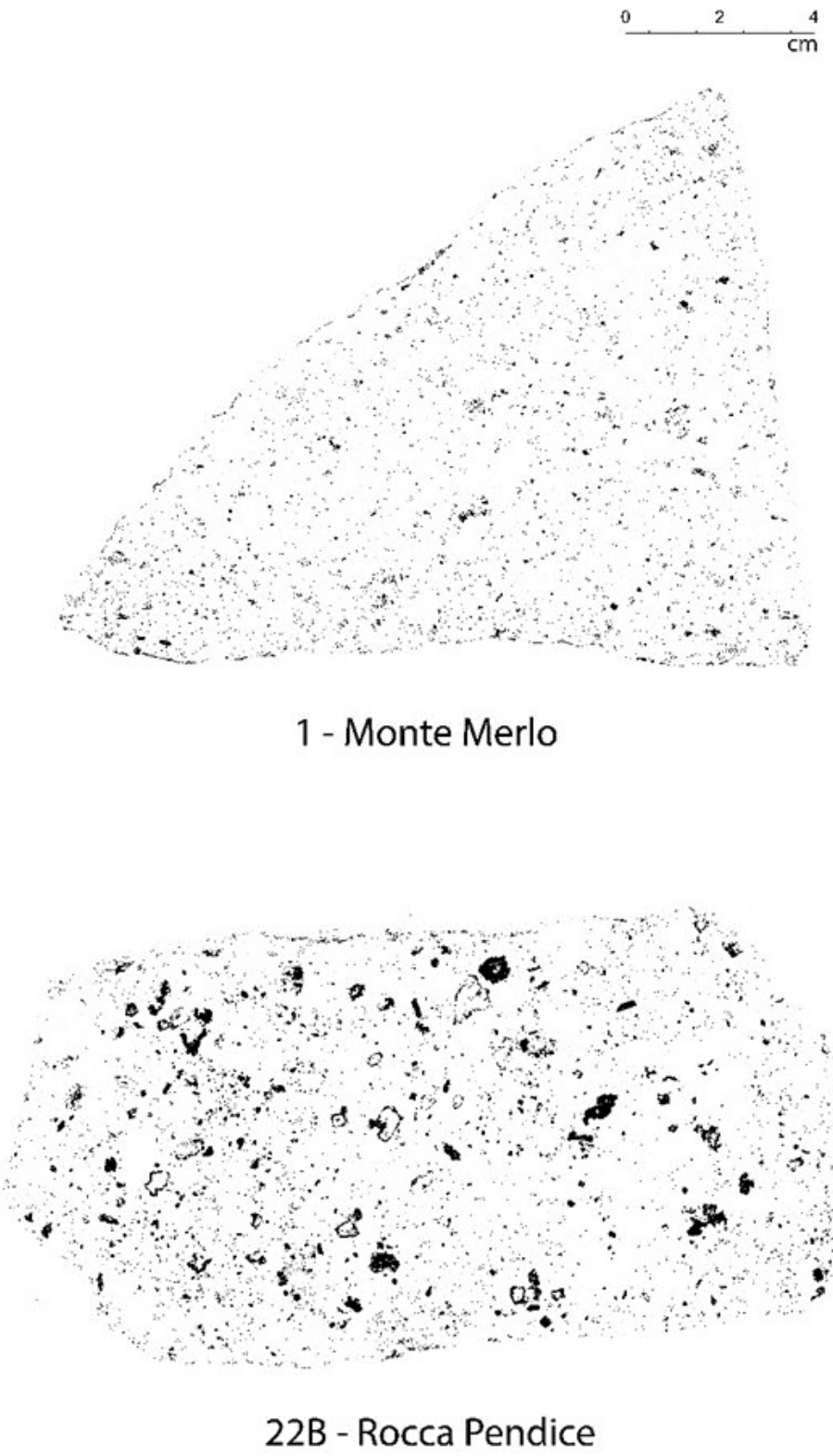

Figure 5.6 *Binary images obtained from scanned images of two trachyte samples.*

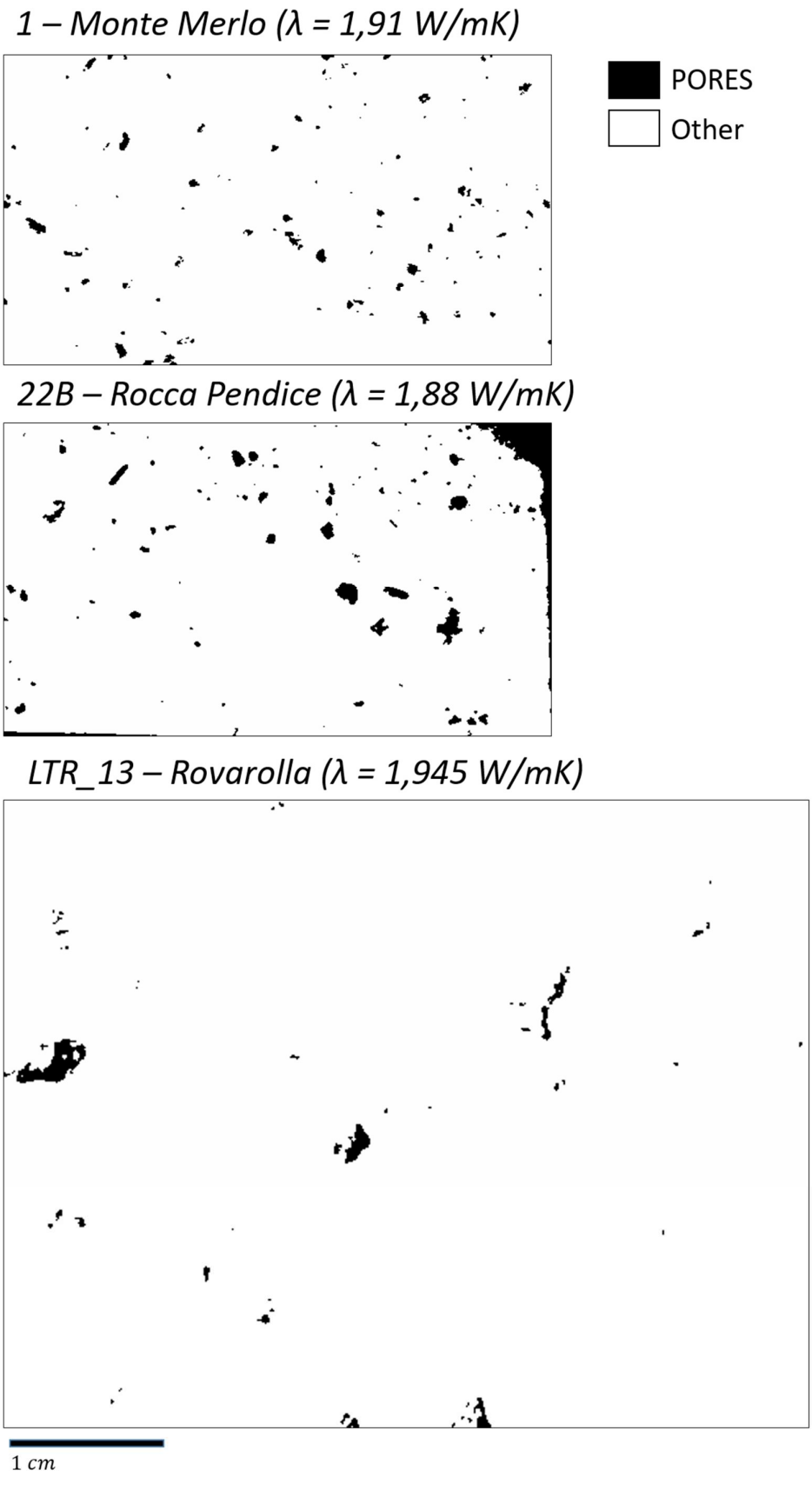

Figure 5.7 *Binary images of pores of trachyte sample 1, 22B, and LRT_13.*

5.4 Mineralogical content

In this section, the results of compositional analyses (X-ray diffraction and fluorescence) on samples are reported.

- ***Dolomites***

Three samples of dolomite were analysed and two different powders were prepared for each of them (E and F letters were used to differentiate them).

Two diffractograms related to sample C-B-Dol_002 are reported in Figure 5.8. They are nearly identical and it was easy to perform both the qualitative analysis and the structure refinement. The most intense peak (at about $36°2\theta$) is the principal peak of dolomite and such an intensity implies the presence of a peak in correspondence of its $K\beta$ contribute (this peak is indicated in figure by blue lines in both E and F specimens). Therefore, it was easy to identify the other two phases, quartz and calcite, through their main peaks, that are at 3.34Å and 3.03Å respectively.

Summarizing, both C-B-Dol_002 specimens are composed almost entirely of stoichiometric dolomite [$CaMg(CO_3)_2$]; little percentages of quartz (0.28% in E and 0.25% in F) and calcite (0.49% in E and 0.20% in F) are also present.

Diffractograms related to sample C-B-Dol_004 are reported in Figure 5.9. They are the most complicated ones. The reason lies in the fact that another population of dolomite is present within the sample. It is a non-stoichiometric dolomite composed by an excess of calcium [$Ca_{3.39}Mg_{2.61}C_6O_{18}$]. Moreover, there are also clay minerals; the structure of illite was used to describe the contribution related to the occurrence of phyllosilicates, but it could be also smectite or mixed-layers illite-smectite. The uncertainty is due to the fact that the intensities of peaks are limited and in some cases peaks are not clearly detectable.

The refinement at high 2θ angles is not perfectly correspondent to the experimental data due to lattice strain phenomena.

Both specimens are composed almost entirely by two populations of dolomite: stoichiometric dolomite (43.24% in E and 44.48% in F) and dolomite with an excess of Ca (53.20% in E and 52.30% in F); there is a little percentage of clay minerals (2.46% in E and 2.31% in F); the rest of the sample is composed by calcite (1.10% in E and 0.92% in F). Quartz is not present.

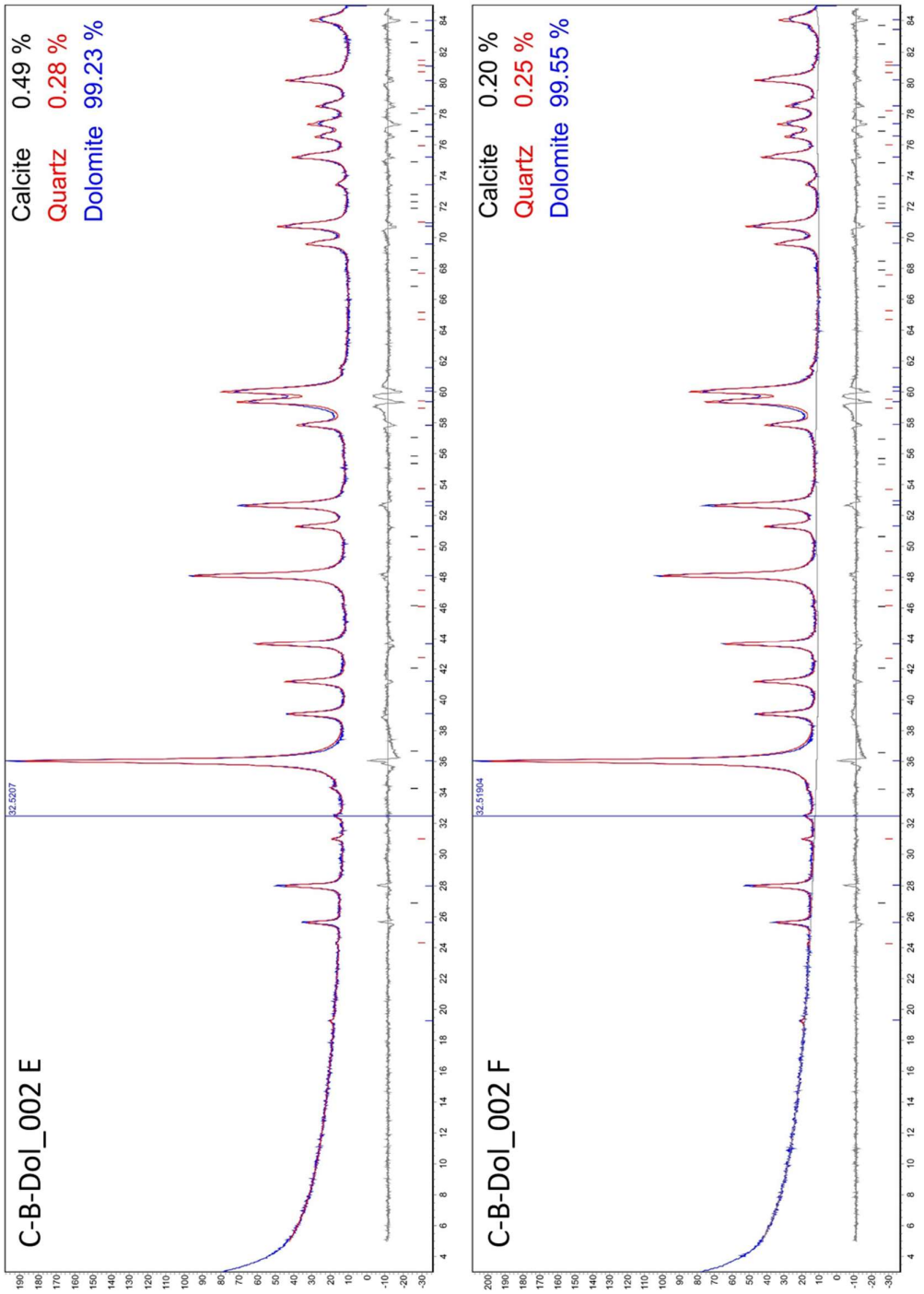

Figure 5.8 *Difractograms of C-B-Dol_002 E and F samples after Rietveld refinement with Topas software. Blue lines indicate the Kβ contribution of the main dolomite peak.*

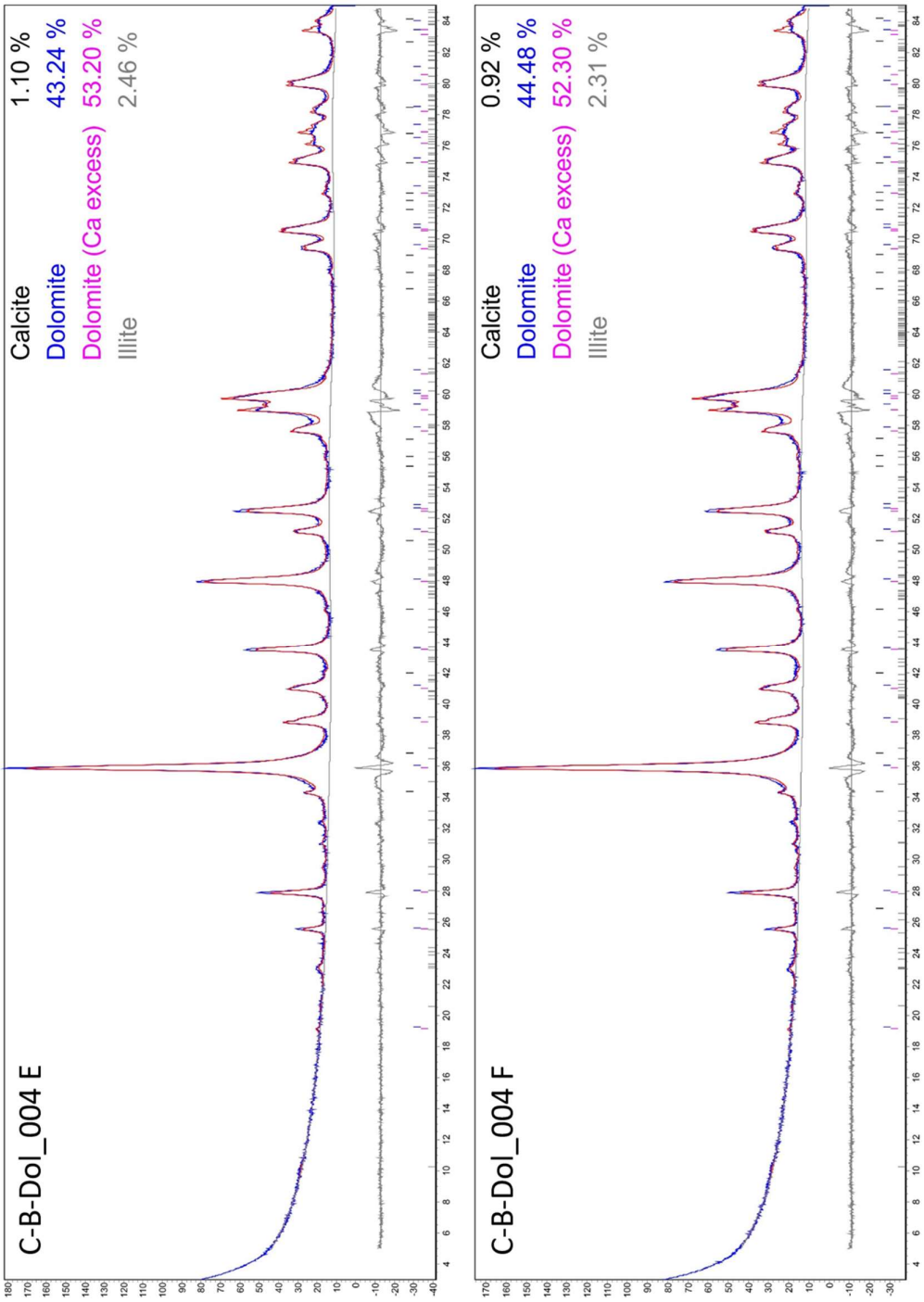

Figure 5.9 *Diffractograms of C-B-Dol_005 E and F samples after Rietveld refinement with Topas software*

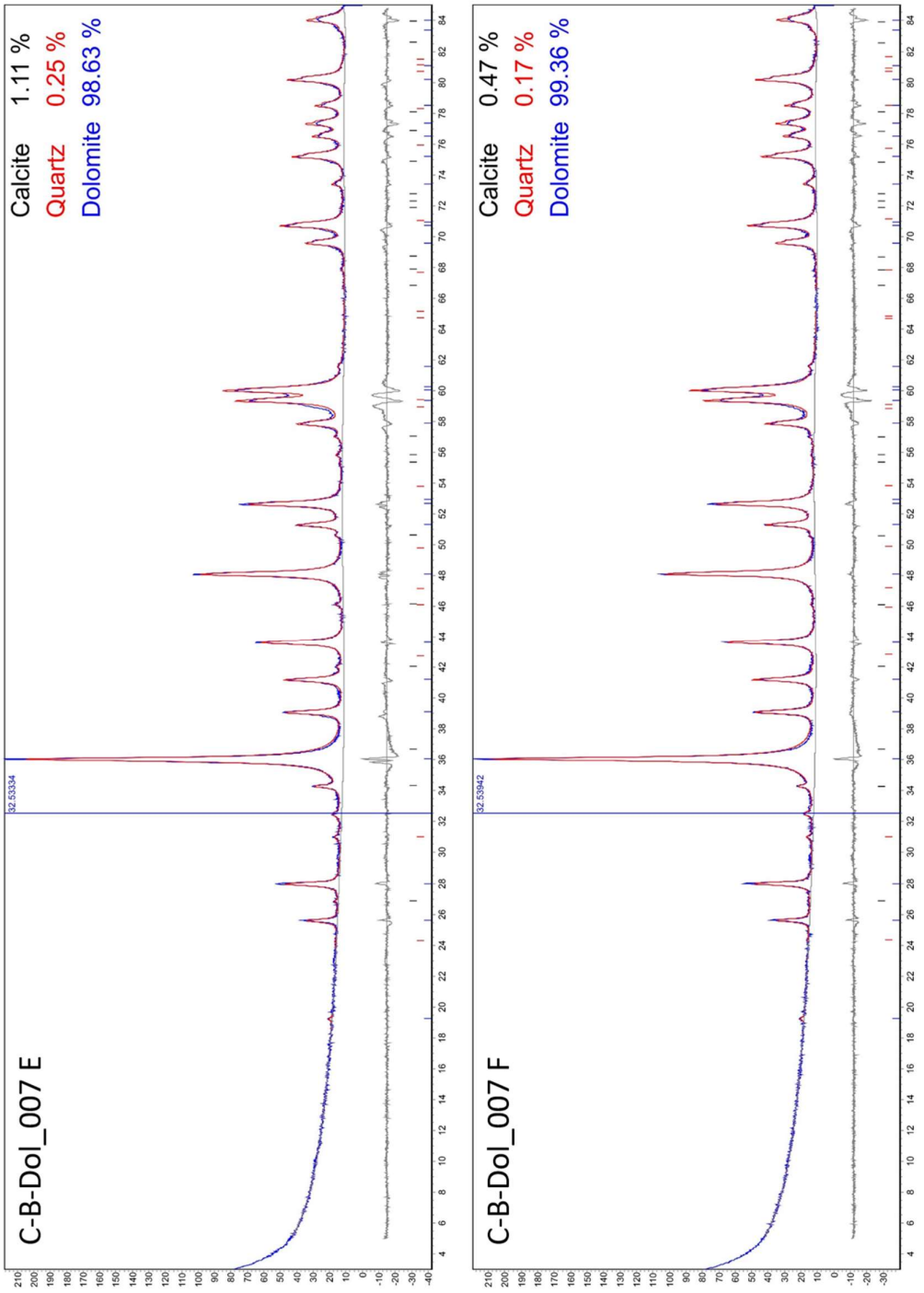

Figure 5.10 *Diffractograms of C-B-Dol_007 E and F samples after Rietveld refinement with Topas software. Blue lines indicate the Kβ contribution of the main dolomite peak.*

X-ray diffraction results of sample C-B-Dol_007 are reported in Figure 5.10. The Rietveld refinement indicated the presence of stoichiometric dolomite (the same of sample C-B-Dol_002) in very high percentage (98.63% in E and 99.36% in F) so it is a nearly pure dolostone with little quartz (0.25% in E and 0.17% in F) and calcite (1.11% in E and 0.47% in F) percentages. Differences in calcite quantities are probably due to sampling: sample C-B-Dol_007 is characterized by fractures often filled with calcite, so a powder belonging to a piece of rock crossed by an important calcite-filled fracture could be characterized by a significant calcite component.

Samples C-B-Dol_002 ($\lambda = 4.982\ W/mK$) and 007 ($\lambda = 5.201\ W/mK$) don't show enough compositional differences to justify the gap in thermal conductivity values. In a preliminary step it was hypothesised that such variations in thermal behaviour was due to porosity (for sedimentary rocks it is one of the main controlling factors on thermal conductivity) and quartz content (it's the mineral with the highest λ). The porosity was investigated first (see section 5.2) and it actually seems to be a controlling factor. On the contrary, quartz is present in similar and very low percentages in both samples and thus it seems to be a negligible element. In the future, a third element considered by Clauser and Huenges (Clauser, 2011; Clauser and Huenges, 1995), namely the origin of sediments (from chemical or physical sedimentation process), will be considered.

Results from X-ray Fluorescence on dolomite samples are reported in Table 5.12. Sulfur (S) data are in italics because they are considered semi-quantitative, while values reported as "<X" are below the detection limit for that element. Some oxides seem to highlight the same situation previously outlined: samples C-B-Dol_002 and 007 are very similar, while the third one shows compositional features slightly different. For example, the percentage of Al_2O_3 is higher (1.57%) than for the other two samples (0.12% and 0.54%); the same for SiO_2 (3.13% against 0.03% of the first sample and 0.96% of the third one). Aluminium and silica, as well as iron and potassium, are the proof and confirmation of the presence of clay minerals. Anyway, x-ray fluorescence alone does not represent the principal technique for the purposes of this study, even if it is a good support to diffraction.

Table 5.12 *Results from X-ray Fluorescence on dolomite samples. On the left oxide percentages of the major elements. On the right trace elements expressed in ppm.*

%Ox	C-B-Dol		
	_002	_004	_007
SiO_2	0.03	3.13	0.96
TiO_2	0.01	0.08	0.02
Al_2O_3	0.12	1.57	0.54
Fe_2O_3	0.16	0.57	0.38
MnO	0.01	0.01	0.01
MgO	39.03	34.23	37.96
CaO	59.82	59.45	59.18
Na_2O	0.01	0.06	0.01
K_2O	0.01	0.21	0.10
P_2O_5	0.02	0.02	0.02
Tot	99.22	99.33	99.18
L.O.I.	42.01	44.97	43.70

ppm	C-B-Dol		
	_002	_004	_007
S	*134*	*979*	*105*
Sc	<5	<5	<5
V	<5	32	48
Cr	27	33	59
Co	<3	<3	<3
Ni	<3	12	17
Cu	34	34	35
Zn	19	24	25
Ga	<5	<5	<5
Rb	9	14	10
Sr	94	323	103
Y	<3	<3	<3
Zr	11	27	15

ppm	C-B-Dol		
	_002	_004	_007
Nb	<3	<3	<3
Ba	<10	42	25
La	<10	<10	<10
Ce	26	<10	12
Nd	29	20	39
Pb	<5	6	5
Th	45	40	38
U	10	22	5

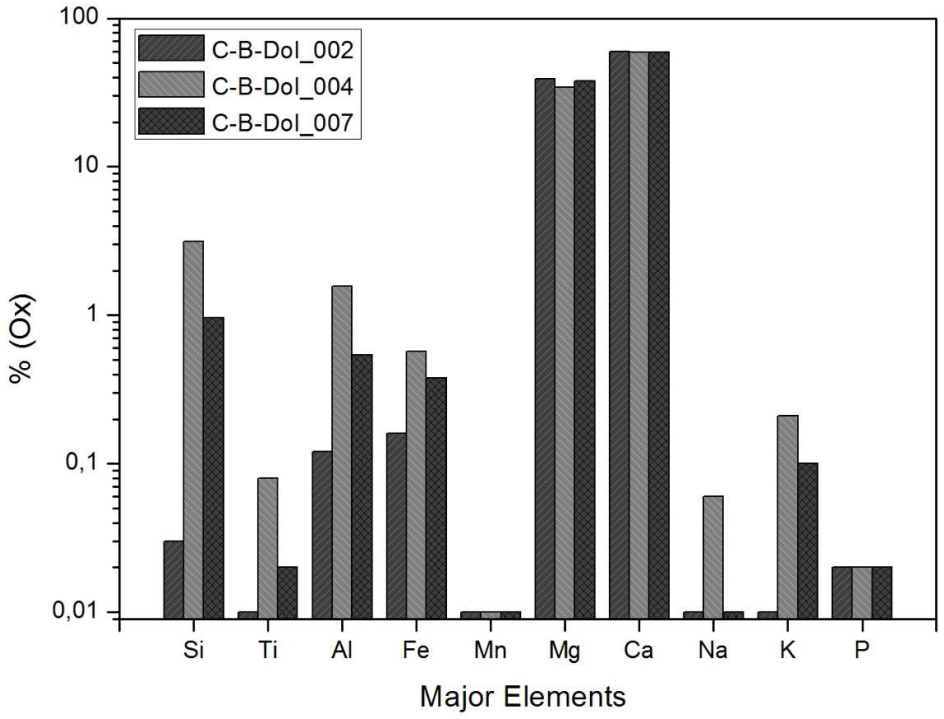

Figure 5.11 *Percentages (in oxides) of major elements for three samples of dolomite.*

- ***Trachytes***

The qualitative and semi-quantitative analysis through powder diffraction and Rietveld refinement on trachytes was more complicated with respect to dolomites. When a great number of mineral phases are present within a sample, several variables need to be considered:

- peaks of different phases overlap and it is difficult to understand every contributions;
- iso-orientation problems affect the intensities;
- crystallite size problems cause peak broadening.

Such issues are particularly relevant for feldspars, namely the main components of trachytes.

Diffractograms related to samples 1 (Monte Merlo) and 22B (Rocca Pendice) are reported in Figure 5.12. 20% of zinc oxide (ZnO) was used as internal standard. The blue profile corresponds to the real diffraction acquisition while the red one is the fitting profile obtained through refinement.

Sample 1 was composed by 26.20% of albite, 23.08% of anorthoclase, and 7.57% of sanidine; among mafic minerals, 0.41% of biotite, 0.22% of amphibole and 2.32% of augite are present. Furthermore, relevant amounts of accessory minerals are present, namely 9.21% of quartz, 1.18% of cristobalite, and 2.57% of magnetite. The amorphous component corresponds to 27.23% of the total composition. In this sample, a clay component is present, as testified by the peaks at low angles. The direct quantification of such phase was not possible because of broadening and overlapping of peaks, apart from the absence of reliable structural models. To solve this problem, it was assumed that samples 1 and 22B have about the same amorphous component since they come from the same geological area; the amorphous detected in sample 22B was taken from the amorphous of sample 1 and therefore the remaining percentage should correspond to the amount of clay minerals present in the sample (9.4%).

The composition of Rocca Pendice sample (22B) is different. The major phase is albite (38.56%), followed by anorthoclase (10.12%) and sanidine (14.31%) as remaining feldspars. Biotite (1.51%) and augite (2.79%) are the mafic components of the sample. Furthermore, quartz (8.26%), cristobalite (4.91%), and magnetite (1.71%) are present as accessory minerals.

Compositional analyses on Euganean Hills trachytes have been performed by several authors. Germinario (2016) conducted a specific study on trachytes from different quarries among which Monte Merlo, Monte Pendice and Rovarolla quarries. He made a preliminary petrographic characterization of the samples, carried out on separate thin sections under a polarizing microscope. Attribution to precise mineral phases was also confirmed by EMPA analyses, performed on all thin sections. Then, he obtained information on texture and rock-forming minerals from image analysis on micro-XRF maps. His study was a great reference for the mineralogical characterization of our samples. It was sure, for example, that in trachytes from Rocca Pendice there were neither plagioclases nor augites. Unfortunately, the same results were not obtained through X-ray diffraction.

Results from X-ray Fluorescence on trachyte samples are reported in Table 5.13. There are not relevant gaps between oxide compositions of the two samples and the interpretation of these data from a thermal point of view is very problematical. The main reason is the presence of a relevant number of mineral phases, some of them as solid solutions such as plagioclase.

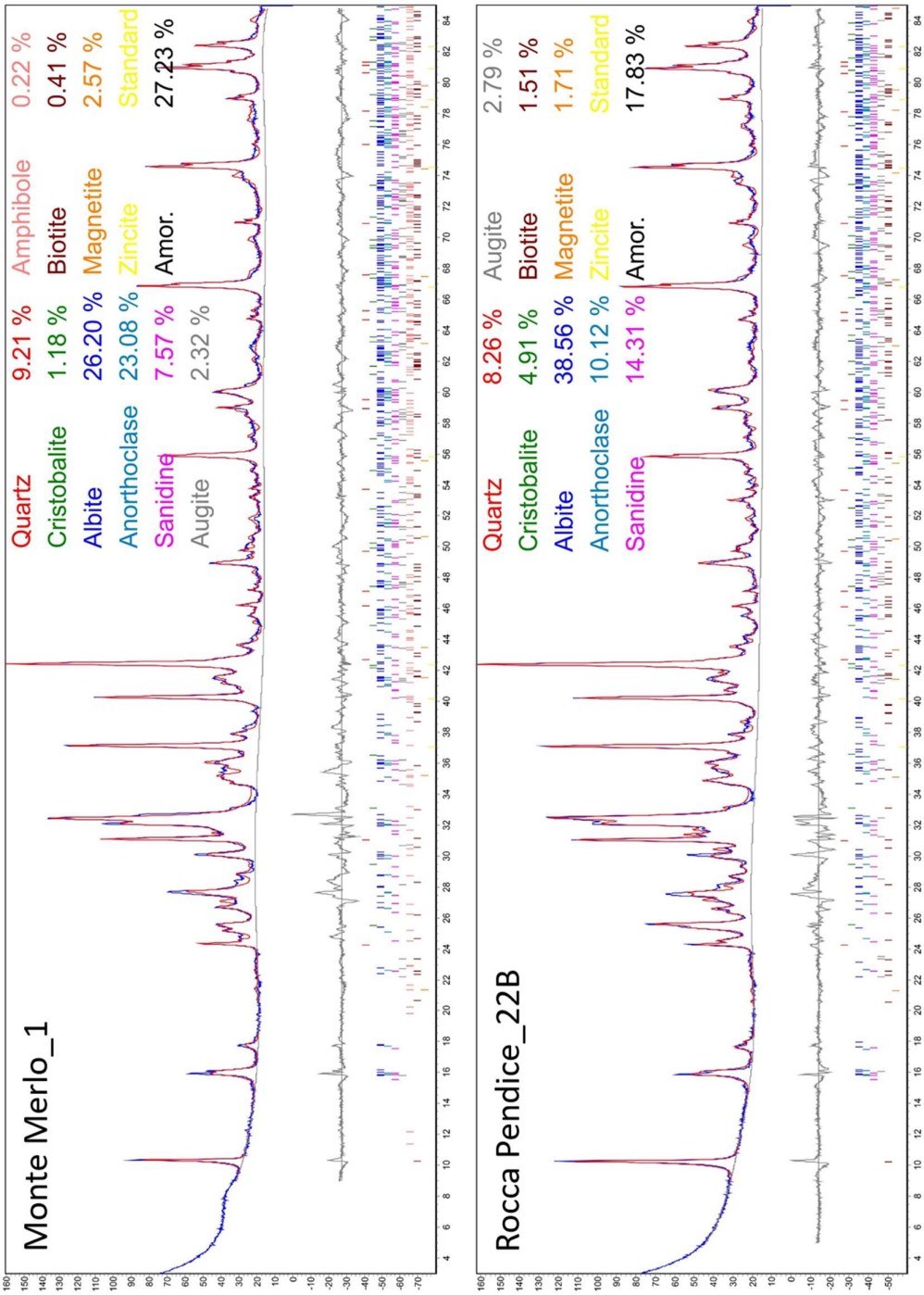

Figure 5.12 *Diffractograms of trachyte samples 1 (Monte Merlo) and 22B (Rocca Pendice) after Rietveld refinement with Topas software.*

Table 5.13 *Results from X-ray Fluorescence on trachyte samples. On the left oxide percentages of the major elements. On the right trace elements expressed in ppm.*

%Ox	1	22B
SiO_2	66.04	67.91
TiO_2	0.68	0.64
Al_2O_3	16.79	16.32
Fe_2O_3	3.54	2.97
MnO	0.08	0.04
MgO	0.71	0.63
CaO	1.58	1.11
Na_2O	5.09	4.75
K_2O	5.18	5.38
P_2O_5	0.29	0.17
Tot	99.98	99.92
L.O.I.	1.17	1.18

ppm	1	22B
S	*56*	*22*
Sc	6	12
V	27	18
Cr	<6	<6
Co	8	7
Ni	<3	<3
Cu	18	27
Zn	101	387
Ga	32	28
Rb	130	133
Sr	313	161
Y	22	27
Zr	559	591

ppm	1	22B
Nb	88	65
Ba	595	710
La	61	61
Ce	114	93
Nd	29	21
Pb	7	12
Th	27	18
U	11	10

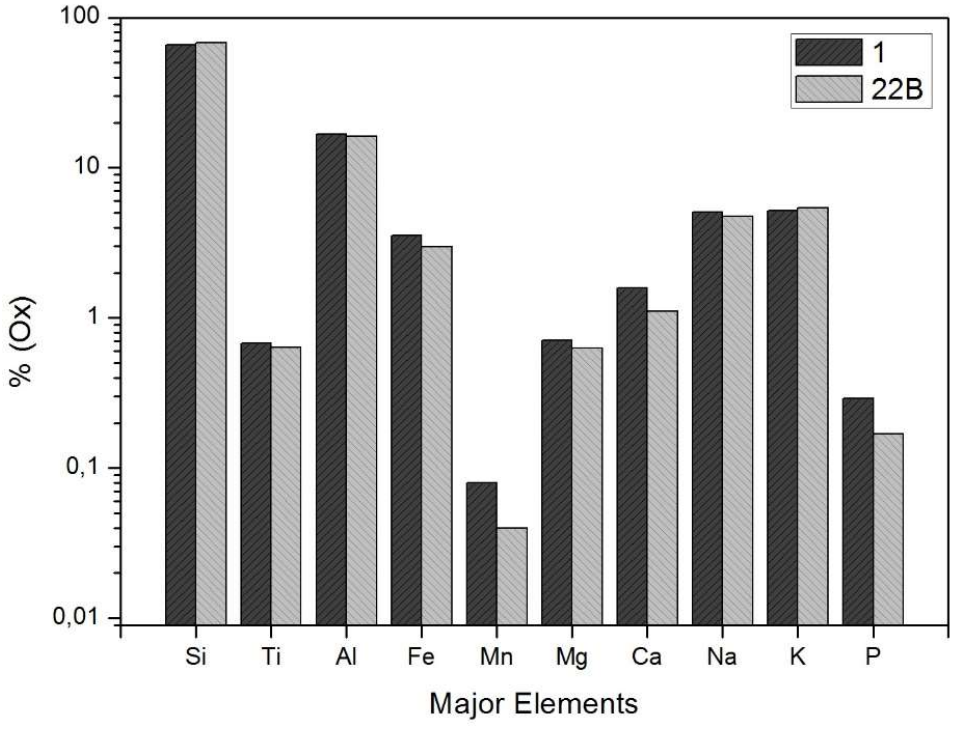

Figure 5.13 *Percentages (in oxides) of major elements for two samples of trachyte.*

5.5 Texture

A textural analysis by micro-XRF mapping was performed. The X-ray fluorescence emitted from the sample as a result of the X-ray excitation is captured by the detector, processed and translated into elemental information which is displayed for the user. For each sample the following elements were detected: Al, Ba, Ca, Fe, K, Mg, Mn, Na, P, Si, S, Sr, Ti, Zr.

- ***Dolomites***

Among the fourteen acquisitions (they are reported in Appendix A), the most significant maps for dolomites are reported in Figure 5.14: Ca, Fe, Mg, K, Si, TotCnt; Al map was also selected for sample C-B-Dol_004.

Ca and Mg maps are obviously helpful for the determination of the dolomite matrix that represent the framework of the rock. C-B-Dol_004 Ca map shows two green colours maybe due to the presence of two population of dolomite one of which rich in Ca. In the calcium map of sample C-B-Dol_007 a higher intensity can be identify in correspondence of fractures so it could represent calcite veins.

A difference in K maps between the first and third sample (lot of noise is present in the lower part of the image) respect to sample C-B-Dol_004 is clearly evident. This could be due to clay minerals already detected through X-ray diffraction. Potassium, aluminium and silica maps could be used together.

Another map that was though to be useful for quartz crystals detection was Si map. However, its interpretation was no simple because a contribution from the thin section glass might affect the intensities coming from Si-rich phases. To overcome this kind of problems, elemental maps analysis had always to be supported by optic microscope observations of thin sections. Unfortunately this was not possible with dolomite samples because thin sections were not available.

In conclusion, the creation of a classified image was not possible. For all the three sample it would have been a dolomite matrix with uncertain phases in between. The approach described in the following section for trachyte may not be the right one to follow for dolomites.

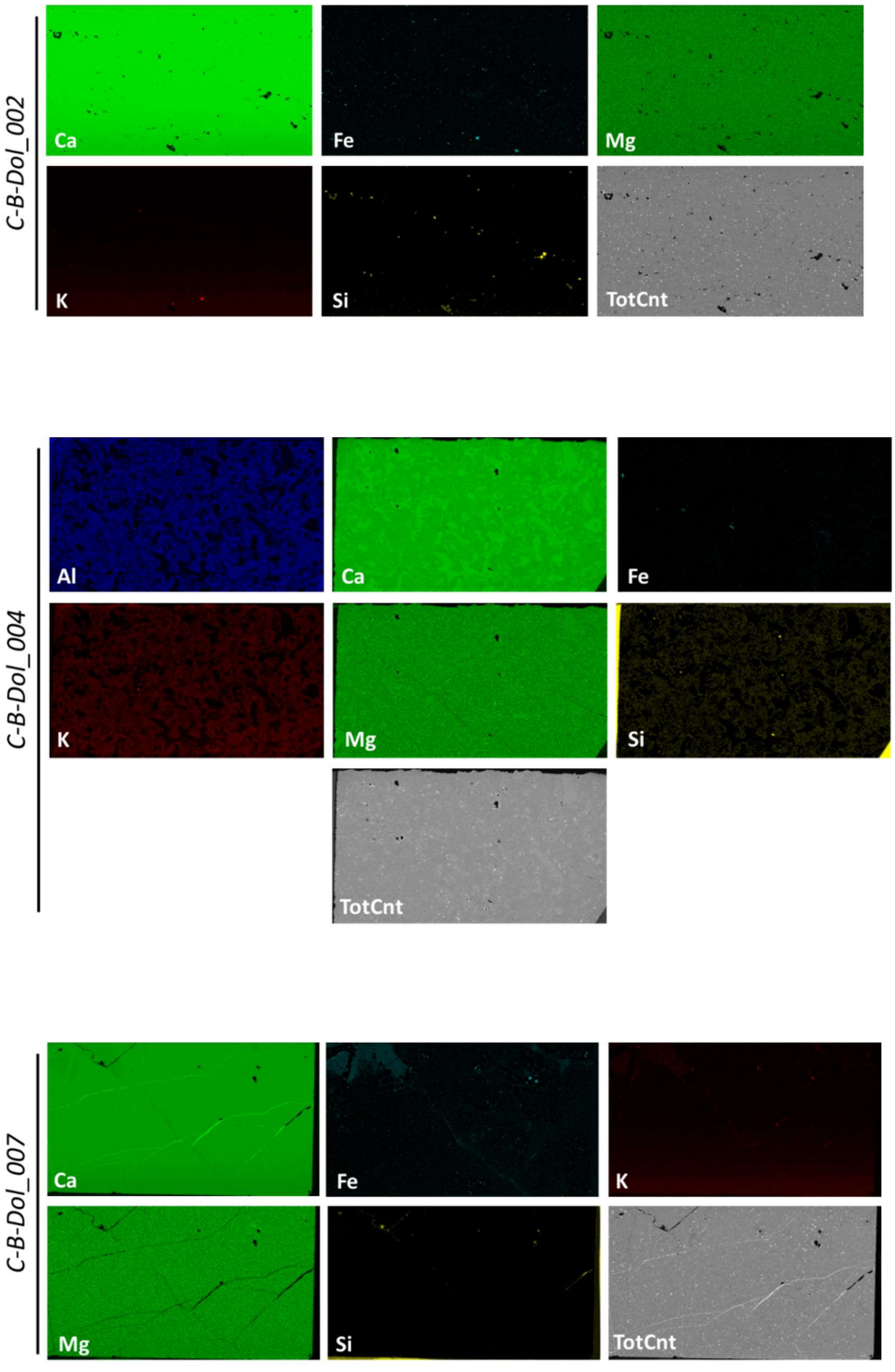

Figure 5.14 *X-ray elemental mapsof three dolomite samples.They were acquired in Torino with micro-XRF technique.*

- ***Trachytes***

Trachytes are classified as volcanic rocks but they actually show characteristics intermediate between intrusive and effusive rocks. The rapid extrusion of melted material (i.e., volcanos eruptions) causes the instantaneous cooling. Crystalline structures doesn't have time to develop and the resulting rock is characterize by glass. This is not the case of trachytes in which well developed feldspar phenocrysts, and biotite minerals are able to grow up. All these first observations can be made on hand samples (see Figure 5.15). The nucleation of crystals sites and the growth of crystals form of a porphyritic-glomero-porphyritic texture in which the main crystals are embedded in a fine groundmass of minerals. On several studies conducted on Euganean Hills trachytes no or little glass have been detected so they can be considered holocrystalline rocks.

After preliminary observations of hand samples, a more accurate petrographic characterization of the samples through a polarizing microscope is then recommended. This step allows to individuate the main mineral phases constituting phenocrysts and to characterize the matrix. Trachytes matrix is microcrystalline and composed by a felted free-glass mass of acicular or lath-shaped crystals. Seriate grain size can be observed.

The description and quantification of texture is a key topic in petrology. 2D methods have been developed for these purposes. Optical techniques provides very cost-effective transmitted-light photos taken on thin section with a polarizing microscope or image scanner, but resolution if often poor and, in most cases, image processing is slow and complex for rocks composed of many phases and crystals (Tarquini & Armienti, 2003; Tarquini & Favalli, 2010). Then there are electronic techniques. Some of them are based on scanning electron microscopy (SEM) or electron probe microanalysis (EMPA). X-ray maps are acquired on millimetric or sub-millimetric surfaces because acquisition may be extremely time-consuming.

After an accurate evaluation of the existing techniques, the micro-XRF seemed to perfectly fit the needs of the project. If mineralogy is a concern, X-ray maps are the most useful source of information, as they can also indirectly provide information on the modal composition of rocks much more quickly than manual point counting under the optical microscope (Maloy & Treiman, 2007, Germinario, 2016). If size and distribution size of phenocrysts are a concern,

classified images created through X-ray maps processing represent an easy tool for dimensional analyses. Another advantage in using this technique regards numerical modelling. A possible application will be discussed at the end of this section.

Among the fourteen maps, Figure 5.16 reports the most significant ones for trachyte samples: Al, Ca, Fe, K, Mg, P, Si, Ti, and total-count maps.

Differently from dolomites, micro-XRF on trachytes provided lot of information. They were superimposed and analysed as multispectral images, in which the various mineral phases were identified by their chemical composition.

Once all phases were identified, a false-colours image was created. Figure 5.17 represents a comparison between the classified images of samples 1, 22B, and LTR_13 (the latter is from Germinario's work under submission). Data regarding samples 1 and 22B refer to an area of investigation of $34.97 \times 20.08\ mm$ (a rectangle build on thin sections) while the other results refer to bigger areas of $5.30 \times 4.14\ cm$ (a rectangle on $7 \times 7 \times 1\ cm$ rock tiles). The legend assigning a colour to each phase applies to all images. Abbreviations for minerals are according to (Whitney and Evans, 2010): Ano, anorthoclase; Ap, apatite; Aug, augite; Bt, biotite; Crs, cristobalite; Ep, epidote; Ilm, ilmenite; Krs, kaersutite; Mag, magnetite; Pl, plagioclase; Qz, quartz; Sa, sanidine; Ttn, titanite; Zrn, zircon.

Classified images are characterized by three components: phenocrysts, pores, and groundmass. Pores were isolated and the images discussed in section 5.3 about porosity. Phenocrysts are all mineral phases that the software was able to detect and identify. A discrete grain, separated from the surrounding groundmass, is defined according to the values of spot size and resolution chosen for the analyses. The smallest discrete particle corresponds to a single pixel ($A_{pixel} = 68 \times 69\ \mu m = \sim 0.005\ mm^2$). Whatever under the detectability limit was classified as groundmass. In some cases a threshold can be provided and, among all the detected particles, only areas bigger than a specify size are going to be considered for textural considerations (see Germinario, 2014 where area values higher than $1 mm^2$ were considered). Anyway, when the field size is limited such an area threshold could mean the loss of a substantial part of data. For this reason, it was decided to consider all detected grains as phenocrysts useful for the textural and mineralogical evaluations.

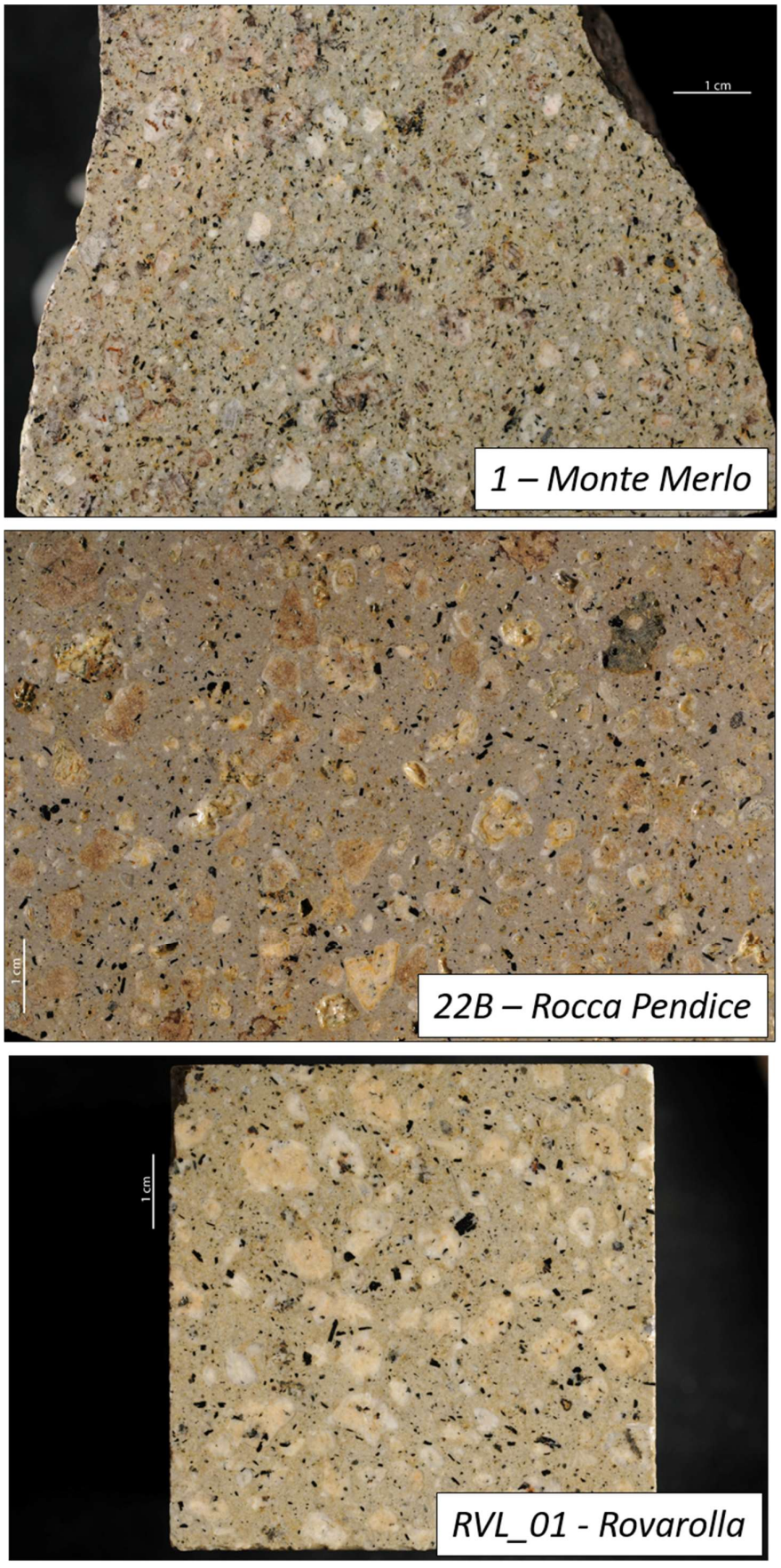

Figure 5.15 *Photos representing samples 1, 22B, and LTR_13. Surfaces treated with alcohol.*

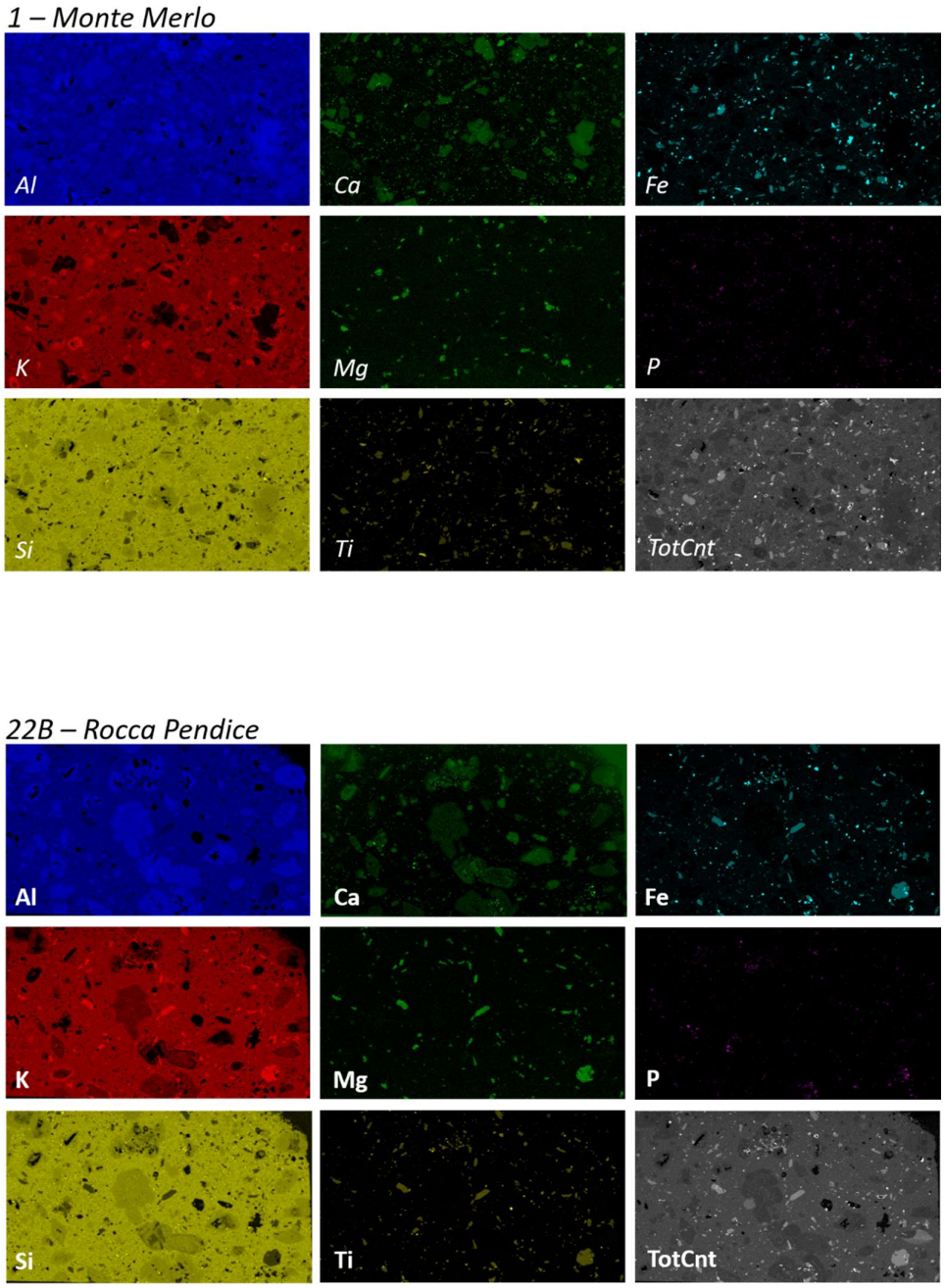

Figure 5.16 *The most significant elemental maps for the two sample of trachytes 1, above, and 22B, below. The TotCnt map records the total count of X-ray collected by the detector.*

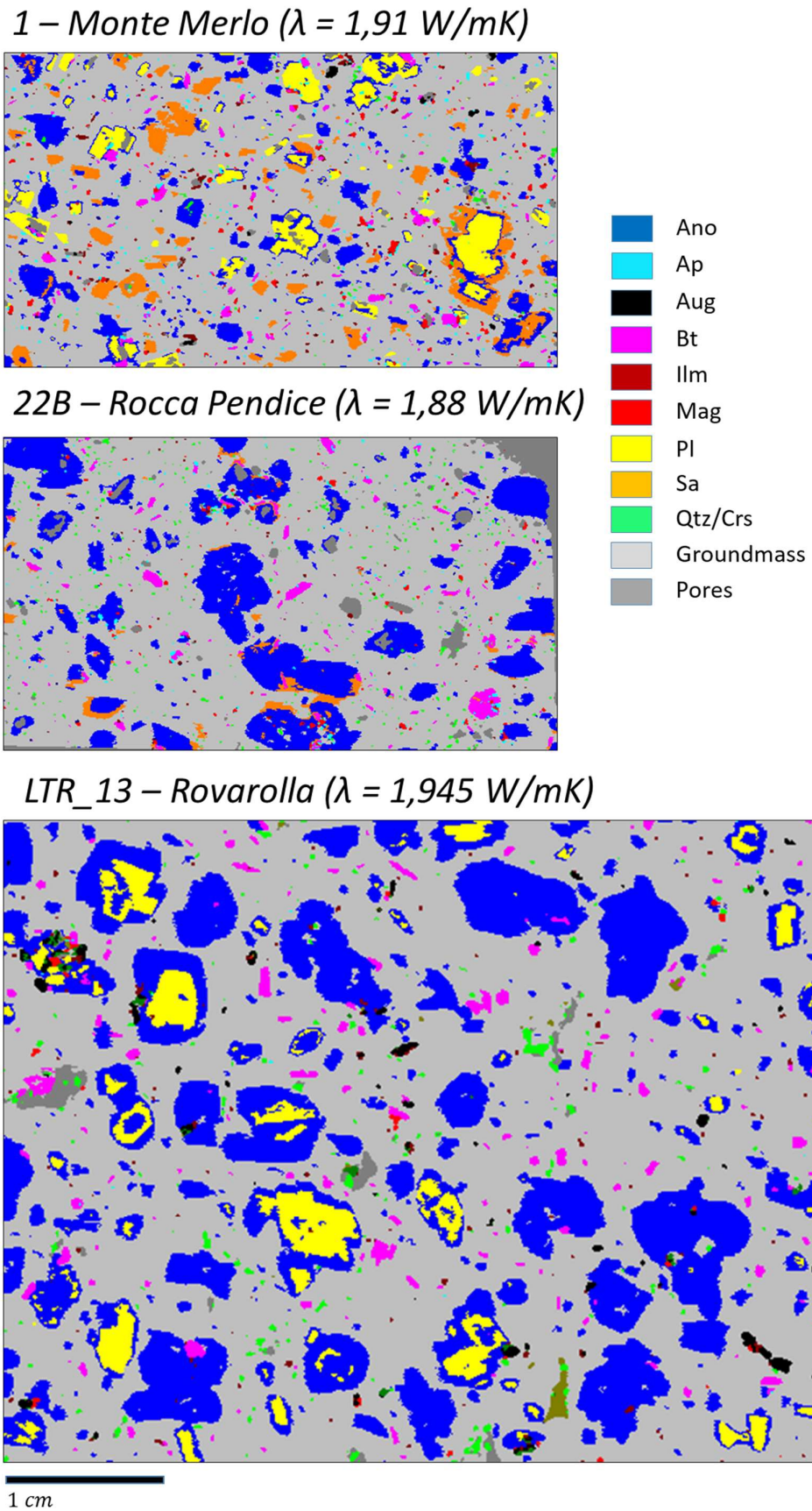

Figure 5.17 *Classified images of trachytes samples 1, 22B, and LTR_13 (from Germinario, under submission). Legend applies to all images.*

Table 5.14 *Percentage of mineral phases constituting phenocrysts, percentage of groundmass (GM) and porphyritic index (P.I., corresponding to percentage area of all phenocrysts) calculated after particle analysis. Abbreviation of minerals as in Table _. ∑ Fsp, total feldspars. Data referring to MRL-02, MRL-03, MRL-05, LTR-13 are from Germinario(2016).*

Quarry Locality	Sample	Feldspars				Mafic Minerals		
		Ano	Sa	Pl	∑ Fsp	Bt	Aug	Krs
Monte Merlo	MRL-02	14.52	0.65	6.88	22.05	2.15	0.04	0.03
	MRL-03	15.93	6.01	4.46	26.40	1.03	0.30	0.32
	MRL-05	19.42	0.96	5.47	25.85	1.11	0.69	0.37
	1	9.97	6.19	6.07	22.23	1.58	0.21	0.00
Rocca Pendice	22B	19.68	1.67	0.00	21.35	1.94	0.00	0.00
Zovon (Rovarolla)	LTR-13	25.47	0.00	4.16	29.63	1.58	0.62	0.00

Quarry Locality	Sample	Accessory Minerals					GM	P.I.
		Qz/Crs	Ilm	Mag	Ap	Others		
Monte Merlo	MRL-02	1.29	0.40	1.82	0.23	0.00	71.99	28.01
	MRL-03	0.23	0.31	0.75	0.05	0.00	70.59	29.41
	MRL-05	0.33	0.38	1.10	0.06	0.00	70.09	29.91
	1	0.41	0.68	0.91	0.46	0.00	71.71	28.29
Rocca Pendice	22B	1.00	0.17	0.49	0.45	0.00	72.07	27.93
Zovon (Rovarolla)	LTR-13	0.71	0.34	0.13	0.01	0.37	66.62	33.38

In order to improve the visual observations, these images were exploited for further processing where each class (biotite, ilmenite, groundmass, etc) was separated from the rest of components. Colour thresholding and particle analysis was performed on each final binary image separately (see Figures 5.18 for feldspars).

Table 5.14 reports the results of modal analysis. There are percentages of all identify mineral phases constituting phenocrysts (mode composition), the percentages of groundmass (GM) and the porphyritic index (percentage area of all phenocrysts; $P.I. = 100 - GM$) calculated after particle analysis. The percentages relative to MRL_02, MRL_03, MRL_05, and to LTR_13 was calculated by Germinario (2016).

Trachytes from Monte Merlo contains $22.05\ to\ 26.40\%$ of feldspars (Ano, Sa, Pl); Rocca Pendice sample contains 21.35% of feldspars (Ano, Sa); the sample from Zovon contains 29.63% of feldspars (Ano, Pl).

As regards mafic minerals, biotite show variability within samples from Mt. Merlo (1.03% in MRL_03 to 2.15% in MRL_02) but between the two analysed samples there is more biotite in sample 22B (1.94%) than in sample 1 (1.58%).

Feldspars represent the major component so the first step was to verify the variability of the thermal conductivity with feldspar content. As reported in section 5.1, thermal conductivity measurements were performed on samples from Mt. Merlo, Rocca Pendice and Zovon quarry. The latter has the higher λ ($1.94 - 1.95\ W/mK$), followed by sample 1 ($1.91\ W/mK$) and finally sample 22B ($1.88\ W/mK$). Looking at the percentages of feldspars, these thermal conductivity values seem to depend on feldspars contents (see Figure 5.18). This is not a surprising relationship. Trachytes show petrographic features intermediate between intrusive and effusive rocks. For volcanic rocks porosity is the controlling factor on thermal conductivity but the dominant phase (feldspar content) controls different conductivity distributions on plutonic rocks (Clauser and Huenges, 1995).

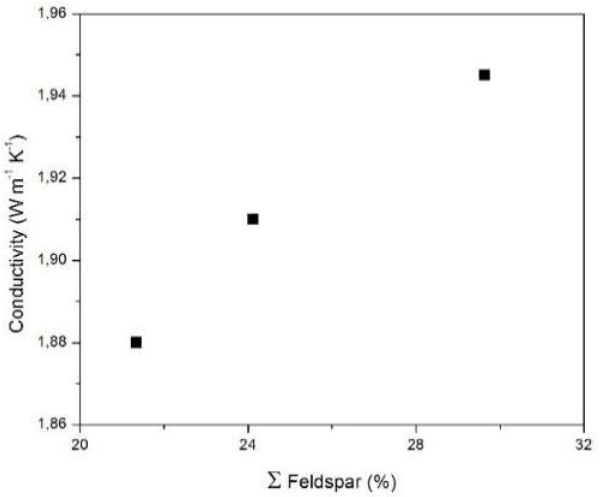

Figure 5.18 *Thermal conductivity variation with feldspar content for three sample of trachyte*

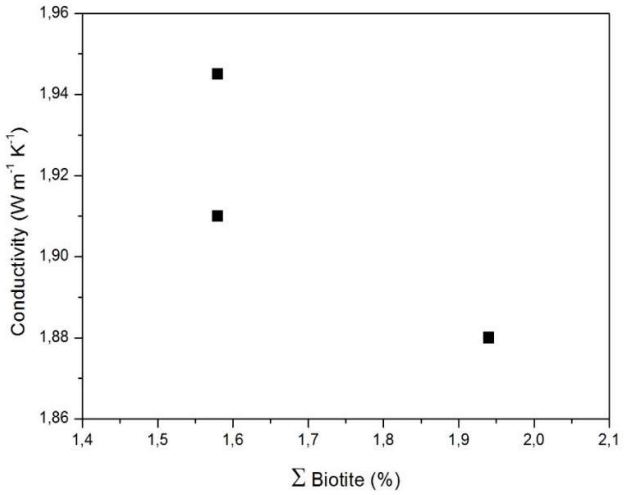

Figure 5.19 *Thermal conductivity variation with biotite content for three sample of trachyte.*

In addition to feldspars, biotites represent the other important mineral phase within trachytes. The influence of micas on thermal conductivity was investigated in Figure 5.19. It was expected the lowest conductivity in correspondence to the higher biotite content. This is true in fact sample from Rocca Pendice ($\lambda = 1.88\, W/mK$) contains 1.94% of biotite. However, the other two samples present the same biotite content but they have different conductivities.

The same investigation was made for quartz. It is one of the more conductive mineral but a clear dependence of thermal conductivity on quartz is not highlighted in Figure 5.20. On the contrary, sample with the higher quart content has the lower thermal conductivity. This is probably due to the very low concentration of quartz respect to that of feldspars within trachytes.

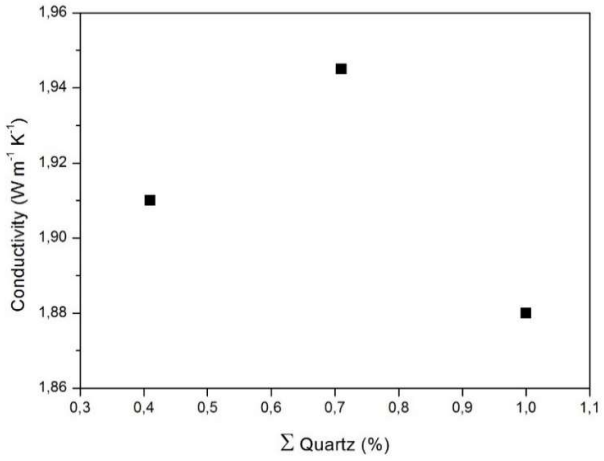

Figure 5.20 *Thermal conductivity variation with quartz content for three sample of trachyte.*

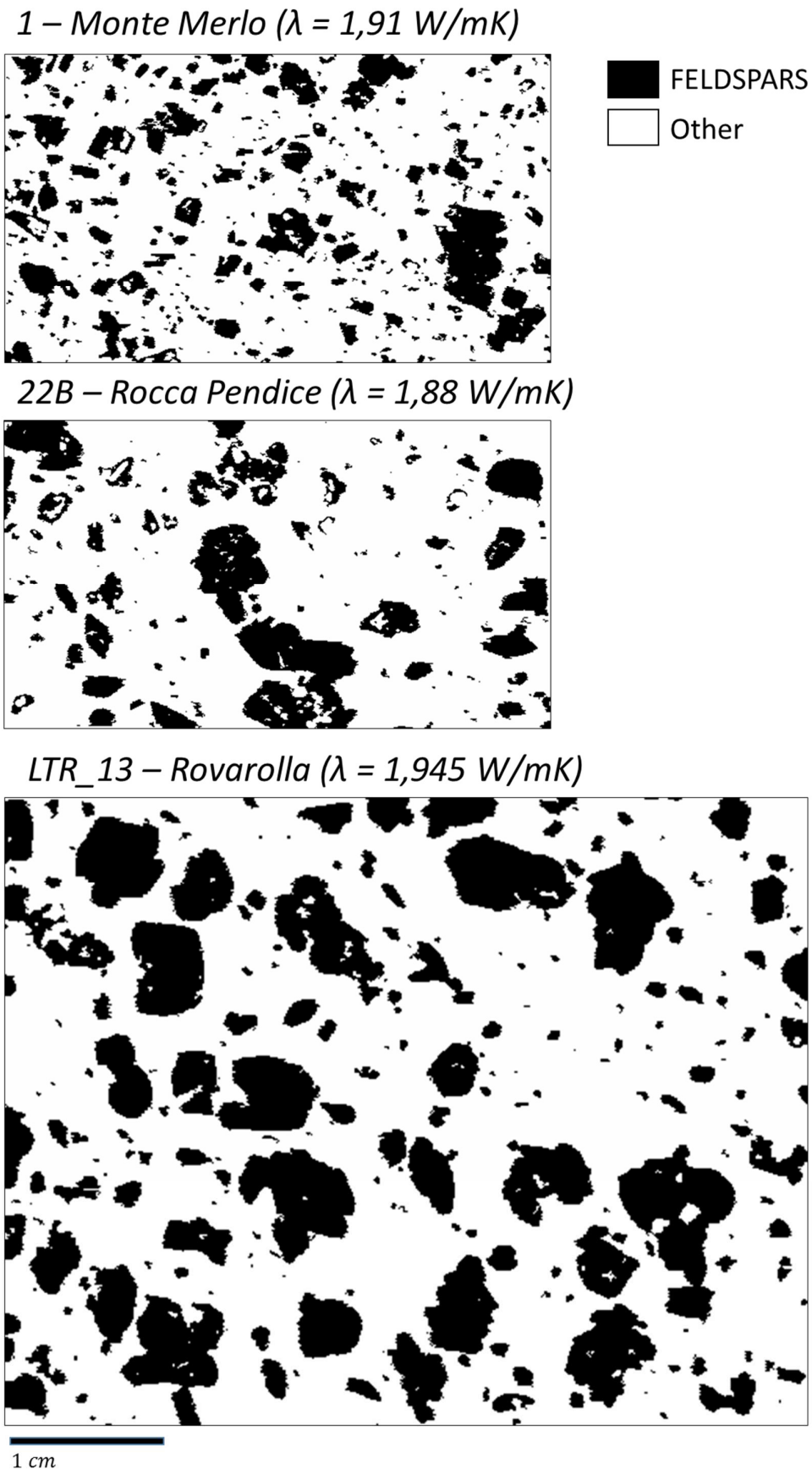

Figure 5.21 *Binary images of feldspar phenocrysts on trachyte sample 1, 22B, and LRT_13.*

Once the centrality of feldspars was ascertained, the following step was to examine their crystal-size distribution. Figure 5.21 reports binary images of feldspars on which textural analysis was made. The three phases anorthoclase, plagioclase and sanidine were considered together under the same class feldspars. Tables 5.15 and 5.16 reports the main textural data. The discussion will take into account samples 1, 22B and LTR_13 only, in this way it's easier to make comparisons with their reference images and also because thermal conductivity data refer to these samples specifically.

The Monte Merlo trachyte (sample 1) is characterized by fine to intermediate-grained feldspars, mainly under $30\ mm^2$: 82.86% of phenocrysts have $1\ to\ 5\ mm^2$ areas, 14.29% $5\ to\ 10\ mm^2$ areas, and 2.86% $10\ to\ 30\ mm^2$ areas. The maximum Feret diameter is of $8\ mm$ but the majority of feldspar phenocrysts have a Feret diameter less than $2\ mm$. The remaining grains (7.54%) have $2\ to\ 8\ mm$ Feret diameters.

Feldspars constituting Rocca Pendice trachyte (sample 22B) arrive to a maximum area of $32.43\ mm^2$ and maximum Feret diameters of $9.42\ mm$ but more than 95.65% of phenocrysts have $1\ to\ 5\ mm^2$ areas. The other two size classes are poorly represented: 2.17 % of feldspars has $5\ to\ 10\ mm^2$ areas, 1.45% has $10\ to\ 30\ mm^2$ areas, and 0.72% has $> 30\ mm^2$ areas.

Trachyte from Rovarolla quarry (LTR_13) contains the largest feldspars coming up to a maximum area of about $42\ mm^2$ and maximum Feret diameter of about $12\ mm$. Differently from the other two samples, the grain size is scattered over a rather broad range: 58.14% of phenocrysts has $1\ to\ 5\ mm^2$ areas, 22.09% has $5\ to\ 10\ mm^2$ areas, 17.44% has $10\ to\ 30\ mm^2$ and 2.33% of phenocrysts are over $30\ mm^2$.

Frequency histograms of crystal-size distribution with both Feret diameter (Figure 5.22) and area (Figure 5.23) of feldspars are reported. They are in log10 scale in order to better visualize the low percentages. Before any consideration it is important to precise that (1) the field size area is bigger for sample LTR_13, (2) the counts refer to 345 particles on sample 1, 138 particles on sample 22B, and on 221 particles on sample LTR_13, (3) the resolution was $68 \times 69\ \mu m$ for samples 1 and 22B and $103.5\ \mu m$ for sample LTR_13. It means that no accurate comparisons can be made looking at histograms only. Lot of other factors play an important role.

Table 5.15 *Textural data of feldspars (anorthoclase, plagioclase and sanidine considered together) relative to Feret diameters (mm). Field size:* $34.97 \times 20.08mm$. *MRL-02, MRL-03, MRL-05, LTR-13 data from Germinario (2016; under submission); they refers to a field size of* $5.30 \times 4.14cm$.

Quarry Locality	Sample	Feret diameter (mm)				
		Mean	Max	$d_{<2}$ (%)	d_{2-8} (%)	$d_{>8}$ (%)
Monte Merlo	MRL-02	0.85	6.15	90.63	9.37	0.00
	MRL-03	1.02	7.99	87.96	12.04	0.00
	MRL-05	1.31	9.69	84.72	15.15	0.13
	1	0.78	8.00	92.46	7.54	0.00
Rocca Pendice	22B	1.04	9.42	84.78	14.49	0.72
Zovon (Rovarolla)	LTR-13	1.54	11.92	78.67	19.60	1.73

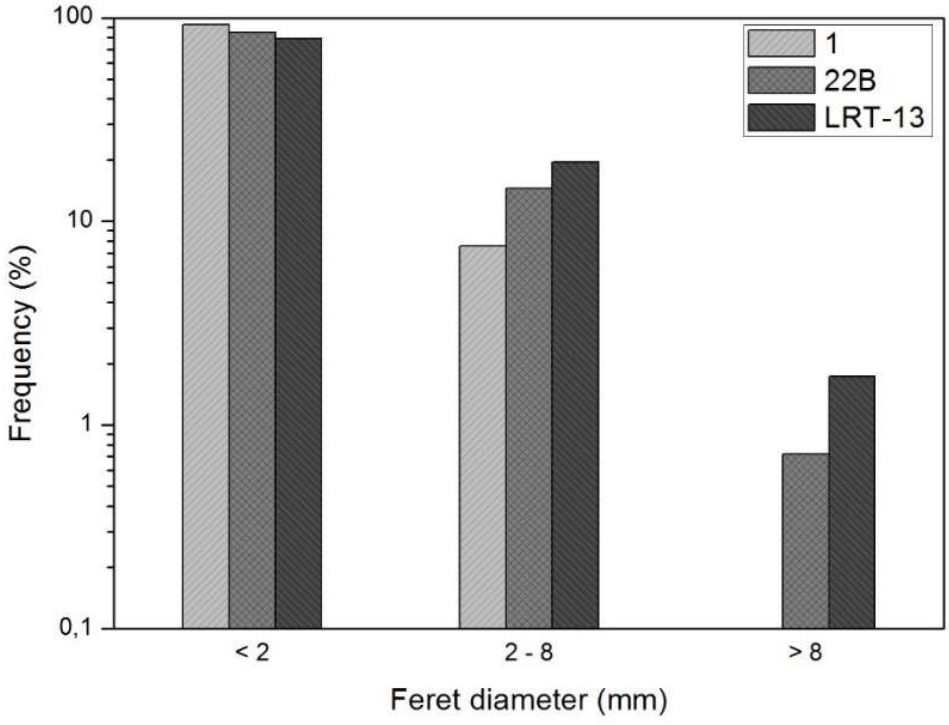

Figure 5.22 *Frequency histograms of crystal-size distribution of feldspars related to Feret diameters.*

Table 5.16 *Textural data of feldspars (anorthoclase, plagioclase and sanidine considered together) relative to areas (mm^2). Field size:* $34.97 \times 20.08mm$. *MRL-02, MRL-03, MRL-05, LTR-13 data from Germinario (2016; under submission); they refers to a field size of* $5.30 \times 4.14cm$.

Quarry Locality	Sample	Area (mm^2)					
		Mean	**Max**	a_{1-5} (%)	a_{5-10} (%)	a_{10-30} (%)	$a_{>30}$ (%)
Monte Merlo	MRL-02	0.41	15.37	85.05	12.15	2.80	0.00
	MRL-03	0.63	26.96	83.90	8.47	7.63	0.00
	MRL-05	0.83	34.94	80.34	13.68	5.13	0.85
	1	0.45	21.50	82.86	14.29	2.86	0.00
Rocca Pendice	22B	1.04	32.43	95.65	2.17	1.45	0.72
Zovon (Rovarolla)	LTR-13	1.87	42.61	58.14	22.09	17.44	2.33

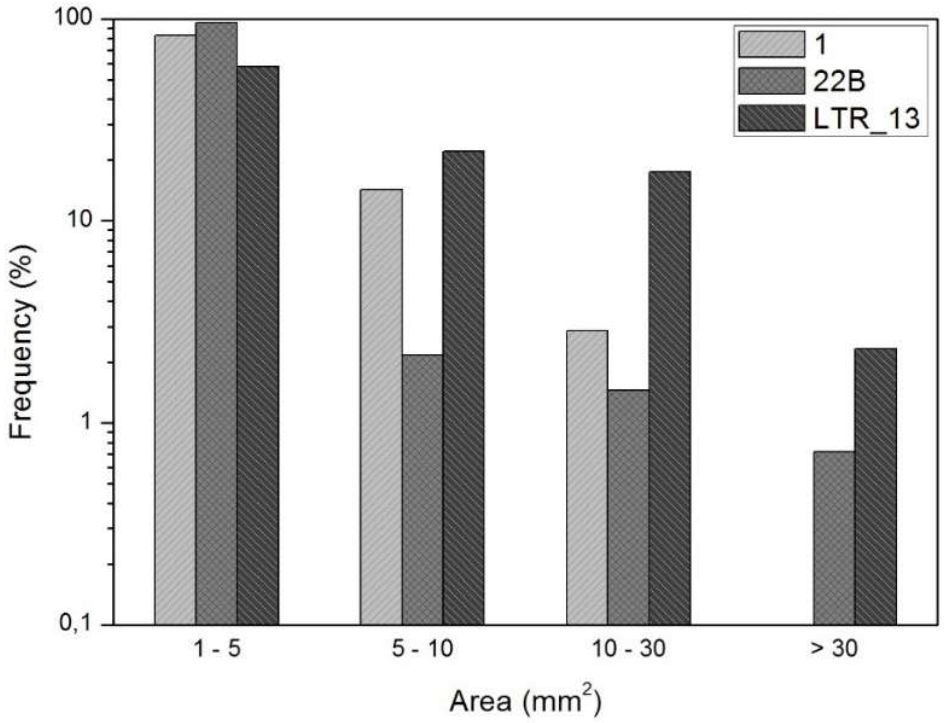

Figure 5.23 *Frequency histograms of crystal-size distribution of feldspars related to areas.*

As regards areas, a good agreement can be observed between thermal conductivity data and the frequencies, except for the range of areas bigger than $30\ mm^2$. In the range $1\ to\ 5$ the higher the number of particles, the lower the conductivity and viceversa. For ranged $5\ to\ 10$ and $10\ to\ 30$ the situation is opposite and sample LTR_13 that has the higher conductivity has more particles in those ranges of areas and viceversa for sample 22B. Sample 1 always represent the intermediate term. Feret diameters distribution seems to be a negligible factor in the thermal characterization of samples. For example, feldspars with the majority of phenocrysts with Feret diameter minor than 2 mm are those in sample 1 that is the sample with intermediate thermal conductivity.

Looking at both binary images and histograms it was tried to understand how a different distribution of the main mineral phase (feldspars) could differently affect the thermal conductivity. Among the first two samples the higher conductivity correspond to a higher P.I. (28.29% of sample 1 and 27.93% of sample 22B), a higher number of phenocrysts but smaller particles in mean. This means that a texture characterized by few big feldspars is less conductive than a texture characterized by a higher number of smaller crystals. The comparison with the sample from Zovon is complicated by the fact that the resolution is lower than that of the other two samples. Thus, particles under about $0.01\ mm^2$ are not detected (particles over about $0.005\ mm^2$ are detected in the other two cases). Anyway, it is clear that sample LTR_13 contains the larger feldspars phenocrysts. This factor added to the highest content make the sample the more conductive one.

So far, groundmass have not been taken into account but it is obviously a controlling factor like phenocrysts. The matrix represent the structure of the rock and as a continuum represents the basic mean for heat transport. Trachytes groundmass have been analysed and its composition is mainly characterized by feldspars. It is a microcrystalline matrix of alkaline feldspars, plagioclases sometimes, and sometimes Ca-rich feldspars. It was tried to quantify the glass component trough X-ray diffraction but no good results were reached. For now, the amorphous is considered as negligible for thermal characterization purposes on trachytes.

Micro-XRF technique was chosen because it can provide modal and textural information in the same time. Another advantage can be find in numerical modelling. Modelling software represent a fundamental resource in geothermal studies. For example, FeFlow provides Fem models of groundwater flow, contaminant, and heat transport simulations.

Modelling was beyond the scope of this thesis but it was an opportunity to test the efficiency of the micro-XRF. Thus, it was made a first attempt trying to compute the composite thermal conductivity of sample 22B from its mineralogical composition. Its classified image was converted into vector images in which each polygon (1532 polygons was created) corresponds to a mineral phase (Figure 5.24). The next step is to assign to each polygon its corresponding mineral phase and a thermal conductivity value to each phase. An average approach consists in taking rock-forming minerals values from tables in the literature. The challenge is to find the way to measure thermal conductivity of minerals because literature values are spread over wide ranges and mean values are too generic.

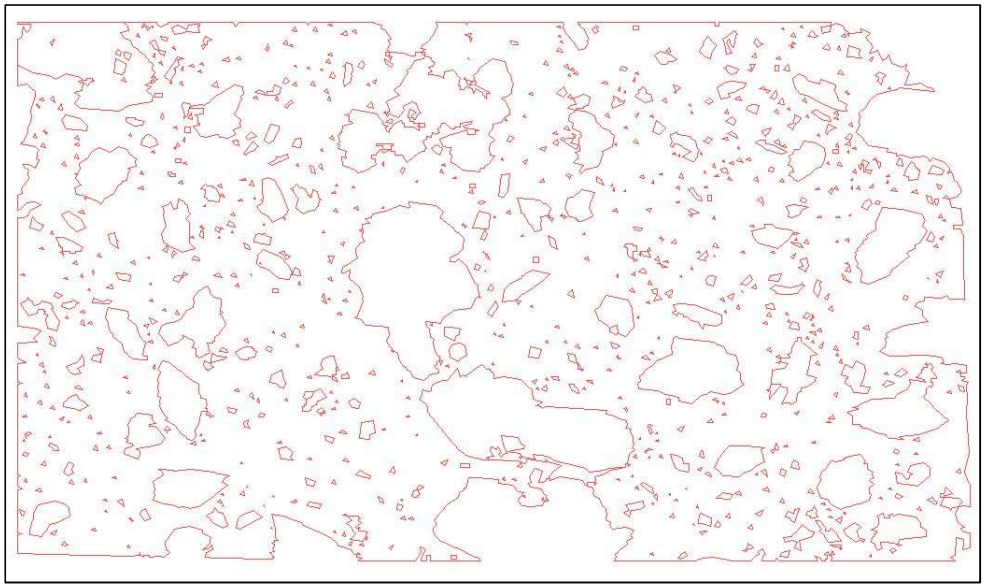

Figure 5.24 *Vector image created from classified image in Figure 5.17. Each polygon corresponds to a mineral grain.*

6 Conclusions

The present work is proposed as the first step in trying to fill the lack of knowledge in the field of thermal characterization of geological materials. A multiscale approach have been proposed. It was tested on two different lithologies, dolomites and trachytes, representing sedimentary and volcanic rocks respectively. The procedure comprehends a microscale characterization of the samples that so far has scarcely been taken into account studying thermal properties of geological materials. Two in particular are the tested techniques: the μ-XRF for the acquisition of quantitative mineralogical and textural information, and the He pycnometer as the most accurate technique for porosity measurements. Then, X-ray diffraction, X-ray fluorescence, image analysis were applied. The variability of thermal conductivity with all the measured parameters was studied.

The two main physical properties, namely density and porosity, are fundamental controlling factors on thermal conductivity for both sedimentary and volcanic rocks (Clauser and Huenges, 1995). The here presented results entirely confirm these statements for both dolomites and trachytes: the lower the density (the higher the porosity) the lower the thermal conductivity.

However, porosity is not enough to justify the variability in thermal conductivity values recorded among dolomite samples. This means that heat is transported almost entirely through the solid matrix skeleton. Consequently, the mineralogical component and its textural characteristics could determine the variation in conductivity. Anyway, X-ray diffraction and X-ray maps analysis do not provide the expected results for compositional and textural valuations. On one hand, single dolomite crystals cannot be discriminated because their size are under the detection limit of micro-XRF. On the other, it was not possible to have precise information about the real mineralogy of the dolomite constituting the

samples. The software indicated a Ca-rich dolomite but it could be a Mg-high calcite. They have different structures and symmetries and so they have different thermal conductivity according to lattice theory. Evidently, another approach had to be proposed for sedimentary rocks (dolomites and limestones) in the future. Other factors have to be considered such as the origin of the sediments, the calcite-dolomite ratio, the dolomite crystals size. Transmission electron microscopy (TEM) could be a possible analytical method for those purposes. As regards the variability that the lithology shows within the same outcrop (the dolomite sample have been collected from the same outcrop in Rio Maggiore mine), this represents a further complication. An accurate sampling is necessary for a correct characterization at the micro- and meso-scale.

Different the situation of trachytes. They show intermediate characteristic between intrusive and effusive rocks. As volcanic rocks, trachytes with higher porosity has the lower thermal conductivity. As plutonic rocks, the main mineral phase represent the controlling factor. The higher the feldspar content the higher the conductivity. As regards the determination of the mineralogical composition, X-ray diffraction and Rietveld refinement have proven to be inaccurate and the estimate of amorphous scarcely reproducible. Fortunately, the micro-XRF offers a reliable modal analysis that can be used for the characterization. Then, the most satisfying result regards the textural information that can be gained through the analysis of the elemental X-ray maps. Once all phases are identify and detected, any kind of texture information can be easily extracted from the classified image and the binary image of each mineral. The success with trachytes poses undoubted basis for the study of plutonic rocks.

The influence on thermal conductivity of the distribution of minerals have been observed in unconsolidated materials. A small percentage of homogeneously distributed graphite on a mixture sand-clay significantly changes the thermal conductivity of the mixture. It was looked for the same relationship on rocks. Three samples of trachytes were available and some considerations were made on them. Obviously a larger number of observations are necessary for a more reliable valuation of the texture influence on thermal conductivity.

A continuation and conclusion of the work started here has a potentially large impact on the future exploitation of energy resources and development of fundamental research and innovative solutions to detect the thermal properties

of rocks and unconsolidated sediments in the domains of geo-energy. Since this geo-energy domain is very broad, there is a great number of fields that can benefit from the results of the present research.

One of the main challenge is improving the understanding of shallow and deep geothermal reservoirs through the characterization of their thermal, hydrogeological and environmental properties (Di Sipio et al., 2013). The present research could contribute to the development of more efficient and safe shallow geothermal systems and to the reduction of the installation costs. A tested measurements protocol to be applied on hand samples in laboratory could be a more economic alternative to the GRT. This is the case, for example, of small residential houses where an elevated depth of the geothermal probes is not requested and few lithologies are crossed. A laboratory analysis of mineralogical content and petrographic texture could be sufficient for the elaboration of a geological model able to predict the thermal behaviour of the subsoil in that specific site under those specific conditions imposed by the geothermal system.

Not only geo-exchange systems, but also deep geothermal reservoir, could benefit from a similar study. Where elevated depths are necessary to reach the underground reservoirs, GRT cannot be performed. The only source of information may be a piece of the reservoir rock, or even worse, some minerals coming from there. The knowledge achieved through the present project (specially the part about single-mineral thermal characterization) could allow to use the compositional information of the mineral(s) and the spatial distribution of the phase(s), in order to hypothesize the geothermal features and the behaviour of the reservoir.

An other discussed theme is nowadays the energy storage. Great progresses have been made in the renewable energies field, starting from solar up to thermal energy, but the issue remains always the same: how to storage the excess energy in order to use it when the source (e.g. sun, wind, heat) is no more available. Thus, the challenge is to phase the energy source availability with the demand and to give the energy supply a continuity. To do that the thermal energy produced during the day must be accumulated in order to be used during the night, on a diurnal level, or, on a seasonal level, the energy accumulated during the summer must be stored for the winter. The subsoil is one of the most favourable place because of its thermal stability and because it has low dispersion compared with other means such as air. The questions are for

example: have the cycles of load and unload in the subsoil consequences such as micro-fracturing linked with expansion and contraction of the material? Which is the soil capacity to keep the heat in the site? Which are the consequences from a microstructurally point of view? Answers to this and other questions could be found with increasingly precise and accurate thermal characterizations. This is the reason why the study conducted for this thesis is a small step but very important for the comprehension of lithic materials thermal behaviour for more and more efficient applications in the future.

Some rocks are used in building trade for their thermal characteristics as insulators. A lithology is better than others but, as you learned from this thesis, the same lithology shows wide ranges of thermal properties values. The knowledge of the influence of the texture on the conductivity could guide toward more conscious choices of building stones.

The difficulties encountered during this work are the demonstration that the characterization of the thermal properties of rocks is a challenge still to be overcome.

Bibliography

Andrés, C., Álvarez, R., and Ordóñez, A. (2016). Estimation of thermal conductivity of rocks from their mineralogical composition (Asturian Coal Basin, NW Spain) for modelling purposes. Environ. Earth Sci. *75*.

Anovitz, L.M., and Cole, D.R. (2015). Characterization and Analysis of Porosity and Pore Structures. Rev. Mineral. Geochem. *80*, 61–164.

Bartoli, O., Meli, S., Sassi, R., and Magaraci, D. (2013). Amphiboles and clinopyroxenes from Euganean (NE Italy) cumulus enclaves: evidence of subduction-related melts below Adria microplate. Rendiconti Lincei *24*, 151–161.

Beck, A. (1957). A steady state method for the rapid measurement of the thermal conductivity of rocks. J. Sci. Instrum. *34*, 186.

Bertermann, D., Müller, J., Galgaro, A., Cultrera, M., Bernardi, A., and Di Sipio, E. (2016). Cheap-GSHPs, an European project aiming cost-reducing innovations for shallow geothermal installations.-Geological data reinterpretation. In EGU General Assembly Conference Abstracts, p. 13086.

Birch, F., and Clark, H. (1940). The Thermal Conductivity of rocks and its dependence upon temperature and composition. Am. J. Sci. *238*, 529–558.

Buggiarin, S. (2014). Thermophysical properties of Euganean Hills lithologies (Padua, North-Eastern Italy) related to underground thermal storage feasibility. Università degli studi di Padova.

Capedri, S., Venturelli, G., and Grandi, R. (2000). Euganean trachytes: discrimination of quarried sites by petrographic and chemical parameters and by magnetic susceptibility and its bearing on the provenance of stones of ancient artefacts. J. Cult. Herit. *1*, 341–364.

Clauser, C. (2011). Thermal Storage and Transport Properties of Rocks, II: Thermal Conductivity and Diffusivity. In Encyclopedia of Solid Earth Geophysics, H.K. Gupta, ed. (Springer Netherlands), pp. 1431–1448.

Clauser, C., and Huenges, E. (1995). Thermal conductivity of Rocks and Minerals. Am. Geophys. Union.

Cruciani, G. (2006). Introduction to powder diffraction. p.

De Lullo, A. (2016). Caratterizzazione termofisica del magazzino ipogeo per la frigoconservazione di Rio Maggiore (Val di Non - TN). Università degli studi di Padova.

Di Sipio, E., Chiesa, S., Destro, E., Galgaro, A., Giaretta, A., Gola, G., and Manzella, A. (2013). Rock Thermal Conductivity as Key Parameter for Geothermal Numerical Models. Energy Procedia *40*, 87–94.

Diment, W., and Pratt, H. (1988). Thermal conductivity of some rock-forming minerals: a tabulation (United State Department of the Interior Geological Survey).

Dove, M.T. (2011). Introduction to the theory of lattice dynamics. Éc. Thématique Société Fr. Neutron. *12*, 123–159.

Eppelbaum, L., Kutasov, I., and Pilchin, A. (2014). Thermal Properties of Rocks and Density of Fluids. In Applied Geothermics, (Berlin, Heidelberg: Springer Berlin Heidelberg), pp. 99–149.

Fuganti, A., Odorizzi, S., and Franzinelli, A. (2013). La miniera di Dolomia Rio Maggiore Val di Non (Trento).

Germinario, L., Cossio, R., Maritan, L., Borghi, A., and Mazzoli, C. (2016). Textural and Mineralogical Analysis of volcanic Rocks by μ-XRF Mapping. Microsc. Microanal.

Giesting, P.A., and Hofmeister, A.M. (2002). Thermal conductivity of disordered garnets from infrared spectroscopy. Phys. Rev. B *65*.

Gong, G. (2005). Physical properties of alpine rocks: a laboratory investigation. University of Geneva.

Gregg, J.M., Bish, D.L., Kaczmarek, S.E., and Machel, H.G. (2015). Mineralogy, nucleation and growth of dolomite in the laboratory and sedimentary environment: A review. Sedimentology *62*, 1749–1769.

Gustafsson, S.E. (1991). Transient plane source techniques for thermal conductivity and thermal diffusivity measurements of solid materials. Rev. Sci. Instrum. *62*, 797.

Höfer, M., and Schilling, F.R. (2002). Heat transfer in quartz, orthoclase, and sanidine at elevated temperature. Phys. Chem. Miner. *29*, 571–584.

Hofmeister, A.M. (2001). Thermal conductivity of spinels and olivines from vibrational spectroscopy: Ambient conditions. Am. Mineral. *86*, 1188–1208.

Hofmeister, A.M. (2006). Thermal diffusivity of garnets at high temperature. Phys. Chem. Miner. *33*, 45–62.

Hofmeister, A.M. (2014). Thermal diffusivity and thermal conductivity of single-crystal MgO and Al2O3 and related compounds as a function of temperature. Phys. Chem. Miner. *41*, 361–371.

Hofmeister, A.M., and Pertermann, M. (2008). Thermal diffusivity of clinopyroxenes at elevated temperature. Eur. J. Mineral. *20*, 537–549.

Horai, K.-I. (1971). Thermal Conductivity of Rock-Forming Minerals. J. Geophys. Res. *76*.

Maritan, L., Mazzoli, C., Sassi, R., Speranza, F., Zanco, A., and Zanovello, P. (2013). Trachyte from the Roman aqueducts of Padua and Este (north-east Italy): a provenance study based on petrography, chemistry and magnetic susceptibility. Eur. J. Mineral. *25*, 415–427.

Mathis, N. (2000). Transient thermal conductivity measurements: comparison of destructive and nondestructive techniques. High Temp.-High Press. *32*, 321–327.

Min, S., Blumm, J., and Lindemann, A. (2007). A new laser flash system for measurement of the thermophysical properties. Thermochim. Acta *455*, 46–49.

Pasquale, V., Verdoya, M., and Chiozzi, P. (2014). Geothermics. Heat Flow in the Lithosphere (Springer).

Popov, Y., Bayuk, I., Parshin, A., Miklashevskiy, D., Novikov, S., and Chekhonin, E. (2012). New methods and instruments for determination of reservoir thermal properties. In Proceedings, Thirty-Seventh Workshop on Geothermal Reservoir Engineering Stanford University, Stanford, California, p.

Popov, Y.A., Pribnow, D.F.C., Sass, J.H., Williams, C.F., and Burkhardt, H. (1999). Characterization of thermal properties by high-resolution optical scanning. Geothermics *28*, 253–276.

Quaschning, V. (2005). Understanding renewable energy systems (London ; Sterling, VA: Earthscan).

Robertson, E.C. (1988). Thermal Properties of Rocks (Reston: U.S. Geol. Survey).

Rollinson, H. (1993). Using Geochemical Data: Evaluation, Presentation, Interpretation.

Sass, J.H. (1965). The thermal conductivity of fifteen feldspar specimens. J. Geophys. Res. *70*.

Sassi, R. (2004). Towards a Better Understanding of the Fibrolite Problem: the Effect of Reaction Overstepping and Surface Energy Anisotropy. J. Petrol. *45*, 1467–1479.

Schön, J. (2011). Physical properties of rocks: a workbook (Amsterdam ; Boston: Elsevier).

Somerton, W.H. (1992). Thermal Properties and Temperature-Related Behavior of Rock/Fluid Systems (Elsevier).

Vaggelli, G., and Cossio, R. (2012). μ-XRF analysis of glasses: a non-destructive utility for cultural heritage applications. The Analyst *137*, 662–667.

Von Herzen, R., and Maxwell, A.E. (1959). The Measurement of Thermal Conductivity of Deep-Sea Sediments by a Needle-Probe Method. J. Geophys. Res. *64*.

Whitney, and Evans (2010). Abbreviations for names of rock-forming minerals. Am. Mineral. *95*, 185–187.

AccuPyc 1330 Pycnometer Operator's Manual

Websites:

www.cheap-gshp.eu

www.gemmarium.it

www.struers.com

www.edax.com

www.speciation.net

Appendix A

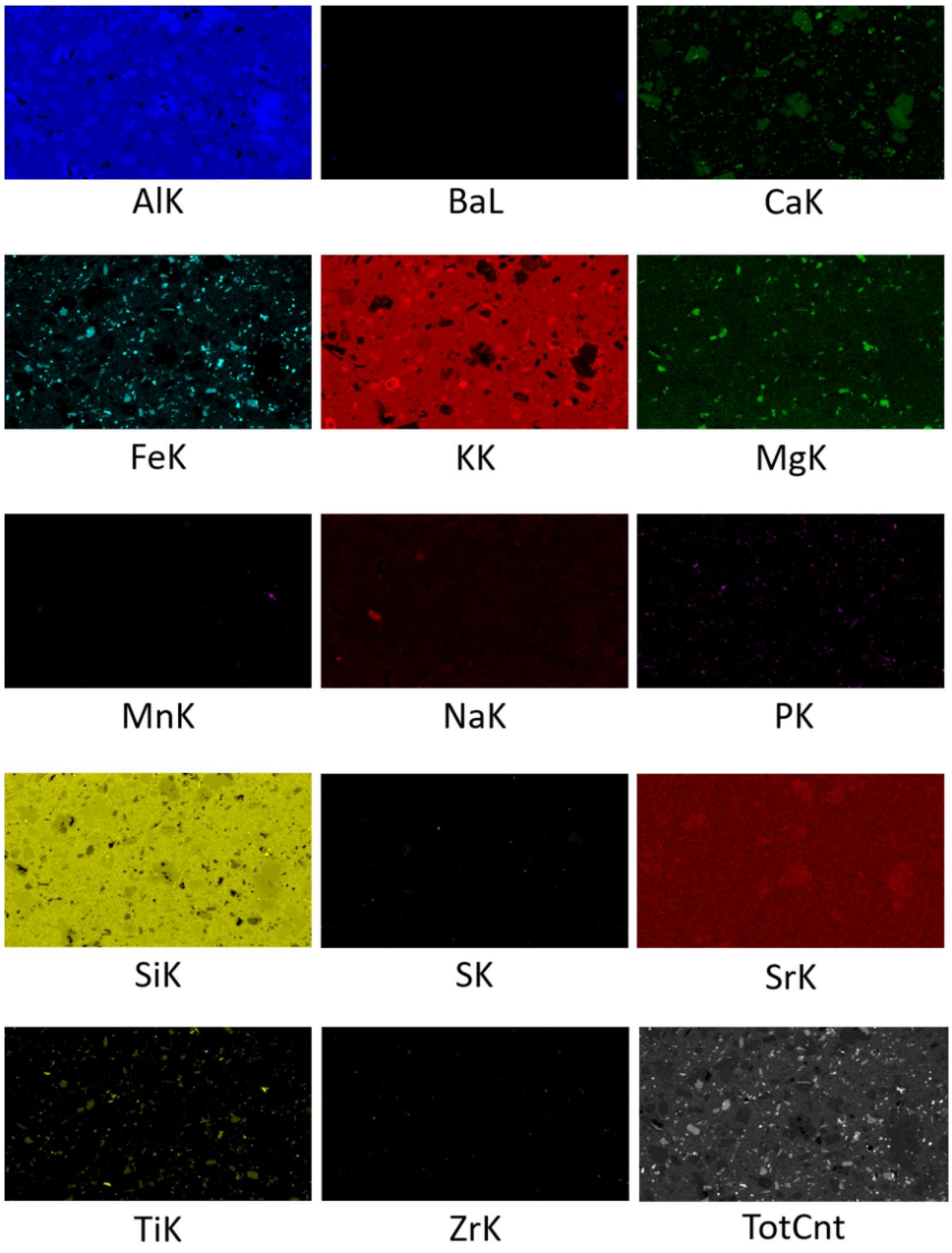

Micro-XRF elemental maps of sample 1 (trachyte).

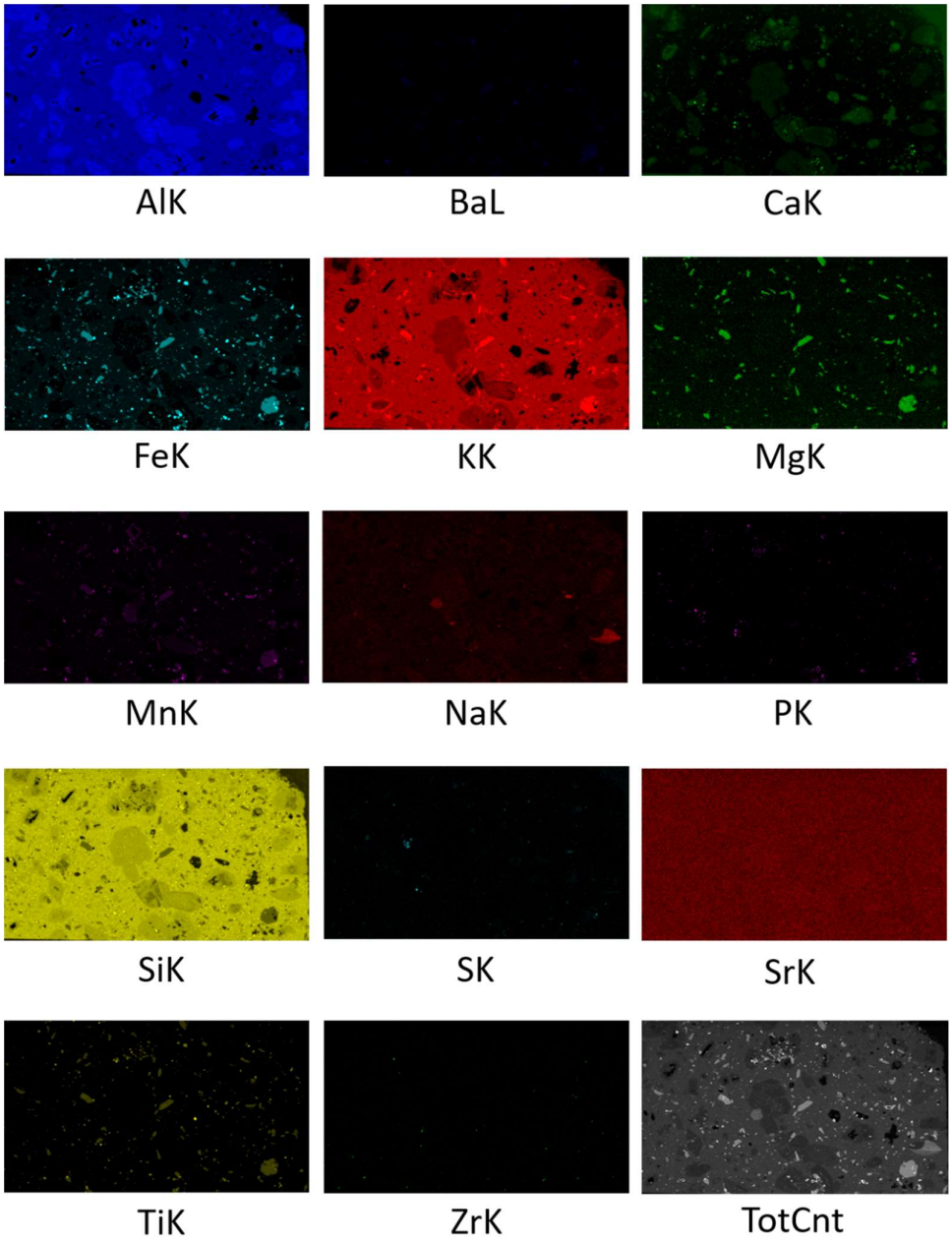

Micro-XRF elemental maps of sample 22B (trachyte).

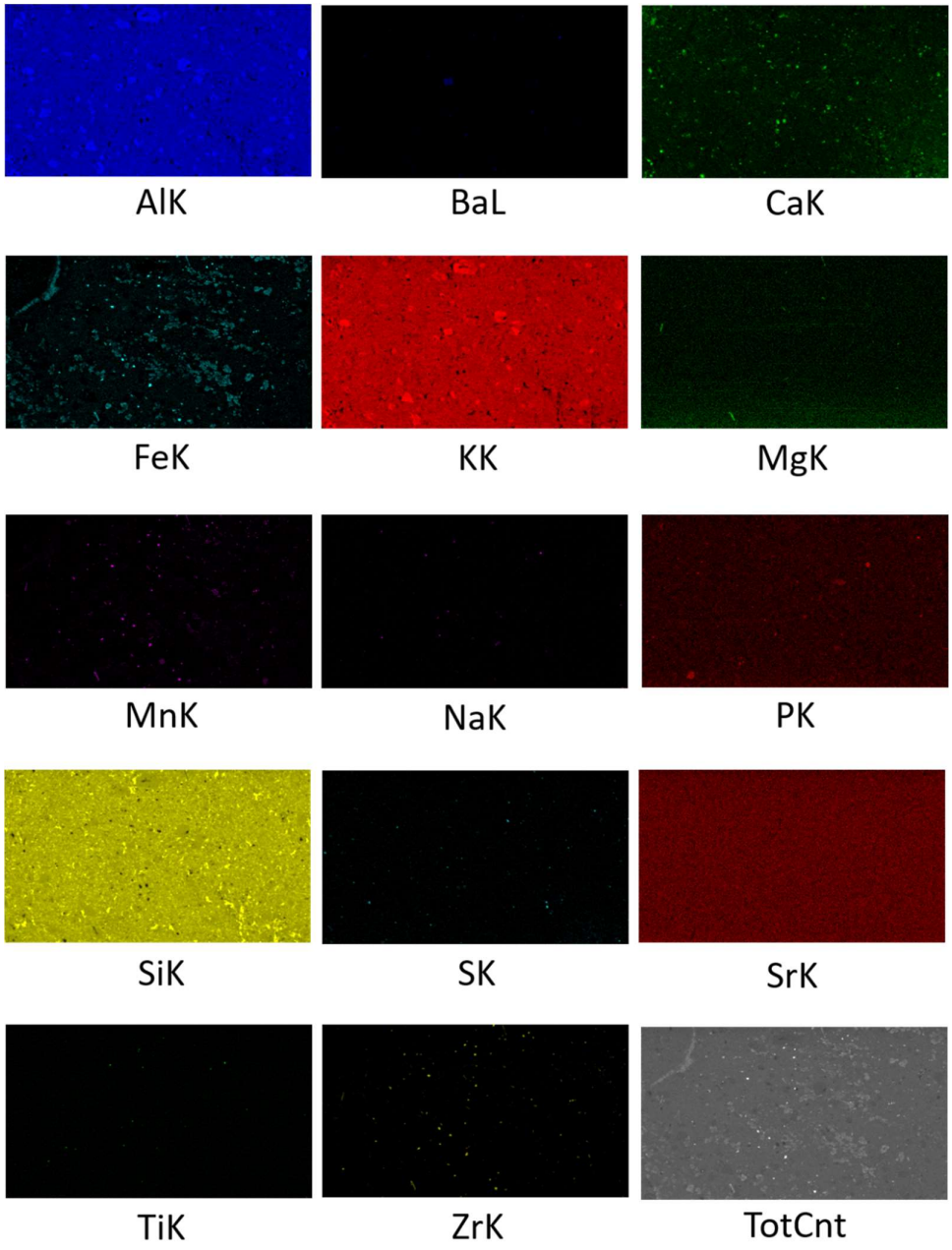

Micro-XRF elemental maps of sample 16 (rhyolite).

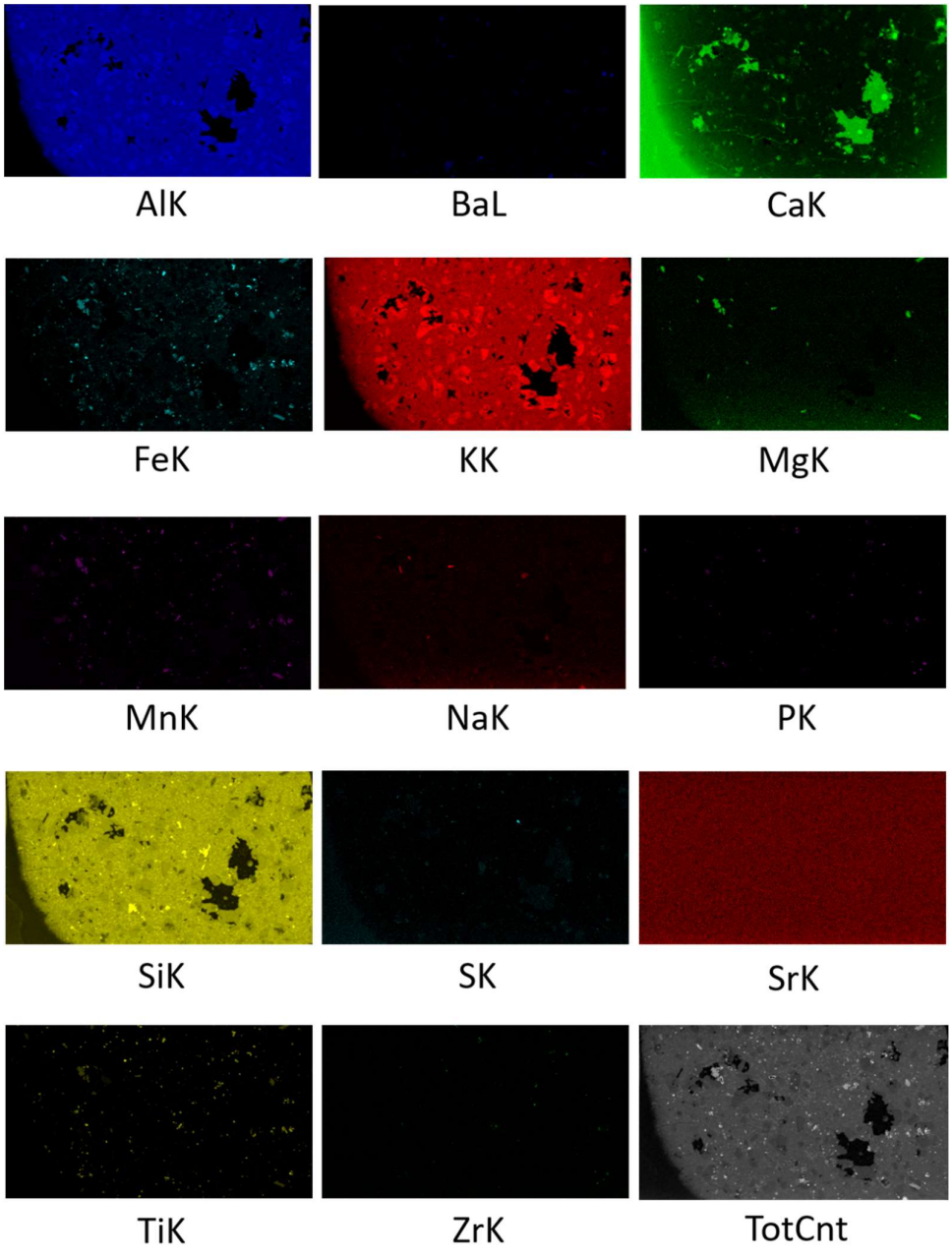

Micro-XRF elemental maps of sample 39 (rhyolite).

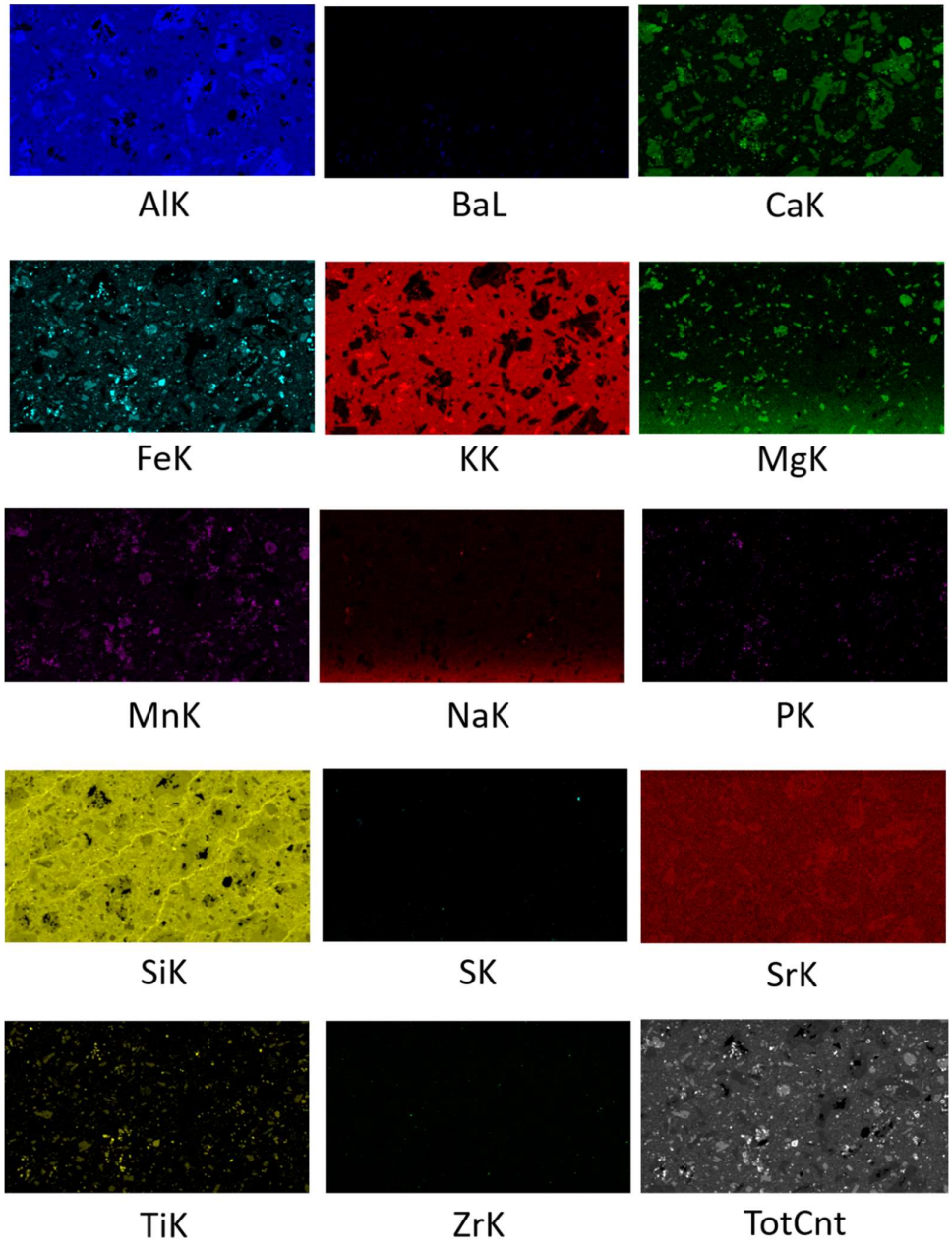

Micro-XRF elemental maps of sample 42 (latite).

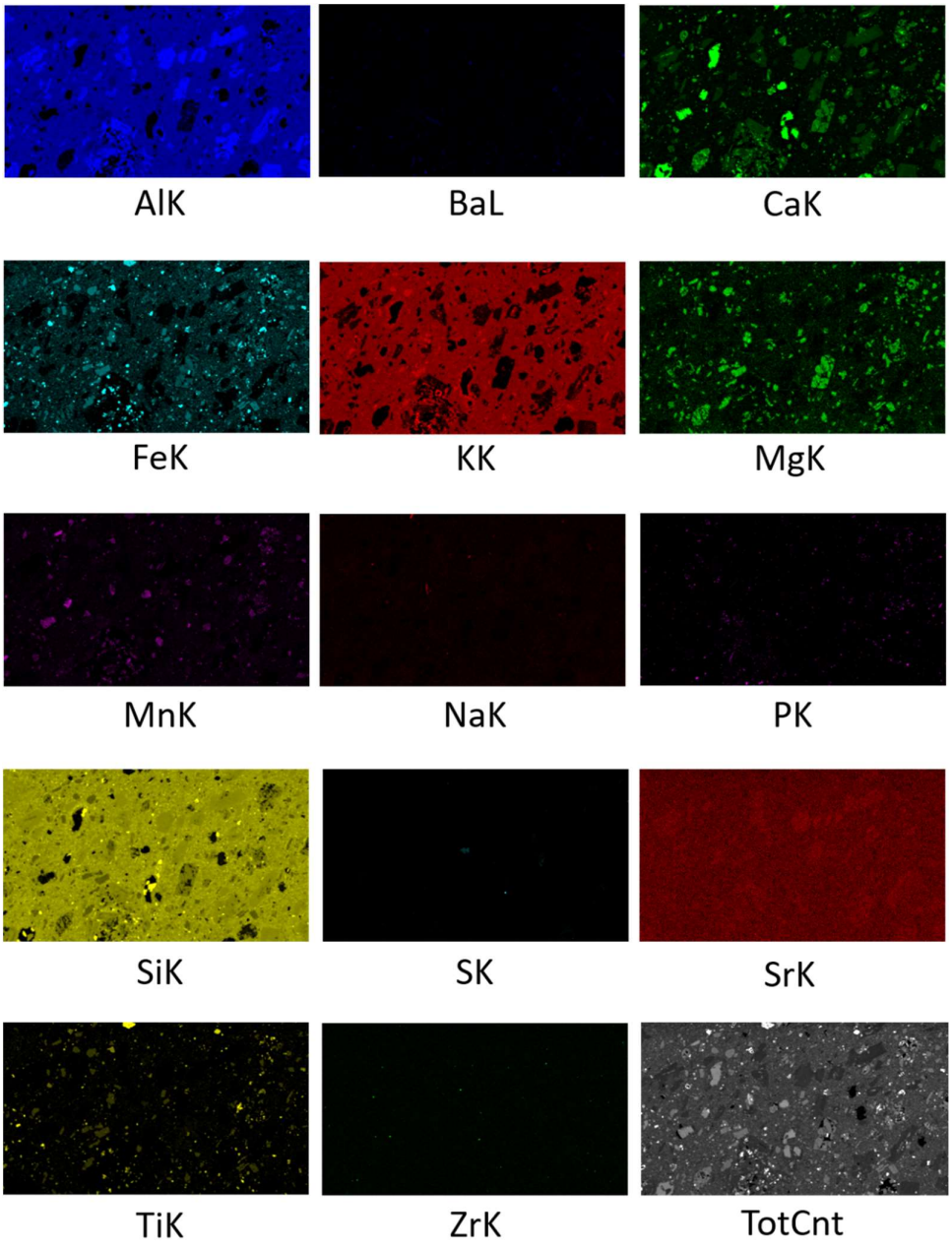

Micro-XRF elemental maps of sample 43 (latite).

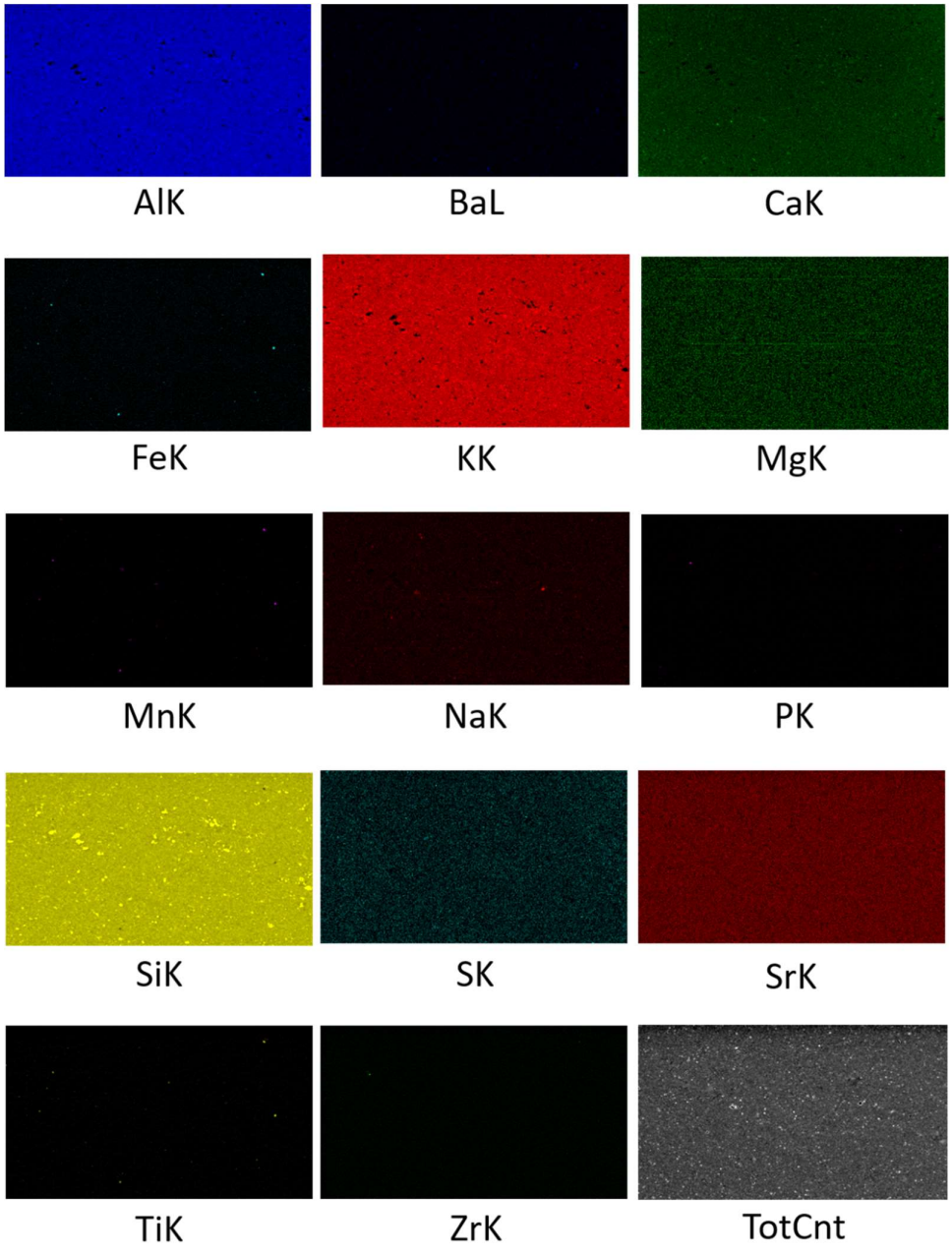

Micro-XRF elemental maps of sample 11 (marl).

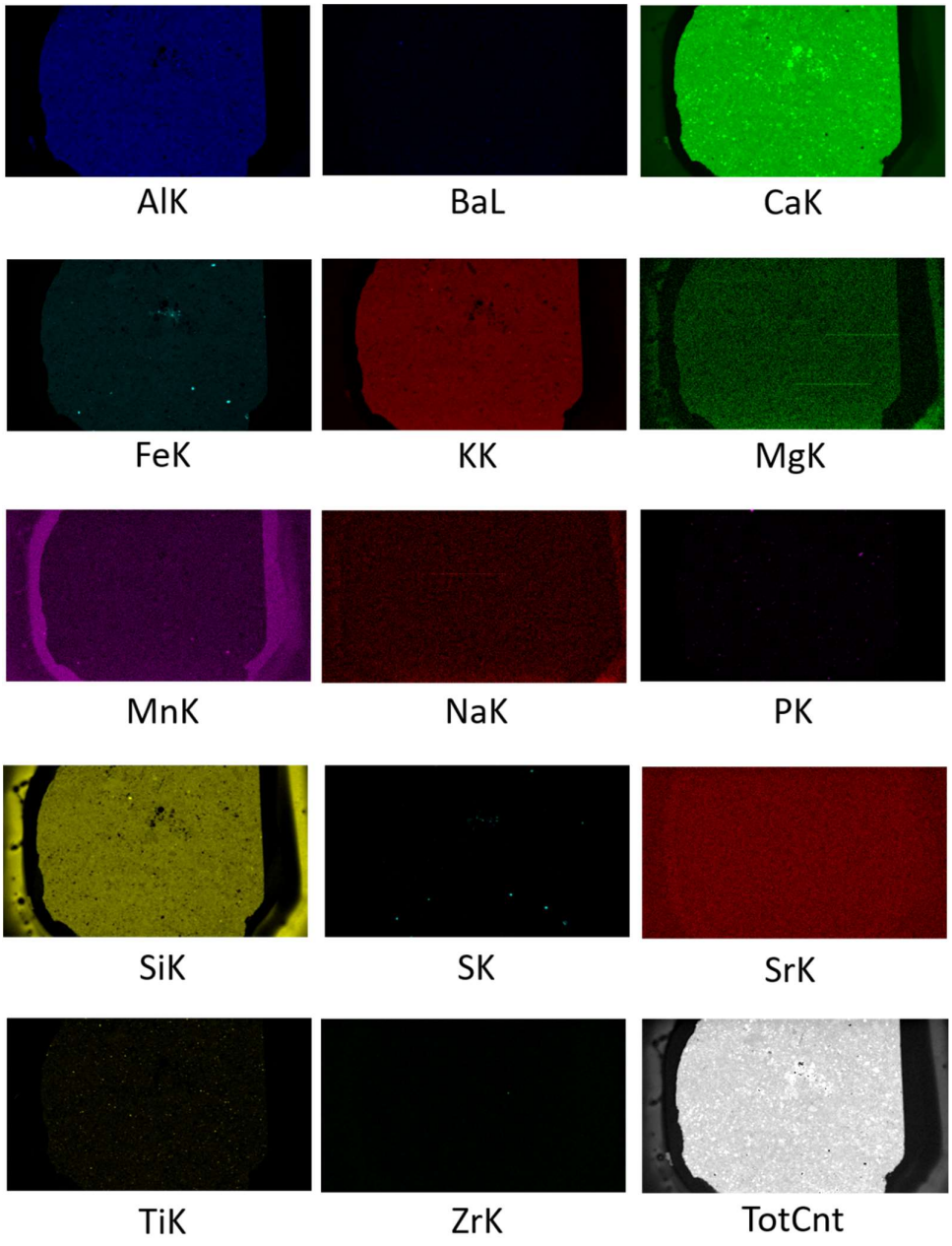

Micro-XRF elemental maps of sample 24 (marl).

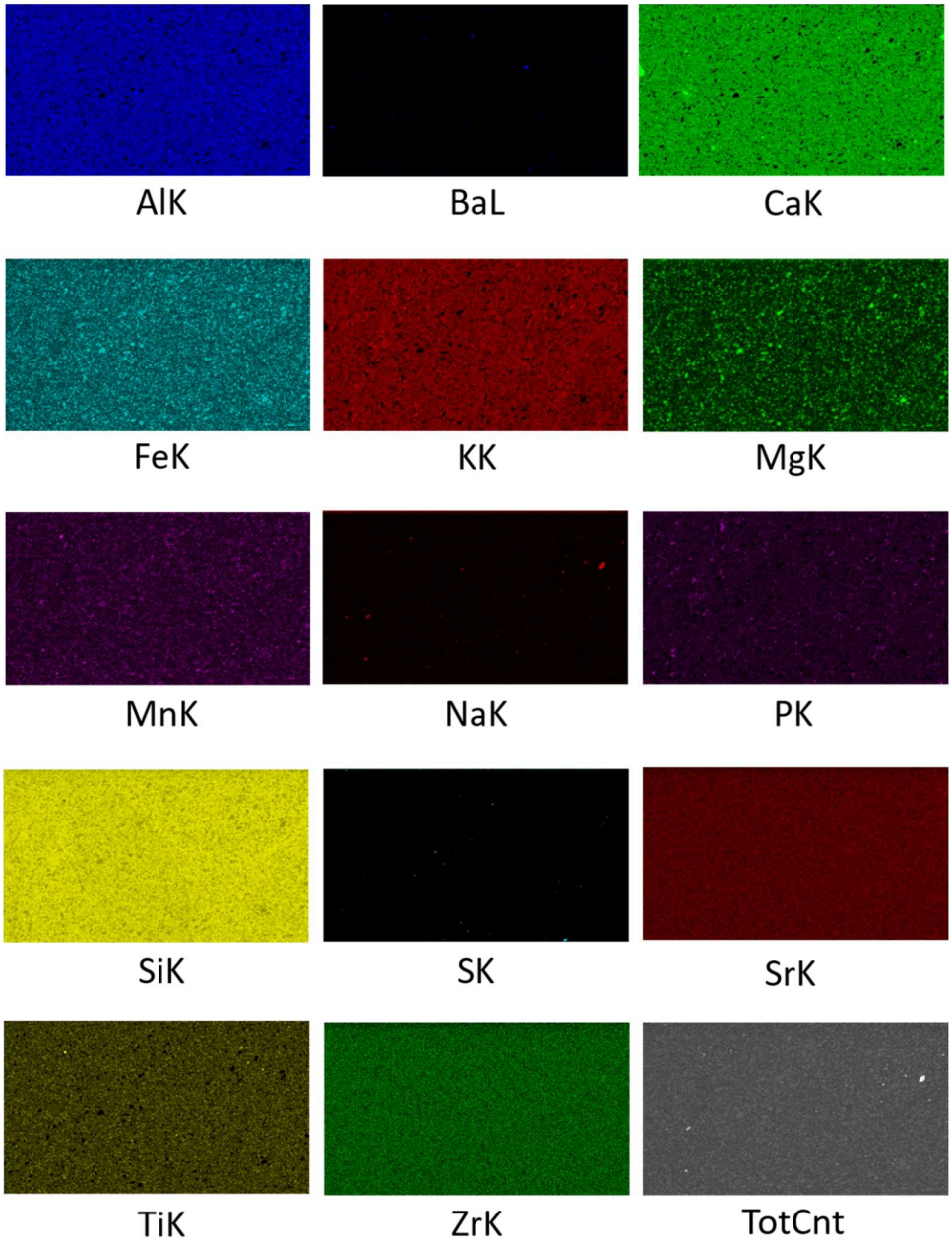

Micro-XRF elemental maps of sample J-83 (basalt).

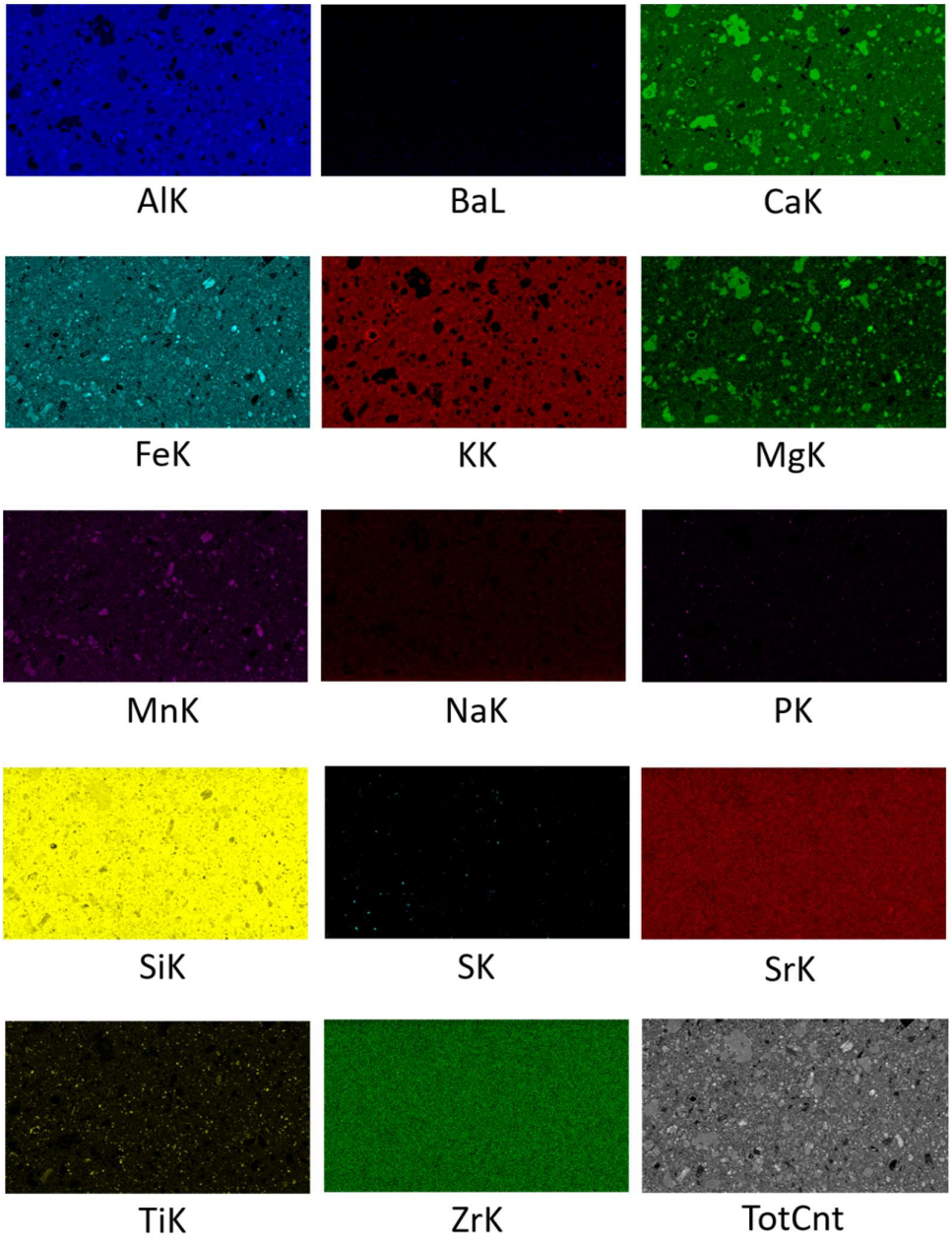

Micro-XRF elemental maps of sample TBD (olivinic basalt).

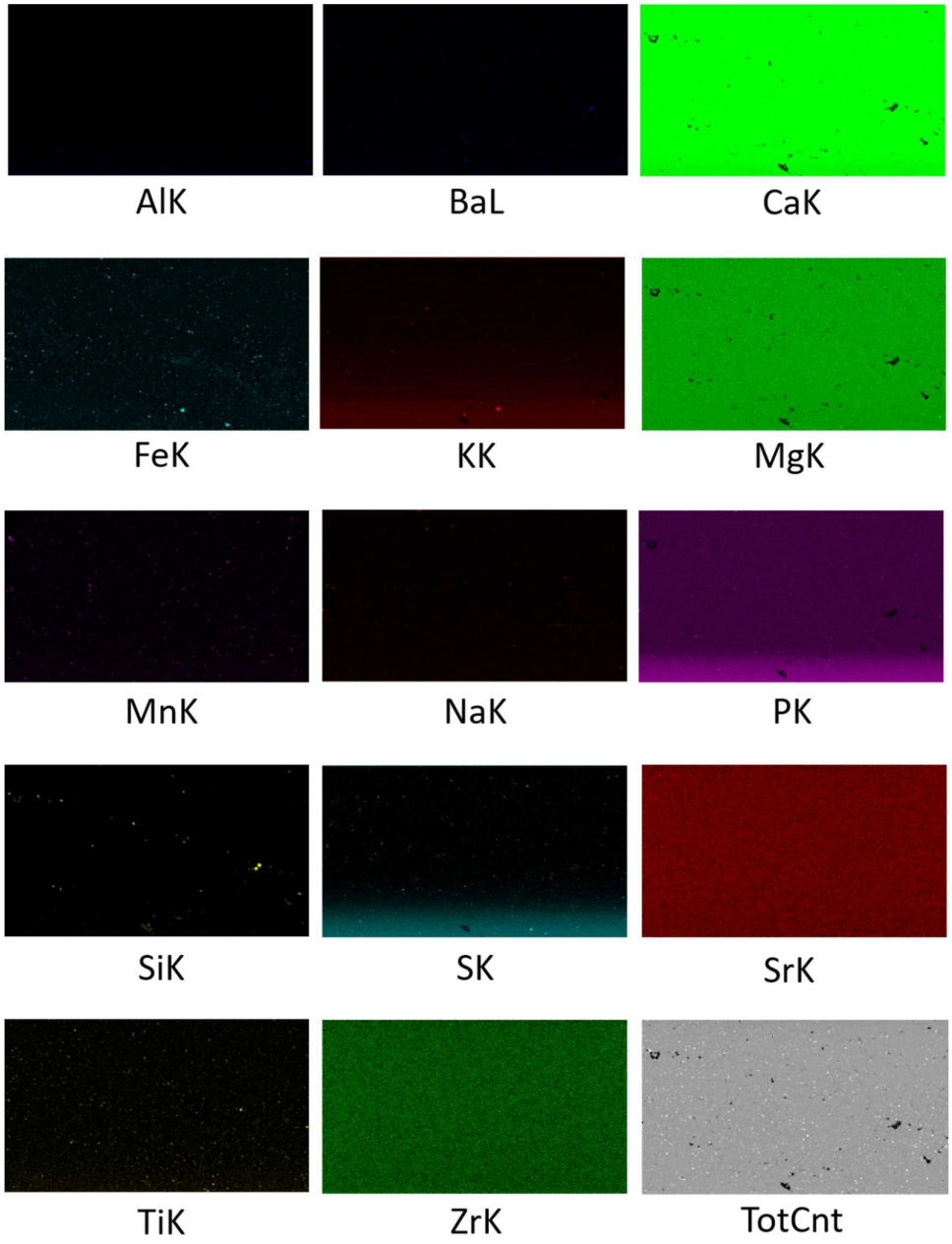

Micro-XRF elemental maps of sample C-B-Dol_002 (dolomite).

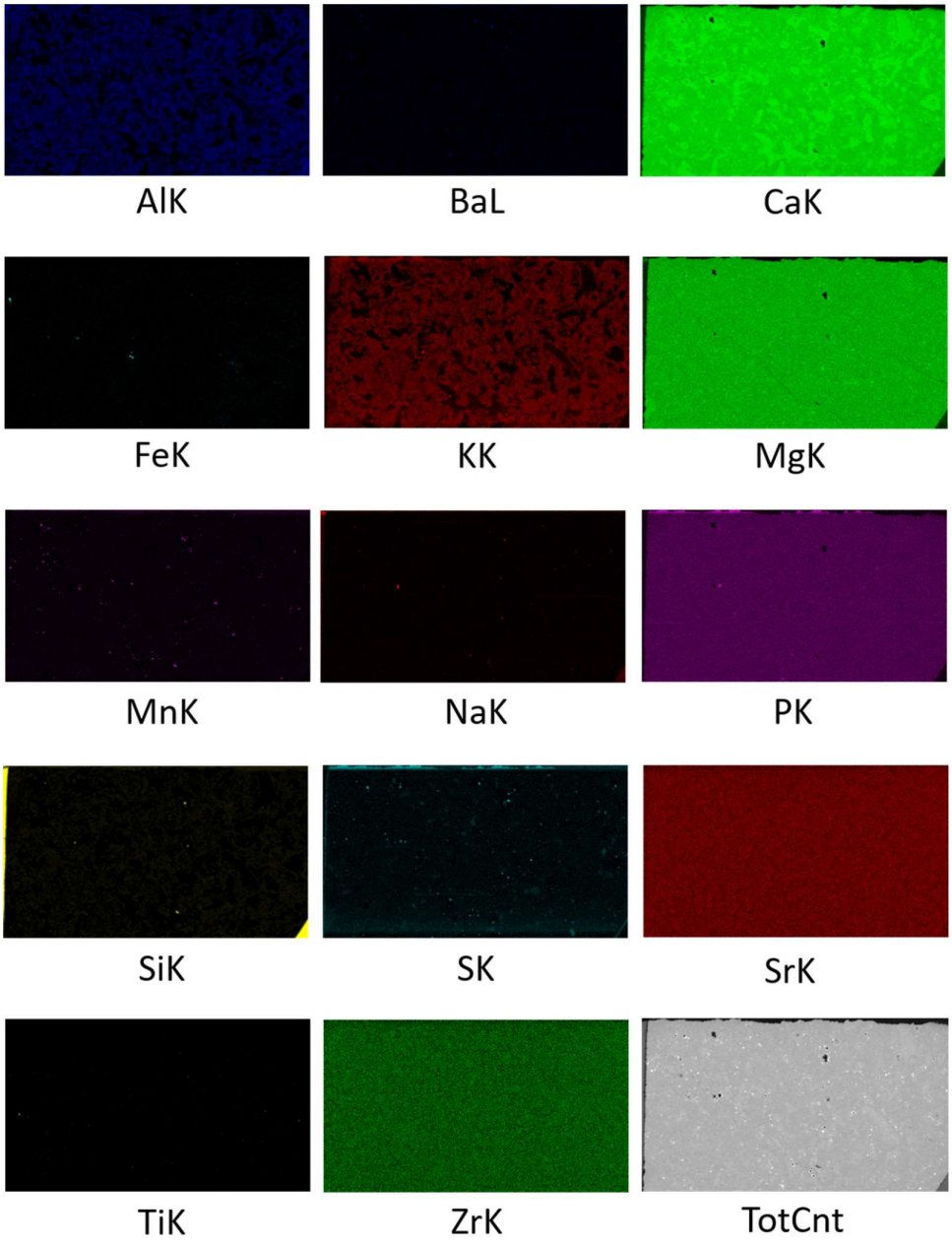

Micro-XRF elemental maps of sample C-B-Dol_004 (dolomite).

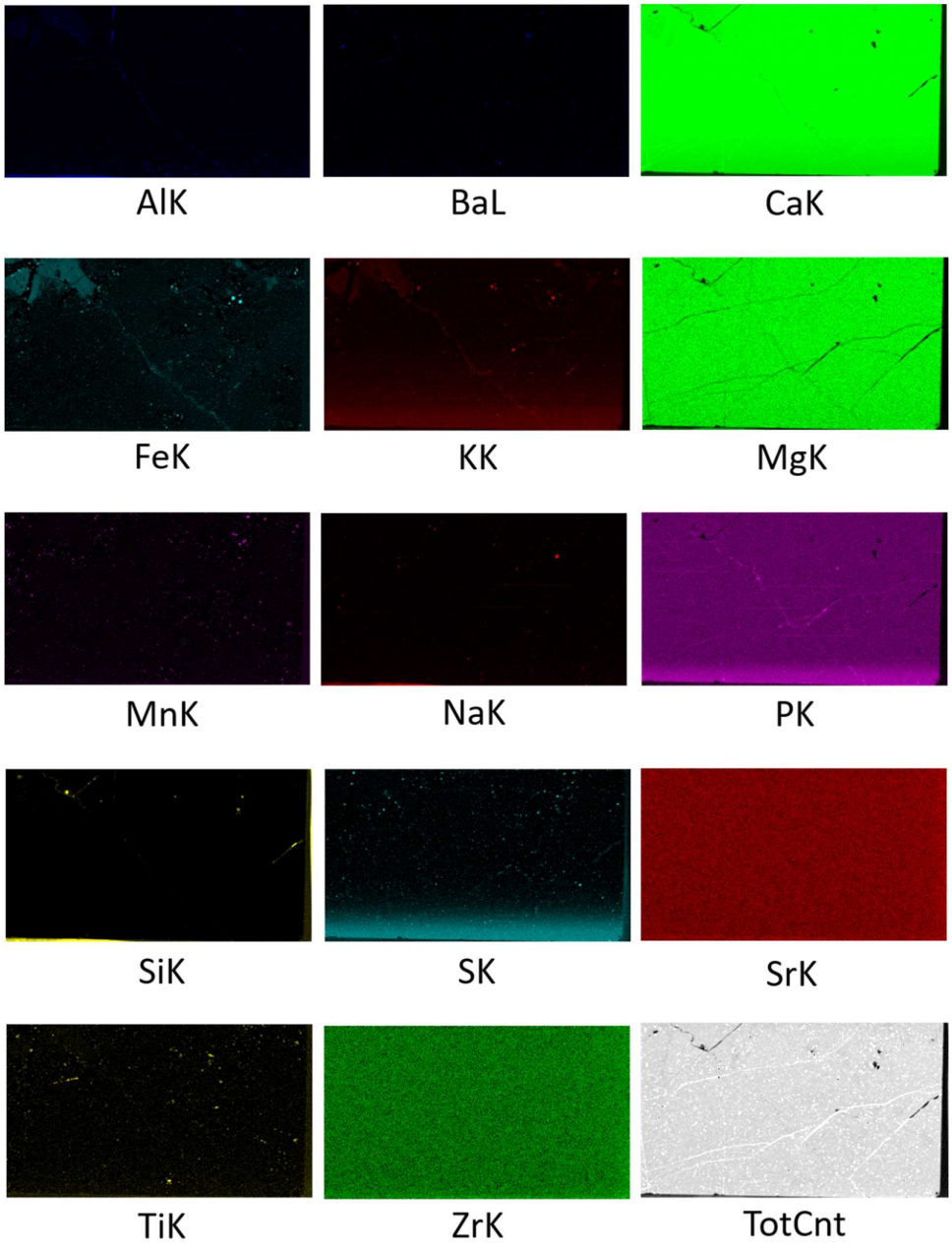

Micro-XRF elemental maps of sample C-B-Dol_007 (dolomite).

Appendix B

Helium pycnometer results for two trachyte samples.

Trachyte_1

Sample preparation	Specimen	Sample Weight (g)	Temperature (°C)	Run #	Volume (cm^3)	Density (g/cm^3)	Average Volume (cm^3)	Standard Deviation (cm^3)	Average Density (g/cm^3)	Standard Deviation (g/cm^3)
powder	1	0.4472	26.0	1	0.1624	2.7538	0.1621	0.0003	2.7589	0.0045
				2	0.1619	2.7624				
				3	0.1620	2.7605				
	2	0.5349	26.0	1	0.1884	2.8397	0.1884	0.0001	2.8397	0.0011
				2	0.1883	2.8407				
				3	0.1884	2.8386				
	3	0.5401	26.0	1	0.1904	2.8365	0.1903	0.0003	2.8374	0.0040
				2	0.1906	2.8340				
				3	0.1901	2.8418				
granulate	4	3.5753	26.2	1	1.3653	2.6187	1.3645	0.0006	2.6201	0.0011
				2	1.3651	2.6192				
				3	1.3642	2.6208				
				4	1.3641	2.6210				
				5	1.3641	2.6210				
	5	3.3854	26.2	1	1.2889	2.6265	1.2879	0.0008	2.6286	0.0016
				2	1.2884	2.6275				
				3	1.2878	2.6289				
				4	1.2875	2.6294				
				5	1.2869	2.6308				

Trachyte_22B

Sample preparation	Specimen	Sample Weight (g)	Temperature (°C)	Run #	Volume (cm^3)	Density (g/cm^3)	Average Volume (cm^3)	Standard Deviation (cm^3)	Average Density (g/cm^3)	Standard Deviation (g/cm^3)
powder	1	0.6293	26.0	1	0.2188	2.8756	0.2189	0.0001	2.8746	0.0016
				2	0.2188	2.8755				
				3	0.2191	2.8728				
	2	0.5992	26.0	1	0.2110	2.8396	0.2114	0.0005	2.8348	0.0068
				2	0.2112	2.8377				
				3	0.2120	2.8270				
	3	0.6340	26.0	1	0.2197	2.8863	0.2196	0.0001	2.8875	0.0019
				2	0.2194	2.8897				
				3	0.2197	2.8864				
granulate	4	3.8827	26.2	1	1.4844	2.6156	1.4842	0.0002	2.6160	0.0003
				2	1.4841	2.6162				
				3	1.4841	2.6162				
				4	1.4841	2.6162				
				5	1.4845	2.6156				
	5	3.1812	26.3	1	1.2058	2.6383	1.2055	0.0003	2.6389	0.0006
				2	1.2055	2.6390				
				3	1.2050	2.6399				
				4	1.2056	2.6386				
				5	1.2056	2.6387				

Percentage and matrix density of the mineral phases constituting dolomite samples.

	C-B-Dol_002 E		C-B-Dol_002 F		C-B-Dol_004 E		C-B-Dol_004 F		C-B-Dol_007 E		C-B-Dol_007 E	
Mineral	%	$\rho_{mineral}$	%	ρ_{matrix}	%	ρ_{matrix}	%	ρ_{matrix}	%	ρ_{matrix}	%	ρ_{matrix}
Calcite	0.49	2.72	0.2	2.71	1.1	2.73	0.92	2.73	1.11	2.72	0.47	2.72
Quartz	0.28	2.65	0.25	2.65	x		x		0.25	2.65	0.17	2.65
Dolomite	99.23	2.86	99.55	2.86	43.24	2.86	44.48	2.86	98.63	2.86	99.36	2.86
Dolomite (Ca excess)	x		x		53.2	2.86	52.3	2.86	x		x	
Illite	x		x		2.46	2.83	2.31	2.81	x		x	
ρ_{matrix}	2.858726		2.859175		285.7832		285.7935		2.857635		2.858985	

Helium Pycnometer results for three samples of dolomite.

C-B-Dol_002

Sample preparation	Specimen	Sample Weight (g)	Temperature (°C)	Run #	Volume (cm^3)	Density (g/cm^3)	Average Volume (cm^3)	Standard Deviation (cm^3)	Average Density (g/cm^3)	Standard Deviation (g/cm^3)
powder	1	0.8927	26.1	1	0.2924	3.0530	0.2927	0.0002	3.0504	0.0023
				2	0.2928	3.0491				
				3	0.2928	3.0490				
	2	0.7716	26.1	1	0.2490	3.0982	0.2486	0.0004	3.1040	0.0050
				2	0.2484	3.1064				
				3	0.2483	3.1074				
	3	0.7645	26.1	1	0.2474	3.0898	0.2472	0.0004	3.0921	0.0048
				2	0.2475	3.0890				
				3	0.2468	3.0976				
granulate	4	4.2670	28.6	1	1.5028	2.8394	1.5028	0.0002	2.8394	0.0003
				2	1.5026	2.8397				
				3	1.5029	2.8391				
	5	4.5740	28.6	1	1.6092	2.8423	1.6098	0.0006	2.8414	0.0010
				2	1.6097	2.8416				
				3	1.6104	2.8403				
	6	4.3229	28.6	1	1.5224	2.8396	1.5223	0.0001	2.8398	0.0002
				2	1.5223	2.8397				
				3	1.5221	2.8401				
	7	4.5902	28.6	1	1.6167	2.8393	1.6162	0.0006	2.8401	0.0011
				2	1.6164	2.8397				
				3	1.6155	2.8413				

C-B-Dol_004

Sample preparation	Specimen	Sample Weight (g)	Temperature (°C)	Run #	Volume (cm^3)	Density (g/cm^3)	Average Volume (cm^3)	Standard Deviation (cm^3)	Average Density (g/cm^3)	Standard Deviation (g/cm^3)
powder	1	0.7503	26.0	1	0.2419	3.1012	0.2418	0.0002	3.1029	0.0020
				2	0.2416	3.1051				
				3	0.2419	3.1023				
	2	0.6887	26.1	1	0.2221	3.1009	0.2225	0.0003	3.0957	0.0046
				2	0.2226	3.0943				
				3	0.2227	3.0920				
	3	0.8087	26.1	1	0.2648	3.0536	0.2643	0.0005	3.0600	0.0057
				2	0.2641	3.0619				
				3	0.2639	3.0644				
granulate	4	4.5169	28.6	1	1.6071	2.8106	1.6072	0.0001	2.8104	0.0002
				2	1.6072	2.8104				
				3	1.6073	2.8102				
	5	4.5684	28.6	1	1.6234	2.8142	1.6231	0.0002	2.8146	0.0004
				2	1.6229	2.8150				
				3	1.6231	2.8147				
	6	4.6306	28.6	1	1.6447	2.8155	1.6444	0.0014	2.8161	0.0025
				2	1.6428	2.8188				
				3	1.6456	2.8139				
	7	4.2046	28.6	1	1.4942	2.8140	1.4942	0.0001	2.8140	0.0001
				2	1.4942	2.8139				
				3	1.4941	2.8142				

C-B-Dol_007

Sample preparation	Specimen	Sample Weight (g)	Temperature (°C)	Run #	Volume (cm^3)	Density (g/cm^3)	Average Volume (cm^3)	Standard Deviation (cm^3)	Average Density (g/cm^3)	Standard Deviation (g/cm^3)
powder	1	0.5708	26.1	1	0.1823	3.1318	0.1821	0.0001	3.1343	0.0023
				2	0.1820	3.1361				
				3	0.1821	3.1351				
	2	0.8429	26.1	1	0.2761	3.0533	0.2759	0.0003	3.0554	0.0035
				2	0.2755	3.0594				
				3	0.2761	3.0534				
	3	0.8378	26.2	1	0.2688	3.1163	0.2692	0.0003	3.1127	0.0035
				2	0.2692	3.1124				
				3	0.2694	3.1094				
granulate	4	4.4434	28.6	1	1.5696	2.8310	1.5696	0.0009	2.8309	0.0017
				2	1.5706	2.8292				
				3	1.5687	2.8325				
	5	4.5932	28.6	1	1.6219	2.8319	1.6220	0.0002	2.8318	0.0004
				2	1.6219	2.8321				
				3	1.6223	2.8313				
	6	4.6062	28.6	1	1.6288	2.8280	1.6286	0.0002	2.8284	0.0004
				2	1.6285	2.8284				
				3	1.6284	2.8287				
	7	4.4420	28.6	1	1.5686	2.8318	1.5682	0.0005	2.8326	0.0008
				2	1.5677	2.8334				
				3	1.5682	2.8325				

Ringraziamenti

Voglio ringraziare innanzitutto il professor Antonio Galgaro che ha riposto in me grande fiducia fin dal primo istante. Lo ringrazio per le opportunità che ho potuto sfruttare, l'esperienza di Torino e il cantiere dell'ex geriatrico, e anche per quelle che purtroppo non sono andate in porto, come l'EGC. Un grazie va al Dott. Matteo Cultrera che mi ha supportato in questi mesi. I suoi consigli mi sono stati di grandissimo aiuto.

Un grazie particolare va al Dott. Michele Secco per la sua infinita disponibilità, per la sua positività e per avermi sempre fatto credere che ce la potevo fare. Nei miei momenti di sconforto ha sempre saputo risollevarmi il morale.

Ringrazio infinitamente anche il Dott. Luigi Germinario che ha accettato di aiutarmi e che mi ha dedicato parte del suo tempo.

Ringrazio il Prof. Alessandro Borghi e il Dott. Roberto Cossio del dipartimento di Scienze della Terra di Torino che si sono resi disponibili per l'acquisizione delle mappe tramite micro-XRF.

Molte altre persone mi sono state di grande aiuto per i consigli e i suggerimenti dati. Ringrazio quindi la Prof.ssa Maria Chiara Dalconi, Leonardo Tauro, il Dott. Federico Zorzi, il Dott. Lorenzo Raccagni, il Dott. Hamada del dipartimento di ingegneria industriale, il Dott. Fabio Tateo, il Prof. Nereo Preto, il Prof. Raffaele Sassi, la Dott.ssa Eloisa Di Sipio, la Dott.ssa Daria Pasqual, il Dott. Pietro De Mori.

L'Università ha occupato una parte importante della mia vita. Mi ha regalato tante soddisfazioni, mi ha fatto maturare e mi ha dato la possibilità di incontrare molte persone. Questo lungo percorso non sarebbe stato lo stesso senza i miei compagni di viaggio. Ciascuno di loro mi ha lasciato qualcosa. Alcuni di loro meritano però un ringraziamento particolare. Giorgia, sei stata e sarai la migliore compagna e amica. Ti voglio un mondo di bene. Tommy, la nostra è stata la storia più travagliata di sempre. I ricordi migliori che ho e che mi porterò per sempre sono sicuramente legati a te. Ci siamo tanto divertiti e abbiamo tanto sofferto. Per questo motivo credo si sia creato un legame speciale. Carry, il mio più grande rimpianto è non aver saputo capirti da subito ed essermi avvicinata a te quando ormai era troppo tardi. Pippo, abbiamo sprecato molto tempo per delle stupide gelosie. Mi dispiace se a volte non ho saputo gestire la situazione. Un Grazie anche a tutti gli altri. Vi voglio bene.

Non è stato solo puro divertimento. L'università per me è stata anche l'ansia prima degli esami, la preoccupazione di non essere all'altezza, i sacrifici per poter dare sempre il massimo. Ed ecco che il famigerato "stress" è entrato nella mia vita per non lasciarmi più. Il mio intestino è il suo migliore amico ed ormai ho imparato a gestirlo quando fa i capricci. Quando ho conosciuto Diego la situazione era però ben diversa. Non mangiavo praticamente più nulla, avevo perso chili e stavo sempre male. Coincidenza o no, con Diego è arrivata anche la cura che ha risolto molti dei miei problemi. Per questo, ma non solo, non finirò mai di ringraziarti. Mi hai accompagnato in questi ultimi due anni dandomi spesso la forza di continuare nei momenti di sconforto. Sei rimasto al mio fianco anche quando ero insopportabile e ingestibile. Grazie di cuore.

Ringrazio poi la parte più importante: la mia famiglia. Ringrazio mamma e papà che non mi hanno fatto mai mancare niente. Li ringrazio per aver sostenuto le spese per i miei studi, per esserci stati quando avevo bisogno, e per aver sempre assecondato le mie scelte perché dagli errori che ho fatto ho imparato moltissimo.

Grazie a Maurizio che per cinque anni ha esclamato "Solo?" di fronte agli esiti degli esami, anche e soprattutto con i 30 e lode. Grazie papà perché, con i tuoi mille difetti, sei il papà perfetto.

Grazie a Matteo senza del quale non avrei un computer, e se anche ce l'avessi non lo saprei usare (non che adesso sia la mia più grande abilità ma almeno questa tesi l'ho scritta da sola). Sono una sorella rompiscatole quindi grazie per aver imparato a sopportarmi.

E poi c'è Lorella. La mamma migliore del mondo e anche la mia migliore amica. I motivi per cui ringraziarti sono infiniti quindi farò una selezione. Grazie mamma per esserti presa cura di me, sempre. Grazie per essere stata il mio punto di riferimento, il mio sostegno e la mia forza. Siamo sempre state una cosa sola io e te. Insieme abbiamo gioito per i miei traguardi e insieme abbiamo sofferto quando stavo male e mi allontanavo. Ti chiedo scusa per i momenti difficili che ti ho fatto passare.

Ringrazio infine il mio angelo custode Clemente che è sempre vicino a me e mi protegge. Tutte le cose belle che mi sono successe e che mi succederanno sono sicuramente merito suo. Sempre nei miei pensieri.